Measurement of the Energy Spectrum of Ultra-High Energy Cosmic Rays using Hybrid Data of the Pierre Auger Observatory

Zur Erlangung des akademischen Grades eines
DOKTORS DER NATURWISSENSCHAFTEN
von der Fakultät für Physik der Universität (TH)
Karlsruhe

genehmigte
DISSERTATION

von Dipl.-Phys. Frank Fabian Schüssler
aus Karl-Marx-Stadt/Chemnitz

Bestimmung des Energiespektrum ultra-hoch energetischer kosmischer Strahlung mit Hybridmessungen des Pierre Auger Observatoriums

Das Thema dieser Arbeit ist die Bestimmung des Energiespektrums kosmischer Strahlung bei höchsten Energien. Die dazu verwendeten Hybriddaten des Pierre Auger Observatoriums zeichnen sich durch eine hohe Rekonstruktionsgenauigkeit und die Abdeckung eines grossen Energiebereichs aus. Dieser schließt den erwarteten Übergang von galaktischen zu extragalaktischen Quellen der kosmischen Strahlung ein. Eine sehr gute Energieauflösung von besser als 10 %, die durch eine geeignete Selektion der Daten erzielt wurde, ermöglicht die Untersuchung der spektralen Eigenschaften in diesem für das Verständnis der ultra-hoch energetischen kosmischen Strahlung extrem wichtigen Bereich mit hoher Präzision. Zur Bestimmung der zeitintegrierten Detektorakzeptanz wurde ein neues Verfahren eingeführt. Basierend auf einer Vielzahl von Datenquellen konnte der Zustand aller Detektorkomponenten des Pierre Auger Observatoriums einschließlich aller zeitlichen Veränderungen abgeleitet werden. Diese Information bildet die Grundlagen einer neuartigen Monte Carlo Detektorsimulation, die die realen Bedingungen der Datennahmen reproduziert. Die Übereinstimmung zwischen Simulation und Daten wurde ausführlich überprüft. Spezielle Selektionskriterien ermöglichten die Beseitigung von systematischen Abhängigkeiten des bestimmten Energiespektrums von der Masse der kosmischen Primärteilchen, Details der hadronischen Wechselwirkungen bei ultra-hohen Energien und der systematischen Unsicherheit der Energieskala des Experiments. Der Einfluss von Wolken auf Luftschauerbeobachtungen konnte bestimmt und beseitigt werden. Das Energiespektrum wurde mit einer systematischen Unsicherheit von 6 % bestimmt. Eine signifikante Änderung des spektralen Verlauf bei $10^{18.7}$ eV konnte nachgewiesen und, zusammen mit Messungen der Massenzusammensetzung der kosmischen Strahlung, mit verschiedenen phenomenologischen Modellen verglichen werden.

Abstract

The subject of this thesis is the measurement of the energy spectrum of ultra-high energy cosmic rays from simultaneous observation of fluorescence and surface detectors of the Pierre Auger Observatory. These hybrid data allow us to study a wide energy range, which includes the region were the transition between galactic and extragalactic cosmic rays is expected. Dedicated event selection criteria result in an unprecedented energy resolution of less then 10 %, which makes a precise determination of spectral features possible. To determine the exposure accumulated during the first years of operation of the observatory, a novel technique has been developed. Based on a very detailed description of the data taking conditions and the status of all parts of the Pierre Auger Observatory, a time dependent Monte Carlo simulation has been introduced. Extensive comparisons ensure the exact reproduction of actual data at all levels and time scales. The definition of an energy dependent fiducial volume led to the removal of systematic dependencies from assumptions on the mass of the primary particles, the details of hadronic interactions at ultra-high energies and the systematic uncertainty of the energy scale of the observatory. A total systematic uncertainty of

6 % has been derived from independent air shower measurements of the surface array and cross-checked with different methods. Extending the nominal energy range of the Pierre Auger Observatory to lower energy, the hybrid energy spectrum above 10^{18} eV is measured. It shows a significant break of the power-law behavior at $10^{18.7}$ eV. The details of this spectral feature known as the 'ankle', are interpreted in conjunction with mass composition data within different phenomenological models of ultra-high energy cosmic rays.

Résumé

Le sujet de cette thèse est la mesure du spectre énergétique des rayons cosmiques de ultra hautes énergies. Cette mesure est basée sur les données hybrides de l'observatoire Pierre Auger qui se caractérisent par une haute précision de reconstruction et permettent d'étudier une large domaine en énergie, ce qui inclut la transition attendue entre les rayons cosmiques de sources galactiques et extragalactiques. La très bonne résolution de l'énergie (< 10 %) permet l'étude précise des propriétés spectrales.

Afin de déterminer l'exposition cumulée pendant les premières années de fonctionnement de l'observatoire, une nouvelle technique a été développée. L'état du détecteur et son évolution dans le temps ont pu être déterminés grâce à une multitude de données. Ces informations sont la base d'une nouvelle technique de simulation Monte Carlo, qui reproduit la situation exacte de la prise des données. L'accord entre la simulation et les données a été vérifié en détail. Des critères de sélection permettent l'élimination des dépendances du spectre à l'incertitude systématique de l'échelle d'énergie, aux détails des interactions hadroniques à ultra-hautes énergies et à l'hypothèse sur la masse des particules primaires. En outre, l'influence des nuages sur la détection des gerbes atmosphériques a pu être déterminée et éliminée.

L'incertitude systématique du spectre a pu être réduite à 6 %. Une modification significative de l'index spectral du flux du rayonnement cosmique a été mis en évidence à une énergie de $10^{18.7}$ eV. En associant les détails de cette caractéristique spectrale, connu sous le nom de «cheville», avec des données sur la composition de la masse des particules primaires, différents modèles phénoménologiques de rayons cosmiques de ultra-haute énergie ont pu être testés.

Contents

Chapter 1

Introduction

Cosmic rays are both a great tool and a great mystery to physicists. Shortly after the discovery of this high energy radiation from the universe at the beginning of the last century, it could be used very successfully to study phenomena at energies not reachable with man-made devices at that time. Many important advances in elementary particle physics like the discovery of the positron [1], muon [2] and pions [3–5] were only possible by studying cosmic rays.

Since then, the studied energy range has been constantly enlarged. The extremely low flux of very high energy cosmic rays, which decreases steeply with increasing energy, required the development of new detection methods like the fluorescence, Cherenkov or radio technique and the deployment of huge arrays of surface detectors.

Surprisingly, particles with energies even exceeding 10^{20} eV have been detected. The processes that could accelerate particles to such high energies are one of the greatest mysteries of modern physics and their understanding would provide insight into physics under extreme conditions.

Almost a century after the discovery of cosmic rays, astroparticle physics is currently entering a new era. The completion of the southern part of the Pierre Auger Observatory [6] provides high precision and high statistics data of cosmic rays at ultra-high energies. Detailed measurements like the determination of the mass of the primary cosmic rays, their energy spectrum and arrival direction distribution are now in reach.

One of the most fundamental measurements is the determination of the cosmic ray energy spectrum, which reflects the injection spectrum of the unknown sources and the physics of ultra-high energy particle propagation through the universe. Many studies focus on the upper end of the spectrum. During the last years, however, it has been realized that one of the most efficient and complementary ways to obtain information about the origin of cosmic rays at ultra-high energies is the study of the energy range between $10^{18} - 10^{19}$ eV, where the transition between galactic and extragalactic cosmic rays is expected. This energy range is accessible with high precision "hybrid" measurements of the Pierre Auger Observatory, i.e. simultaneous observations with two complementary detectors, a surface array and a fluorescence detector.

The aim of this work is a measurement of the ultra-high energy cosmic ray spectrum

in the transition range from galactic to extragalactic cosmic rays. The flux of cosmic rays is derived by counting the number of events in a given energy interval and comparing it with the integrated aperture of the instrument. In a first step, observed air showers were reconstructed and their characteristic parameters were determined. This has been done by developing an automated event reconstruction scheme and storing the reconstructed events in a dedicated data summary format. In a second step, the time dependent aperture of the detector system, the other key element for the flux measurement, was determined. Whereas the aperture for surface detector arrays can be derived purely from geometrical considerations, its determination is one of the main challenges for optical detectors like the fluorescence telescopes of the Pierre Auger Observatory. The aperture of a fluorescence detector is depending on a large number of highly correlated parameters like the energy, mass and direction of the primary particle and atmospheric conditions. For the work presented here, additional difficulties arise from the fact that the detector itself was in its construction phase. Not only the changes of the detector configuration, but also the initial failures of detector components during the startup phase have to be accounted for.

In addition to these large scale changes, smaller but nevertheless important changes occur on much shorter timescales. The most important effects analyzed in this work include the fact that the fluorescence detector is taking data only during moonless nights, which introduces a seasonal dependence of the aperture as nights are longer during the winter season. Other weather effects like storm or rainfall are affecting the available detector configuration as some parts might be shut down for safety reasons. In addition, changing background light is affecting the trigger threshold of the fluorescence telescopes. Also the status of the surface detector is constantly changing, for example, by the temporary loss of the wireless communication between the stations and the central data acquisition system. These and other changes in the detector configuration have to be taken into account during the determination of the aperture.

A novel approach for the exposure determination, called REALMC , has been developed. In a first step a complete time dependent detector status description, which takes into account all known effects that might influence the data taking of the observatory, was derived (cf. Sec. 4). This information is used as basis for extensive Monte Carlo simulations reproducing the actual data conditions (cf. Sec. 5). After validating the REALMC simulations with data at various reconstruction levels, they were used to determine the time integrated aperture of the Pierre Auger Observatory in hybrid mode (cf. Sec. 6).

The quality of the selected events and an unprecedented energy resolution is assured by dedicated selection criteria, which were verified with Monte Carlo simulations. Additional selection criteria have been developed to minimize systematic dependencies of the energy spectrum on the primary mass composition, hadronic interaction models and the absolute energy scale of the observatory.

Extending the nominal energy range of the Pierre Auger Observatory to lower energy, the hybrid energy spectrum above 10^{18} eV has been derived and compared with existing data. Finally different physics interpretations are discussed.

Chapter 2

Ultra-high energy cosmic rays

Since the first indirect detection of radiation from outside the Earth by Victor Hess almost 100 years ago [7], cosmic rays have puzzled physicists and astronomers alike. Although enormous progress has been made with respect to both theoretical understanding and experimental observations, fundamental questions remain unanswered: "What are the astrophysical sources of ultra-high energy cosmic rays?", "What is the mass composition of the highest energetic particles?", "Is there a transition between galactic and extragalactic cosmic rays?", . . .

The current level of understanding of these problems will be discussed briefly in Sec. 2.2. The experimental difficulties of cosmic ray experiments, in general, are related to the extremely low flux of particles. Fortunately the detection of the very rare ultra-high energy cosmic rays (UHECRs) is facilitated by the creation of huge particle cascades in the Earths atmosphere. Phenomenological approaches and experimental techniques to detect these *extensive air showers* (EAS) are reviewed in Sec. 2.1.1. Many aspects of the understanding of UHECRs are linked together in the interpretation of the energy spectrum, which follows a power-law over many decades in energy. Only a very limited number of features, i.e. slight changes of the slope have been observed. Details of these features and their possible interpretations are discussed in Sec. 2.2.3.

2.1 Extensive air showers

2.1.1 Phenomenology of extensive air showers

Shortly after Rossi reported on 'very extensive groups of particles which produce coincidences between counters even rather distant from each other' [8], Pierre Auger introduced the notion of *extensive cosmic-ray showers* in 1938/1939. Auger had performed measurements of coincidence rates of detectors placed both at sea level and at high altitude (Jungfraujoch, 3500 m and Pic du Midi, 2900 m) with as separation of up to several hundreds of meters [9]. He concluded the existence of primary particles with an energy around 10^{15} eV creating a multitude of secondary particles when interacting with the molecules of the Earth's atmosphere.
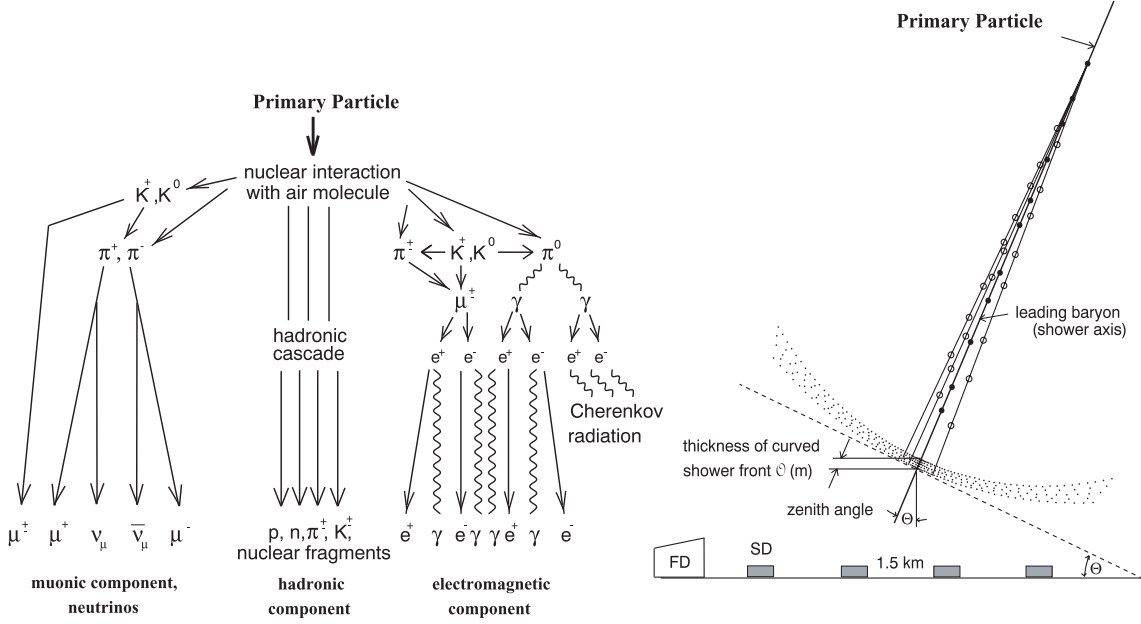
Figure 2.1.1: Left panel: Particle content of extensive air showers. Right panel: Air shower detection techniques and important parameters.

This first interaction usually takes place in the upper atmosphere and, due to the low density of the air and the stochastic nature of particle interactions, results in large fluctuations of the height of this interaction. Assuming a primary cosmic ray nucleon, mostly pions and kaons together with a leading baryon are produced in the interaction. The primary energy is shared between these secondaries and, due to the enormous amount of energy available, they have a large probability to interact with other nuclei in the atmosphere and produce new particles before decaying into (mainly) photons, muons, electron and neutrinos.

As sketched in Fig. 2.1.1, the resulting extensive air shower consists of three main components: a hadronic, a muonic and an electromagnetic component. Due to the high boost factors and the comparably low transverse momentum of the secondary particles produced in the hadronic interactions, the hadronic component is forming along the incoming direction of the primary cosmic ray. Production of π^0 instantly decaying into two photons is the main mechanism to transfer energy to the electromagnetic part of the air shower, which very quickly becomes the dominant component. Charged pions and kaons decay into muons and neutrinos. The latter can not be detected and need to be corrected for during the reconstruction of air shower measurements (cf. Sec. 3.2.4). A sketch of the interplay between the different air shower components is given in Fig. 2.1.2.

As the dominant part of air showers in terms of number of particles is the electromagnetic component, the main features of the shower development can be described in a comprehensive way [11, 12]. $e^\pm$ and γ undergo bremsstrahlung and pair production, respectively, if their energy is higher than the critical energy E_{crit} at which energy losses dE/dX due to ionization become important, i.e.

$$\left.\frac{dE}{dX}\right|_{E=E_{crit}}^{\text{ionization}} = \left.\frac{dE}{dX}\right|_{E=E_{crit}}^{\text{brems}}. \tag{2.1.1}$$
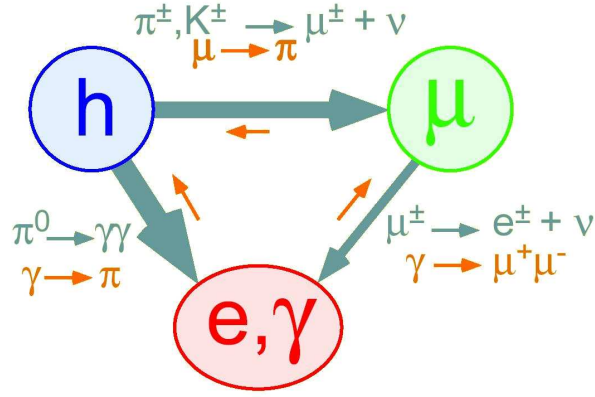
Figure 2.1.2: Energy flow between different air shower components. The thickness of the arrows illustrates the amount of energy transfered in the given direction by the stated processes (from [10]).

In air the critical energy is about 85 MeV. Furthermore a constant radiation length X_0 of about $37\,\mathrm{g/cm^2}$ can be assumed for both processes. This means that after each step of traversed matter, or 'grammage' X_0 ($[\mathrm{g/cm^2}]$) either a new $e^+ - e^-$ pair or a bremsstrahlung γ is created (cf. Fig. 2.1.3, left panel). The total number of particles after n steps is therefore $N = 2^n$. In each interaction the initial energy is assumed to be divided into equal parts among the two secondary particles. Starting the cascade with a primary energy E_0, the average energy of each shower particle after n steps is

$$E_n = E_0/N = E_0/2^n \,. \tag{2.1.2}$$

As soon as ionization losses are becoming important (i.e. $E_n \leq E_{\mathrm{crit}}$), absorption starts to dominate over particle creation and the total number of shower particles is decreasing. This point of maximal shower development is reached at a depth

$$X_{\mathrm{max}} = N_{\mathrm{max}} \cdot X_0 = \ln \frac{E_0}{E_{\mathrm{crit}}} \cdot \frac{X_0}{\ln 2} \,, \tag{2.1.3}$$

where N_{max} is the number of generations created until the shower maximum. Given Eq. (2.1.2), it can be written as

$$E_{N_{\mathrm{max}}} = E_0/2^{N_{\mathrm{max}}} \equiv E_{\mathrm{crit}} \quad \longrightarrow \quad N_{\mathrm{max}} = \ln \frac{E_0}{E_{\mathrm{crit}}} / \ln 2 \,. \tag{2.1.4}$$

The measurement of the total number of electromagnetic particles (e^+, e^- and γ) at the shower maximum ($2^{N_{\mathrm{max}}}$) can be used to infer the energy of the primary cosmic ray E_0. A more precise energy determination will be discussed in Sec. 3.2.1. It is relying on large parts of the shower development in the atmosphere which can be observed by fluorescence detectors.

An extension of this shower development scheme, as depicted in [14], is including hadronic interactions and the muonic component of air showers. In addition to a different interaction length X_1 of about $120\,\mathrm{g/cm^2}$ in air for inelastic hadronic processes, the main
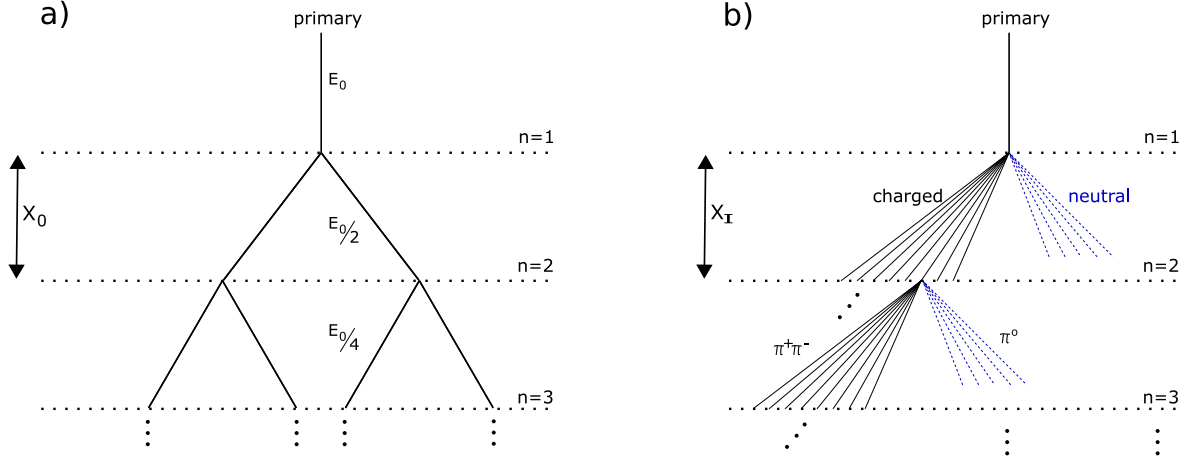
Figure 2.1.3: Heitler model of electromagnetic cascades (a) and extension to hadronic showers (b) (from [13]).

feature of these interactions is the higher number of secondary particles or 'multiplicity' N_{mult} (cf. Fig. 2.1.3, right panel). The fundamental relation (2.1.3) is slightly modified into

$$X_{\text{max}} \propto X_1 \ \ln \frac{E_0}{N_{\text{mult}} \cdot E_{\text{crit}}^{\text{had}}} \ , \tag{2.1.5}$$

where $E_{\text{crit}}^{\text{had}} \approx 20\,\text{GeV}$ denotes the energy threshold at which the pion decay length becomes comparable to the interaction length [14]. In this relatively simplistic model only pions are produced as secondary particles. The electromagnetic component is initiated by neutral pion decays whereas the charged pions either re-interact or decay and build up the muonic component.

Another very useful model for the description of air showers is the *superposition model*. In this scheme, an air shower initiated by a nucleus containing A nucleons and carrying an energy E_0 is treated as A independent air showers, each initiated by nuclei ($A = 1$) carrying an energy E_0/A. Together with (2.1.3) this simplification yields

$$X_{\text{max}} \propto \ln \left(\frac{E_0}{A} \right) \ . \tag{2.1.6}$$

The position of the shower maximum X_{max} is a parameter, which is rather easy to access in air shower observations with fluorescence detectors. Comparisons between measurements and detailed MC simulations allow one, within the limits of the correctness of the high energy interaction models, to derive the mass composition of cosmic rays. Results of this technique will be discussed in Sec. 2.2.2.

2.1.2   Detection of extensive air showers

Two main techniques have been developed to observe and study extensive air showers: optical telescopes and ground arrays of particle detectors. Both of them have their particular advantages and disadvantages, some of which will be stressed in this section. The combination of both techniques allows one to overcome most of the problems and gain a lot of

insight into the features of extensive air showers and primary cosmic rays. The currently largest hybrid cosmic ray experiment, the Pierre Auger Observatory, will be introduced in Sec. 3.

Another detection technique employed successfully for example by the Tunka experiment [15], uses arrays of optical detectors on the ground to record cherenkov light emitted by the air shower in the atmosphere. The revival and extensive R&D work related to radio measurements of air showers is aiming at establishing a third technique. With relatively small test arrays of radio detectors first observations [16] in the radio domain could be achieved. Extensive accompanying simulation studies [17] helped to increase the understanding of the underlying processes and the full scale use for air shower observations seems possible in the future [18].

Ground arrays

Starting with Pierre Auger's first experiments, ground based EAS detectors have a long and very successful history. As high energy EAS cover large areas on the ground, even a sparsely instrumented detection area is sufficient to detect and reconstruct important parameters of the primary particle. If, for example, more than two independent stations recorded the signal and arrival time of the shower, the reconstruction of the impact point and its direction becomes possible. With the help of Monte Carlo (MC) simulations, the recorded signal can be related to the total number of particles in the air shower and the energy of the primary cosmic ray. This latter step introduces uncertainties as the details of the hadronic interactions at energies well above those reachable with man-made accelerators are subject to rather large theoretical uncertainties [19] and shower to shower fluctuations. On the other hand, data can be taken with an almost 100 % duty-cycle. If an energy threshold above which all air showers falling onto a ground array will trigger the detectors can be determined, the acceptance of such a detector is determined solely by the geometric aperture and is readily calculable.

Various types of particle detectors have been used in UHECR experiments. Concentrating on the electromagnetic EAS component scintillators have been employed by the pioneering experiment at Volcano Ranch [20] and the Akeno [21]/AGASA [22] experiments. A new scintillator array, the Telescope Array [23], is currently being commissioned. In Fig. 2.1.4a the first event with an energy above 10^{20} eV, detected with the Volcano Ranch ground array is shown.

The Haverah Park experiment [24] used water Cherenkov detectors observing the flashes of Cherenkov light when the shower particles traverse the water in the detector. This technique is now used on a much larger scale in the Pierre Auger Observatory [6] and will be discussed in Sec. 3.

Several techniques like electron and muon counters together with a hadron calorimeter are used in the KASCADE [25] and KASCADE-Grande [26] experiments. The measurement of all main EAS components facilitates very detailed studies for example of the changing mass composition in the energy range around $10^{16.5}$ eV [27]. Detailed studies in the knee region are also performed at high altitude by the Tibet array [28].

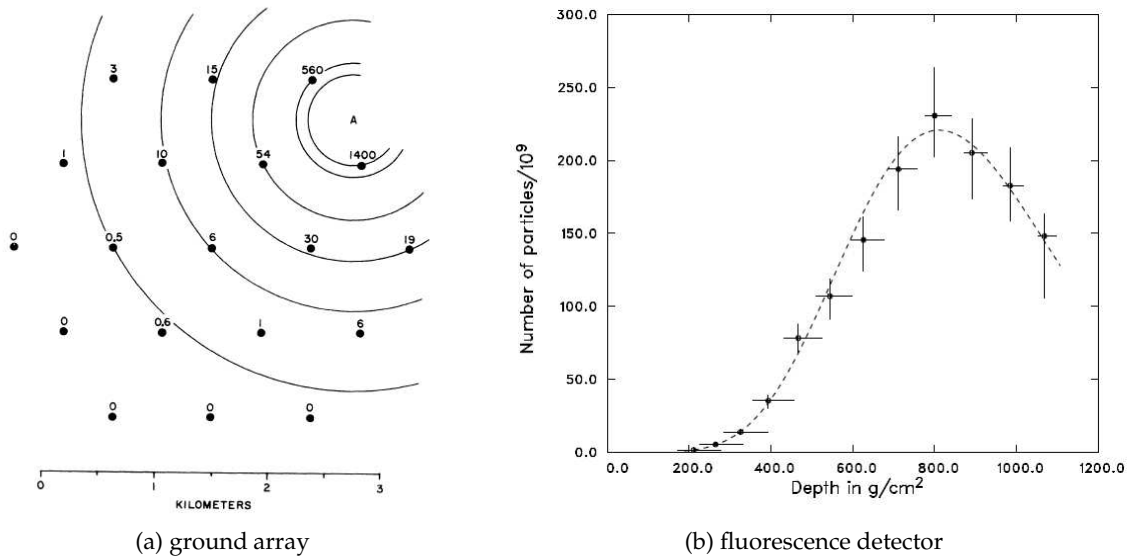(a) ground array   (b) fluorescence detector

Figure 2.1.4: Observations of EAS initiated by cosmic rays with energies above 10^{20} eV. The events have been detected by the scintillator array Volcano Ranch (left panel, [29]) and the Fly's Eye fluorescence detector (right panel, [30]).

Fluorescence detectors

The electromagnetic particles in air showers excite air molecules (mainly nitrogen). The prompt de-excitation of these molecules is associated with the emission of fluorescence light in the UV-band ($\lambda \approx 300 - 400$ nm). The ionization energy loss of the shower particles can be described by the Bethe-Bloch formula and the connection between energy deposit and amount of emitted light, the *fluorescence yield*, is measured in laboratory experiments [31–33]. Fluorescence light is emitted isotropically around the air shower axis, which is an advantage for air shower fluorescence measurements, as the recording telescopes do not have to be very close to the shower itself and (depending on atmospheric conditions) large volumes can be monitored. Using the atmosphere as calorimeter, a precise energy determination becomes possible and the dependence on air shower simulations is reduced significantly. The observation of the longitudinal shower development and especially the position of the shower maximum X_{max} is increasing the sensitivity to the mass composition of the primary cosmic rays (cf. Eq. (2.1.6) and Sec. 2.2.2). On the other hand, the atmospheric condition have to be monitored very precisely and data taking is limited to clear, moonless nights, which reduces the duty-cycle to $10 - 15$ % (cf. Sec. 4).

Most of the shower particles are highly relativistic leading to the additional emission of Cherenkov light on their way through the atmosphere. The light emission is peaked in the forward direction (angle to the shower axis $\lesssim 10°$) but light scattering in the atmosphere can lead to significant contributions also for large viewing angles. This additional light component can be used during the reconstruction of the shower profile [34] (see also Sec. 3.2.1).

The longitudinal shower profile shown in Fig. 2.1.4b has been observed by the pioneering experiment Fly's Eye [35]. It is still the highest energetic cosmic ray detected so far ($E \approx 3.2 \cdot 10^{20}$ eV [30]). The fluorescence technique has also been used very successfully

by the HiRes I + II experiment [36, 37], which were able to gather the largest event statistics before the Pierre Auger Observatory. A compilation of exposures obtained with different experiments is given in Fig. 2.2.10. Fluorescence telescopes will also be used in the upcoming Telescope Array [23].

An important enhancement of the reconstruction accuracy of EAS observed with fluorescence detectors is achieved by adding information from a surface array [38]. Especially the stability and precision of the geometrical reconstruction is increased for these *hybrid events*. Details will be discussed in Sec. 3.2.1.

2.2 Astroparticle physics at the highest energies

Over the last years the field of astroparticle physics, at the crossroads of elementary particle physics and astronomy, has evolved significantly towards a mature research area with great potential. High precision and high statistics experiments are about to open windows to both the universe and particle physics at extreme energies. Although promising prospects seem at hand, the available data on UHECRs does not yet allow one to draw conclusive answers on the most fundamental question about the origin of UHECRs. Being closely connected with each other, at least three domains of relevant information can be distinguished: *direct* source searches, studies of the chemical composition and interpretation of the energy spectrum.

2.2.1 Charged particle astronomy

Evidently the clearest way to discover the sources of UHECRs is the observation of deviations from isotropy of the arrival directions of cosmic rays. These deviations can occur on very different angular scales [39] and many suitable analysis methods have been developed over the last years to detect them (e.g. [40–42]).

Even though the actual acceleration mechanisms are unknown one can rely on very basic arguments to characterize possible source scenarios. In order to be able to accelerate charged particles they have to be at least partially confined into some 'acceleration region' and the maximum achievable energy E_{max} is given by

$$E_{\text{max}} \sim \beta_s \cdot Z \cdot B \cdot L \, , \tag{2.2.7}$$

with β_s being the characteristic velocity of particles or fields driving the acceleration in a shock front. Z is the charge of the accelerated particle and B the magnetic field needed to keep the particles inside the acceleration region of size L. This relation is the basis for the *Hillas plot* shown in Fig. 2.2.5a. Possible UHECR accelerators have to lie above the diagonal line and therefore only a few astrophysical objects like active galactic nuclei (AGN) or plasma-jets of radio galaxies remain possible candidates.

A main prerequisite for the possibility to use UHECR for astronomical observations is the conservation of the original particle direction during its travel from the source to the observer. Unfortunately charged cosmic rays are deflected by the galactic and extragalactic magnetic fields. The scale of the deflection is depending on a variety of variables like the strength of the B-field, its orientation and coherence length, the charge of the cosmic particle, and the distance between source and observer. All of these quantities are very poorly known

(a) possible sources   (b) magnetic deflections
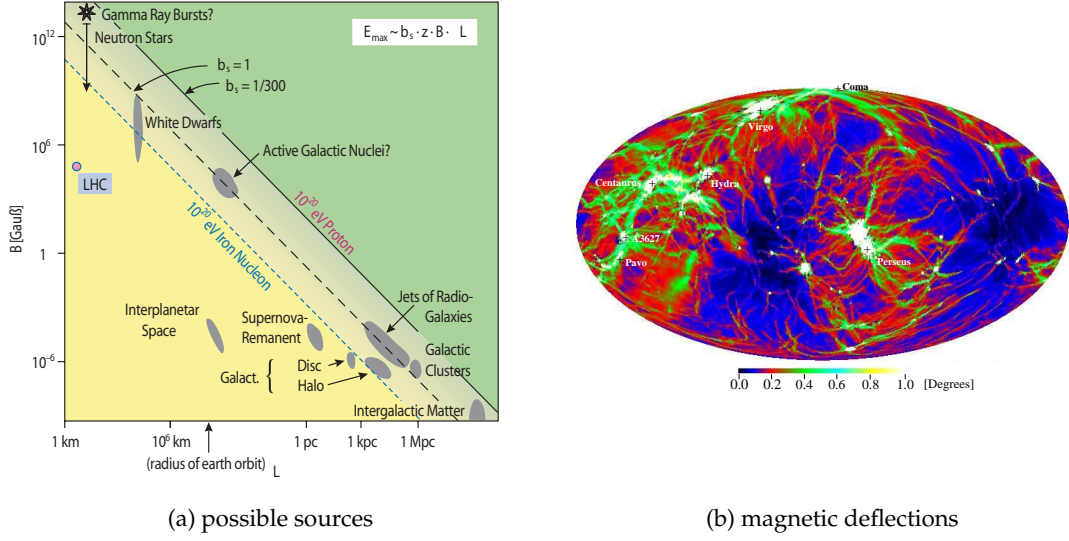
Figure 2.2.5: Two ingredients for charged particle astronomy: the required size and magnetic field strength of possible UHECR sources is limiting the source candidates (left panel [43]) and deflections in extragalactic magnetic fields might be small [44].

and are subject to intense debates. Nevertheless, assuming 'typical' parameter values for the extragalactic magnetic fields, protons at very high energies, and relatively close by sources, one can estimate the spread of the deflection in the extragalactic space as [45]

$$
\begin{aligned}
\alpha_{\text{rms}} &= 1.1^\circ\, Z \left(\frac{E}{10^{20}\text{eV}}\right)^{-1} \left(\frac{r}{10\text{Mpc}}\right)^{1/2} \left(\frac{l_c}{1\text{Mpc}}\right)^{1/2} \left(\frac{B}{10^{-9}\text{G}}\right) \qquad (2.2.8) \\
&\approx 6^\circ \quad (E = 56\text{ EeV};\ r = 75\text{ Mpc};\ l_c = 1\text{ Mpc};\ B = 1\text{ nG}) \,.
\end{aligned}
$$

More detailed MC simulations of large scale structure formation and the related build-up of magnetic fields enable much more detailed predictions for field configurations and particle deflections. The predicted cosmic ray deflections are shown in Fig. 2.2.5b. Unfortunately a significant difference is found between independent calculations [44, 46] and the order of magnitude of possible deflections remains uncertain.

A big step towards the discovery of the UHECR sources has been recently made by the Pierre Auger Collaboration [47, 48]. The highest energy events recorded so far were scanned for correlations with relatively nearby AGNs ($z \leq 0.024$ corresponding to $D \lesssim 100\text{ Mpc}$) listed in the Veron-Cetty/Veron catalogue [50]. AGNs where used only up to a maximal redshift z_{max}, which was a free parameter in the correlation scan. Two other free parameters were the minimal energy of the cosmic ray events E_{thr} and the maximum separation between reconstructed cosmic ray direction and the AGN position ψ. The scan was performed over data taken during the first two years of stable operation (01/2004 - 05/2006) and a significant minimum of the chance probability calculated assuming isotropic arrival directions was observed. After the parameters of this explorative scan ($z_{\text{max}} = 0.018$, $E_{\text{thr}} = 56\text{ EeV}$, $\psi = 3.1^\circ$) were fixed, the consecutive data set (06/2006-08/2007) was used to verify the correlation signal and the hypothesis of an isotropic source distribution could be rejected at more then 99 % confidence level. A sky map of the 27 events above the energy threshold of $E_{\text{thr}} = 56\text{ EeV}$
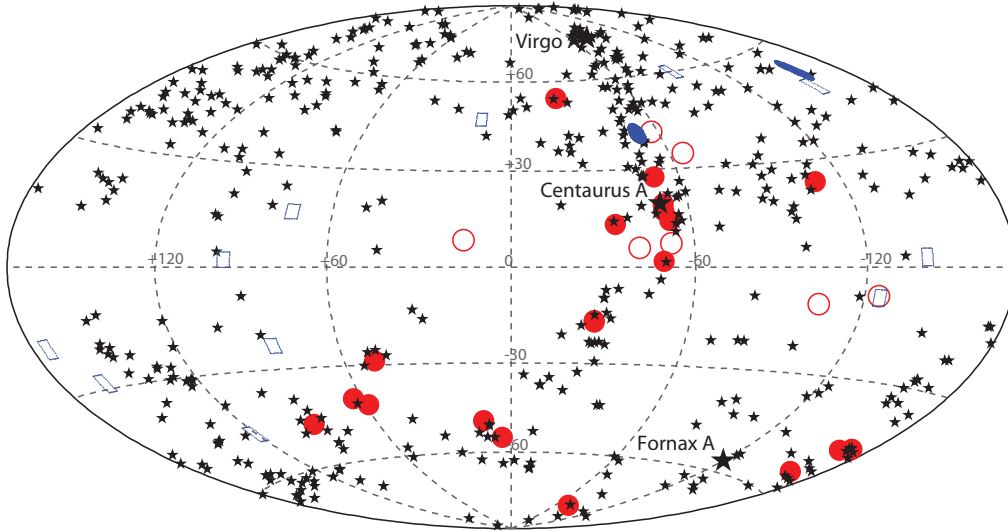
Figure 2.2.6: The sky seen with UHECRs with energies above 56 EeV detected with the surface array of the Pierre Auger Observatory (red circles, [47, 48]) and with the HiRes detector in stereo mode (blue squares, [49]) in galactic coordinates. Filled markers denote cosmic rays within $3.1°$ from AGN with redshift $z < 0.018$ (black stars, [50]).

together with the selected AGN is shown in Fig. 2.2.6. Also shown are the events selected during a follow-up analysis of stereo data from the HiRes experiment [49], which do not show a significant correlation.

The interpretation of the observed anisotropy is ongoing and a much larger event statistics will be needed to investigate, for example, whether the AGNs act only as tracers for the underlying true sources and whether the angular separation between AGN and UHECR can be related to magnetic deflections. Taken at face value, the correlation parameters are compatible with light particles originating from nearby extragalactic sources as deflections by magnetic fields of only a few degrees can only be explained assuming very light primary particles (cf. Eq. (2.2.8) or [51]).

This hypothesis of a dominant light mass composition of cosmic rays at ultra-high energies can be checked by independent mass composition analyses.

2.2.2 Primary mass composition

In direct measurements of elementary particles and cosmic rays at comparably low energies, the particle type can be determined on an event-by-event basis (e.g. [52]). This is not possible in typical hadron-induced EAS observations due to large shower-to-shower fluctuations. Analyzing rather large samples of recorded air showers the average mass compositions (typically as function of the energy) can be determined. Special analysis techniques, which allow to draw conclusion about the composition of very small samples of a few events only, are currently under discussion. One possibility has been developed during this work [51].

A strong correlation between air shower observables and the mass of the primary cosmic
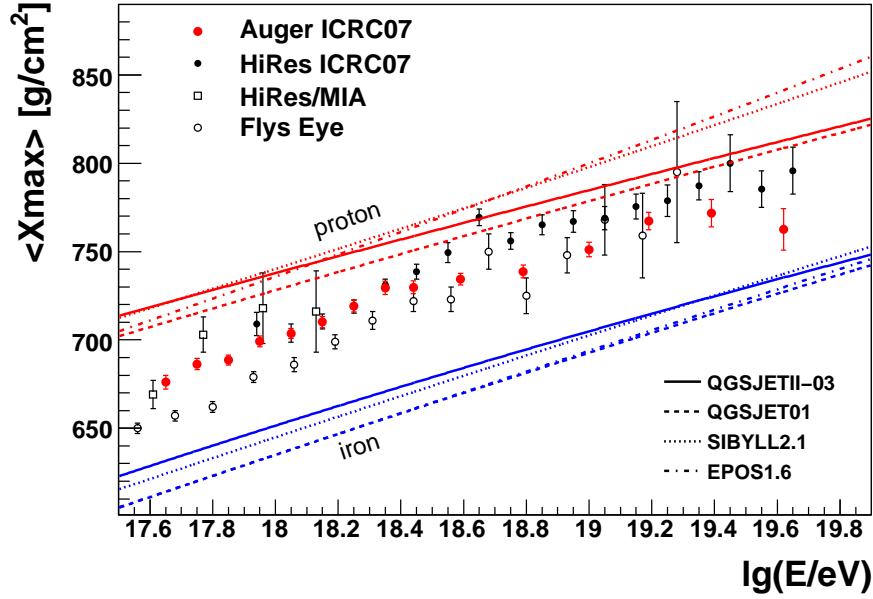
Figure 2.2.7: Measurements of $\langle X_{max} \rangle$ as function of energy from different experiments [53–55] compared to predictions from hadronic interaction models (plot from [56]).

ray is expected for the depth of the shower maximum X_{max} (cf. Eq. (2.1.6)). X_{max} is also easily accessible by fluorescence measurements (for details see Sec. 3.2.1). The last and crucial step is the interpretation of the measured $\langle X_{max} \rangle$ as function of energy into a primary mass composition. This is done by comparisons with predictions from shower simulations with hadronic interaction models and yields the biggest systematic uncertainty of this method.

A compilation of $\langle X_{max} \rangle$ measurements from fluorescence experiments together with predictions from hadronic interaction models are shown in Fig. 2.2.7. Although the available statistic is very limited, the measured $\langle X_{max} \rangle$ values at ultra-high energies ($\gtrsim 10^{19}$ eV) seem not to be compatible with proton simulations. On the other hand one would expect proton primaries from the interpretation of the observed correlation with AGN (see above). Given the limited statistics, the systematic uncertainties of the hadronic interaction models and the uncertainties in the interpretation of the AGN-correlation due to the unknown magnetic fields, these apparent inconsistencies cannot be resolved at the moment.

The problem of mass composition determination is much easier if the signature of the primary particles are very different from 'typical' hadronic showers. This is the case for photon and neutrino induced EAS. Photons showers penetrate much deeper into the atmosphere and, due to the very low photo-nuclear cross-section, only very few muons are created. These features have been employed to search for UHECR photons. So far no candidates were found and limits on the photon fraction were derived, for example, from data of the Pierre Auger Observatory [57,58]. These limits, sketched in Fig. 2.2.8a, severely challenge proposed alternative scenarios for the creation of UHECRs called top-down models. In these models the UHECR flux is made of secondary particles created in decays of superheavy particles left over from the very early phase of the universe, the collapse of topological defects, magnetic monopols, cosmic strings, etc.
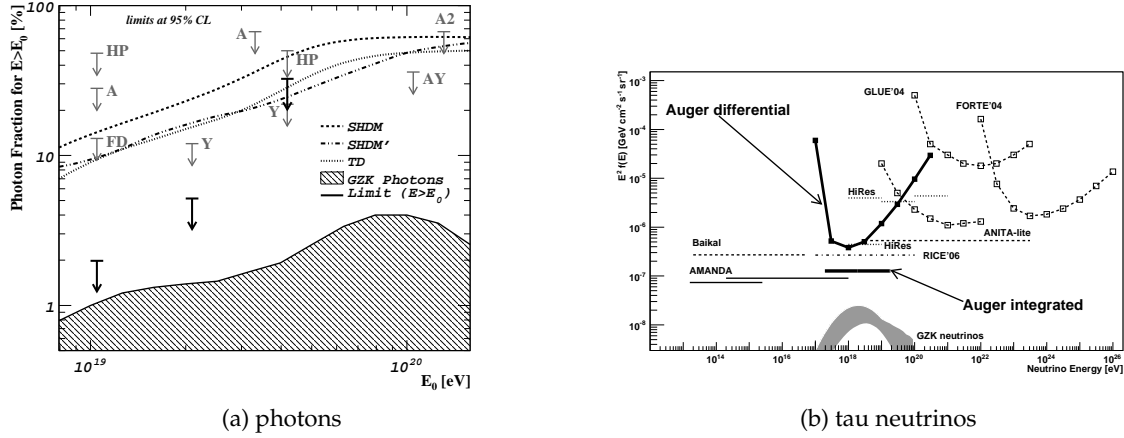
(a) photons   (b) tau neutrinos

Figure 2.2.8: Limits on the UHECR photon fraction (left panel, [58]) and on the tau neutrino flux (right panel, [59]).

Another very interesting possibility is the sensitivity of air shower detectors to ultra-high energy neutrinos. Neutrinos, which should be produced by basically all cosmic hadron accelerators, can travel undisturbed over long distances due to extremely small cross-sections. Their registration on Earth with reasonable rates would allow for detailed studies of the sources (e.g. [60, 61]) and propagation of UHECR (e.g. [62]). Neutrino detection with air shower observatories is based on the fact that neutrinos can interact very deep in the atmosphere or can cause upward going EAS after traveling through the Earth and interacting just below the surface ('Earth skimming neutrinos'). The predicted experimental signatures can be distinguished from hadronic showers and upper limits on the neutrino flux can be derived. The current status of these searches with very different techniques ranging from typical cosmic rays detectors like the Pierre Auger Observatory and HiRes to radio detectors on high altitude balloons like Anita is depicted in Fig. 2.2.8b. The flux predictions originating from the interaction between UHECRs and the microwave background, the GZK-process (see below), are also shown. The detection of this flux would be a very important step in the interpretation of the features observed in the UHECR energy spectrum.

2.2.3 The energy spectrum of cosmic rays

The third fundamental aspect of cosmic rays and another way to solve the *cosmic ray puzzle* is the study of the primary particle flux as function of energy, the *energy spectrum*. The flux of cosmic rays J as a function of energy is defined as

$$J(E) = \frac{\mathrm{d}^4 N}{\mathrm{d}E\,\mathrm{d}A\,\mathrm{d}\Omega\,\mathrm{d}t} \tag{2.2.9}$$

$$\cong \frac{1}{\Delta E}\frac{N^D(E)}{\mathcal{A}(E)\,\tau}, \tag{2.2.10}$$

where $N^D(E)$ is the number of detected events in the energy bin centered around E and having width ΔE. $\mathcal{A}(E)$ is the aperture of the detector, which is, in general, energy dependent. In the simplest case, i.e. detectors for which the trigger, reconstruction and selection
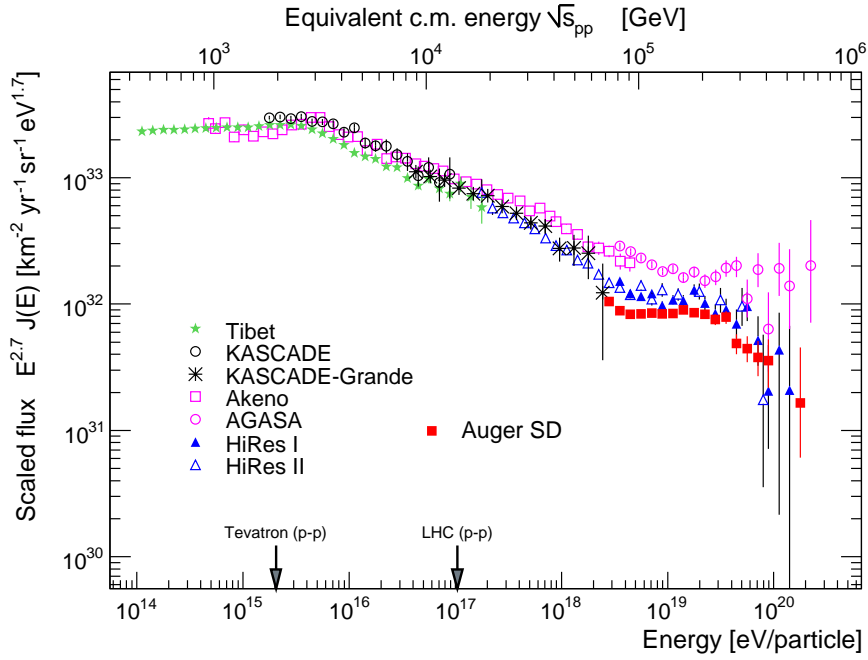
Figure 2.2.9: The flux of cosmic rays as determined by Tibet [28], KASCADE [27], KASCADE-Grande [63], Akeno/AGASA [64, 65], HiRes [66] and the surface array of the Pierre Auger Observatory [67].
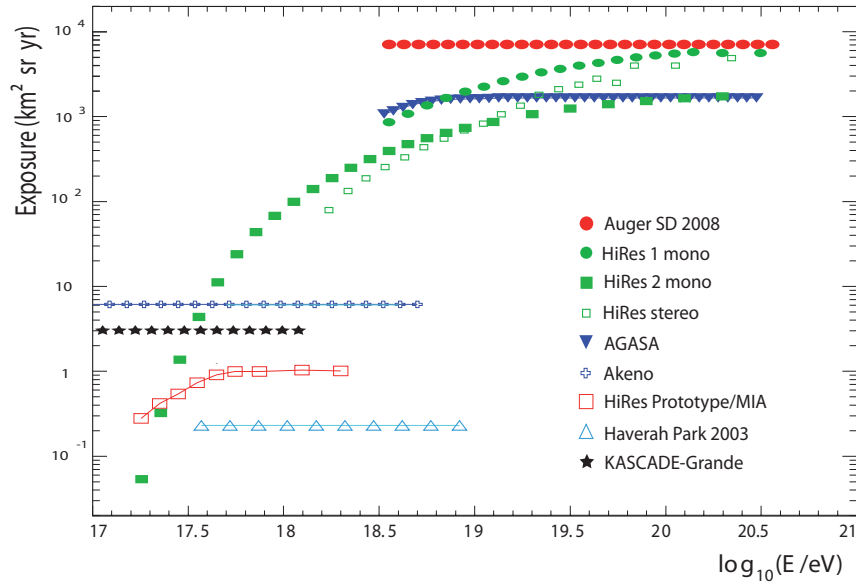
Figure 2.2.10: Exposures accumulated by different UHECR experiments (modified from [68]).

probability is independent of the energy, $\mathcal{A} = $ const. can be derived geometrically. This is for example the case for the surface array of the Pierre Auger Observatory above $3 \cdot 10^{18}$ eV (cf. Sec. 3.2). τ denotes the uptime, i.e. the effective data taking time of the detector and $\Delta\Omega$ the solid angle. The product $\mathcal{A}(E)\,\tau$ is usually referred to as the exposure $\mathcal{E}(E)$.

(a) mass measurements　　　　　　　(b) mass group spectra
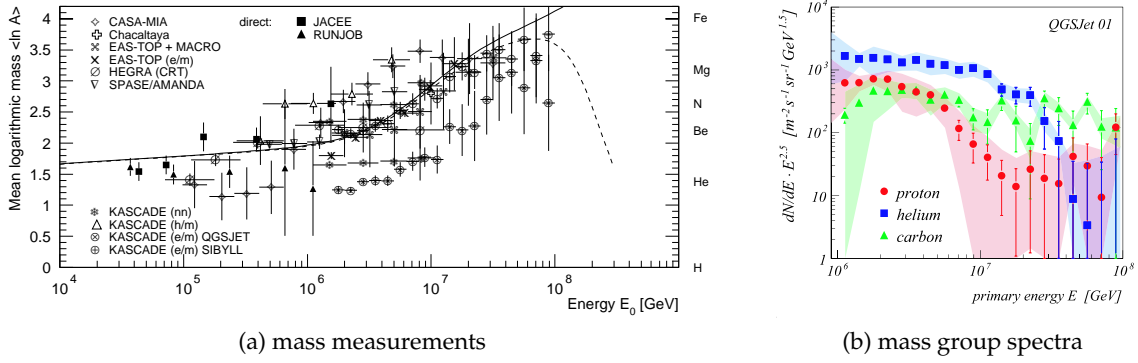
Figure 2.2.11: Measurements of the mean CR mass show a trend towards heavier elements just above the knee region (left panel, [77]). This trend is confirmed by the KASCADE experiment, which is able to resolve the cosmic ray spectrum into different mass groups [27].

Experimental situation and phenomenology

The determination of the cosmic ray flux is the first and for most of the experiments the main goal. Consequently there is a multitude of measurements already available. A representative set of recent measurements is shown in Fig. 2.2.9. The rather large statistical uncertainties are due to the limited exposure of the experiments which is shown in Fig. 2.2.10. The main property of the cosmic ray flux is its almost pure power-law behavior following roughly $J \propto E^{-\gamma} \sim E^{-3}$.

A first break of this power-law is visible between 10^{15} and 10^{16} eV, where the spectral index γ increases significantly from 2.7 to about 3.1. The KASCADE experiment was able to derive spectra of different mass groups [27]. As depicted in Fig. 2.2.11, the *knee* in the energy spectrum can be explained by a drop of light elements. Interpretation of this feature is subject to a wide range of proposals and has been extensively studied over the last years (e.g. [69–71]). Possible scenarios range from a change in the propagation of the charged cosmic rays in the galactic magnetic fields (e.g. [72,73]) to the inefficiency of the acceleration mechanism (e.g. [74]).

Given the knee is caused by light elements one would expect to observe another knee-like feature at the point where the heaviest elements, i.e. iron like nuclei, cannot be accelerated further or drop out of the confinement in the galactic magnetic fields. This *iron knee* should be in the energy range $10^{17} - 10^{18}$ eV and is being searched for by the KASCADE-Grande experiment [26]. There are indeed indications of a second knee but it is unclear whether this feature in the flux is related to the expected iron knee.

The next remarkable feature in the cosmic rays spectrum is a hardening above 10^{18} eV. First observations of this *ankle* have been reported by the Haverah Park [75] and Akeno [64] ground arrays and confirmed by the Fly's Eye [76] and HiRes [53] fluorescence detectors. The energy range of the ankle is also accessible by hybrid measurements of the Pierre Auger Observatory. The determination of its position and shape, using data of the Pierre Auger Observatory, will be a focus of this work.

Much attention has been paid both experimentally and theoretically to the existence of the predicted flux suppression at ultra-high energies due to the *GZK* effect. Shortly af-
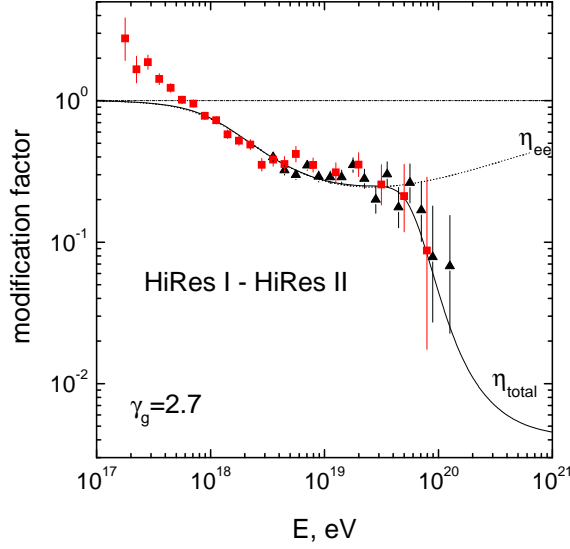
Figure 2.2.12: The *dip-model* is explaining the ankle in the energy spectrum by $e^+ - e^-$ pair production of protons in the cosmic microwave background radiation field [84].
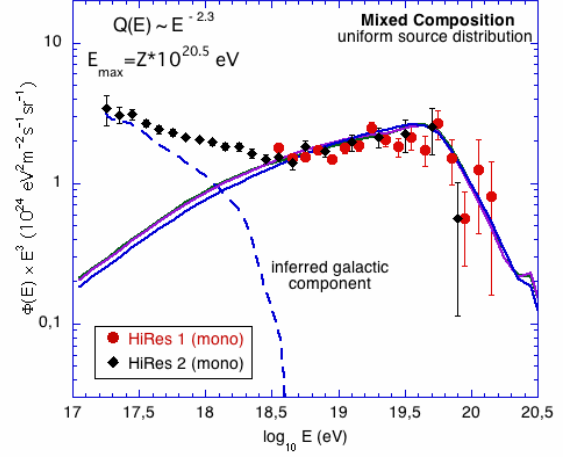
Figure 2.2.13: The *transition model* is explaining the ankle in the energy spectrum by the cross-over of the galactic and extra-galactic cosmic rays fluxes [85].

ter the discovery of the cosmic microwave background (CMB) by Penzias and Wilson [78], Greisen [79] and independently Zatsepin and Kuz'min [80] realized that interactions of ultra-high energy protons with energies above $10^{19.5}$ eV and photons from the 2.7 K background radiation should be able to excite a $\Delta(1232)$ resonance. This *GZK-effect* can be described as

$$p + \gamma_{2.7\,\mathrm{K}} \rightarrow \Delta^+(1232) \quad \rightarrow \quad n + \pi^+ \tag{2.2.11a}$$
$$\rightarrow \quad p + \pi^0 \tag{2.2.11b}$$
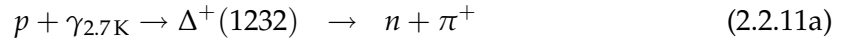
Above the threshold, an average energy loss of $\approx 20\,\%$ per interaction leads to significant energy losses and therefore to a strong suppression of the cosmic ray flux (cf. Fig. 2.2.14a).

It has been realized that also heavier nuclei suffer from energy losses while traveling over astronomical distances through the various radiation fields [79, 81, 82]. Of special importance is the possibility to excite the Giant Dipole Resonance, which dominates the photo-disintegration processes due to its high cross-section at low energies. The resulting energy loss lengths are shown in Fig. 2.2.14b. It is interesting to note that both the spectral features and the mass composition measurements can be explained assuming cosmological sources accelerating only iron nuclei [83] if the maximal achievable energy of these accelerators is relatively low.

During the last years it has been realized that a lot valuable information about the origin of UHECRs can be obtained by studying the ankle region. Currently two main phenomenological models to interpret the features observed in this energy range are pursued. They are closely related to different assumptions of the mass composition. In the first model put forward by Berezinsky et al. [84], the ankle is explained as an effect of proton energy losses in
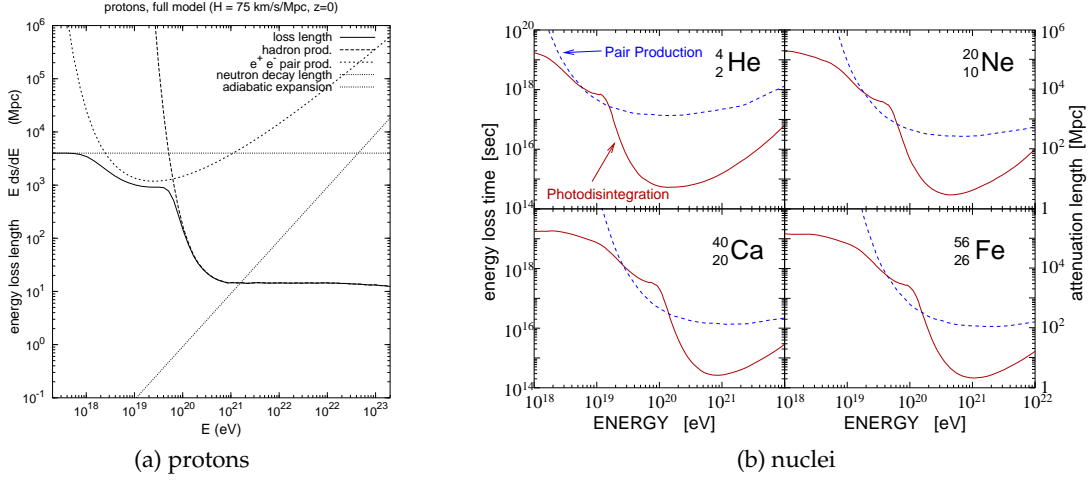
Figure 2.2.14: Energy loss length for extragalactic protons (left panel, [86]) and heavier nuclei (right panel, [87]).

the CMB due to Bethe-Heitler e^+e^- pair production,

$$p + \gamma_{2.7\,K} \rightarrow p + e^+ + e^- \ . \tag{2.2.12}$$

Only weakly depending on assumptions of the source evolution with redshift, a *dip* in the *modification factor* η, defined as the ratio of the final cosmic ray flux at earth ϕ_{Earth} over the flux one would get by adiabatic redshift related losses only:

$$\eta = \frac{\phi_{\text{Earth}}}{\phi_{\text{redshift only}}} \ . \tag{2.2.13}$$

The dip is centered at about 8×10^{18}eV and therefore able to explain the ankle feature in the cosmic ray energy spectrum (cf. Fig. 2.2.12). This process is only possible for UHECR protons and is therefore able to explain the ankle only if the flux of UHECRs is largely proton dominated. As shown in Fig. 2.2.7 this interpretation is challenged by recent observations of the Pierre Auger Observatory and a re-analysis of the HiRes data. Of course one has to keep in mind that the interpretation of the $\langle X_{\text{max}} \rangle$ measurements are based on available hadronic interactions models, which have large systematic uncertainties. Another important assumption of the dip-model is the very steep injection spectrum, which has to follow approximately $E^{-(2.5...2.7)}$ (cf. Fig. 2.2.12) in order to explain the spectral features at high energies. Extrapolating this steep spectrum to lower energies ($\lesssim 10^{17.5}$ eV) leads to extremely high energy requirements of the accelerator, which seems unnatural and a cut-off at low energies has to be introduced.

In the second model, which has been the standard interpretation of the ankle until recently, the ankle is explained as the transition from galactic to extragalactic spectra [88, 89]. In a recent calculation by Allard et al. [85], a mixed mass composition close to the abundances found in our solar system is assumed at the extragalactic acceleration sites. This mass composition is changing during the propagation due to proton energy losses and nuclei disintegration in interaction with the CMB. The ankle is interpreted as the transition between a

galactic and the propagated, mixed composition extragalactic component. It should be noted that this model has a rather large number of intrinsic parameters like initial mass composition at the sources, maximum energy the accelerator(s) can reach, etc. The agreement with current data above the ankle is good for both spectral and composition measurements (cf. Fig. 2.2.13 and [85]). On the other hand a currently unexplained additional galactic component is required to fill the energy range up to $> 10^{18}$ eV.

Due mainly to the lack of statistical power of the data, both models are able to explain the observed spectral features to good accuracy. The dip-model is preferring a smooth ankle compared to the transition model but precision and statistics of the data has to be increased significantly in order to make this distinction. Based on the UHECR spectrum derived in this work a first attempt of this discrimination will be discussed in Sec. 7.3. Further studies with the aim to falsify one of the proposed models would require more data on the evolution of the primary mass composition with energy.

Chapter 3

The Pierre Auger Observatory

The Pierre Auger Collaboration is building and operating the worlds largest detection system for ultra-high energy cosmic rays. The current status of the detector is illustrated in Fig. 3.1.1. As *hybrid-detector* the Pierre Auger Observatory combines a huge ground array with measurements of the fluorescence light produced by extensive air showers [6]. The simultaneous measurement of many independent variables is improving the event reconstruction quality and reduces the systematic uncertainty. In addition, the independent measurements enable important cross checks and calibrations.

To achieve full sky coverage two similar detectors, one on each hemisphere, were conceived. Construction of the first one (southern hemisphere, Province of Mendoza, Argentina) is completed and, in addition to enhancements of the baseline design of the southern detector [90,91], detailed design studies of the counterpart in the northern hemisphere (Colorado, USA) have begun [92]. In the following description emphasis is put on components relevant for the determination of the energy spectrum like the trigger functionality (Sec. 3.2) and the energy reconstruction of hybrid events (Sec. 3.2.1).

3.1 The southern Observatory

The almost complete surface detector (SD) array consists of about 1600 water Cherenkov detectors aligned in a triangular grid with 1.5 km spacing. It is covering an area of about 3000 km^2 (cf. Fig. 3.1.1). Each stand-alone detector is filled with 12 m^3 of ultrapure water and monitored by three 8 inch photomultiplier tubes (PMT), to detect the Cherenkov light pulses of charged particles traversing the water tank (cf. Fig. 3.2.2). Each detector is continously auto-calibrated by the Cherenkov signal of ambient atmospheric muons passing through the detector [94]. The energy assignment to detected air showers is done through a cross-calibration with the fluorescence detector [67].

After fulfilling dedicated trigger conditions, which will be discussed in Sec. 3.2, the tank signals are read out via radio communication. Due to its almost perfect independence of atmospheric conditions, the SD is able to collect data with a duty-cycle of nearly 100 %.

The fluorescence detector consists of 4 telescope buildings, overlooking the detector array (cf. Fig. 3.1.1). Each building houses 6 telescopes with a $30^\circ \times 28.6^\circ$ field of view (FOV)
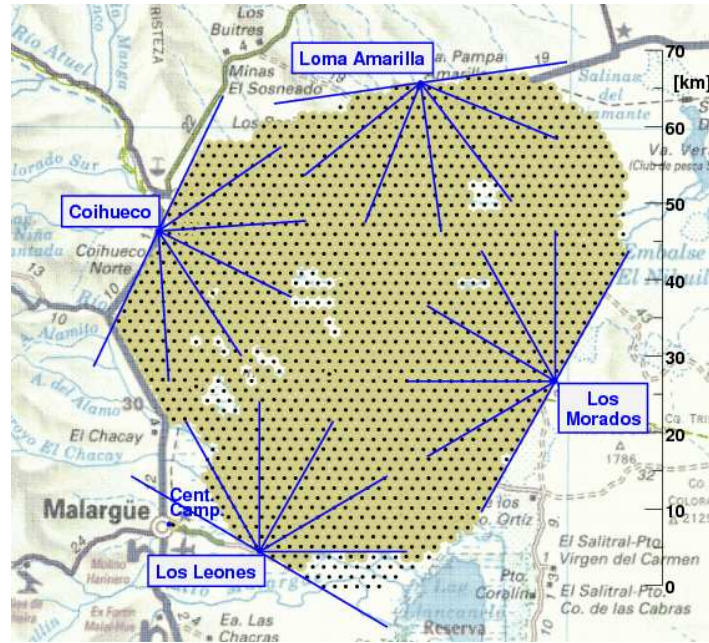
Figure 3.1.1: Map of the southern site of the Pierre Auger Observatory. The fluorescence detectors are marked in blue with lines indicating the field of view of the telescopes. The planned surface detectors are represented by black dots (already installed detectors are displayed as shaded area) [93].

as shown in Fig. 3.2.4, leading to a 180° azimuth angle coverage of each building (also called *eye*). The fluorescence light is focused through Schmidt-optics and a spherical mirror of $\approx 13\,\mathrm{m}^2$ onto a camera consisting of 440 photomultipliers. The signal of each PMT is digitized using analog to digital converters (ADCs) with a frequency of 10 MHz.

The detection of EAS is using the Earth's atmosphere as a calorimeter and, hence, environmental parameters are strongly influencing the measurements. A large atmospheric monitoring system is employed at the site of the Pierre Auger Observatory. Most important for the current analysis are the two laser facilities in the middle of the array (CLF and XLF, [95]) for aerosol measurements and the devices for cloud detection, i.e the Lidar systems [96] and infrared cameras at each fluorescence building. Details on cloud detection are given in the Appendix Sec. C.1. In regular time intervals weather balloons are launched to determine the atmospheric profile, i.e. temperature, pressure and humidity as function of height above the detector. In addition a horizontal attenuation monitor (HAM), an aerosol phase function monitor (APF), a high power Raman Lidar, several weather stations, a lightning detector and an automatic telescope system for star observations (FRAM) are available for atmospheric monitoring. The usage of the atmospheric parameters determined by these devices during event reconstruction is described in Sec. 3.2.4.

3.2   Air shower detection and reconstruction

Extensive air showers hitting the ground inside the Pierre Auger Observatory can potentially trigger several stations of the surface array. In order to discern these events from the
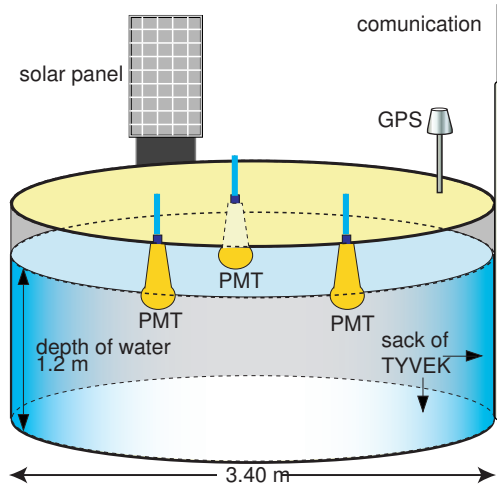
Figure 3.2.2: Schematic view of a surface detector filled with ultrapure water and monitored by three photomultiplier tubes.
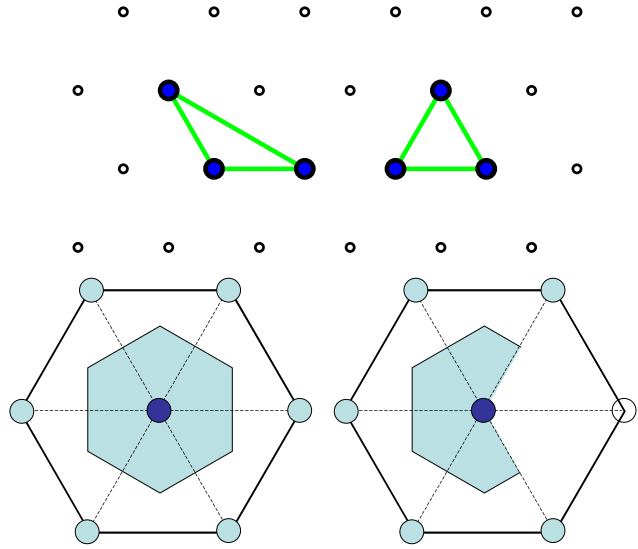
Figure 3.2.3: Two possible surface array trigger configurations (top, [97]) and the T5 quality criterion used to ensure an almost 100 % reconstruction efficiency and allow for an analytical aperture calculation (bottom, [98]).

random, mainly muon induced noise triggers occurring at about 100 Hz at the single station level, a 3-fold coincidence of neighboring tanks is required (3ToT-trigger). The two possible configurations are illustrated in Fig. 3.2.3 (top). The decision to readout the whole detector array is taken at the Central Data Acquisition System (CDAS). Extensive MC simulations and comparisons with fluorescence events have shown that the surface detector array becomes fully efficient for zenith angles $\leq 60°$ above $3 \cdot 10^{18}$ eV [98]. A quality criterion requiring at least 5 active stations around the one with highest signal has been introduced. This *T5-trigger* is ensuring a more than 99 % probability to reconstruct the event [99]. The T5-condition can also be used to limit the available detector area to a well defined surface, which can be calculated analytically by summing up active elementary cells of $a_{cell} = 4.59$ km^2 sr illustrated as shaded area in Fig. 3.2.3.

A main problem for surface detector arrays is the absolute energy calibration. Whereas the ambient muon flux is providing an online calibration at the single station level, one has to rely on MC simulations to relate the measured EAS signals to the energy of the primary cosmic rays. A big advantage for the surface array of the Pierre Auger Observatory is the possibility to cross-calibrate the surface detector signal with the almost calorimetric measurements of the fluorescence detector [67].

The fluorescence telescopes have an independent trigger system of several consecutive layers [100]. Acting on the lowest level of single PMTs or *pixels*, a threshold trigger with a running box-car sum over 1 μs is applied. The threshold of this 'First Level Trigger' (FLT) is auto-adjusting itself to assure a constant rate of about 100 Hz per PMT. In the next step the FLT triggered pixels have to follow a pattern consisting of connected pixels. This 'Second Level Trigger' (SLT) is fulfilled if at least four pixels belong to one of the basic patterns sketched in Fig. 3.2.5 or rotations of them are found.
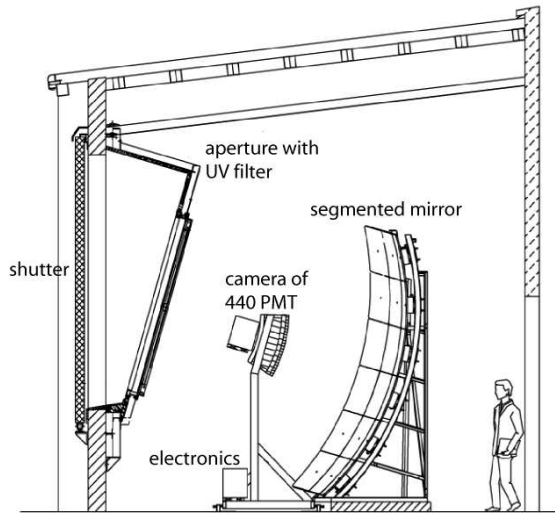
Figure 3.2.4: Schematic view of a fluorescence telescope showing the spherical mirror, the photomultiplier camera and the UV-filter.
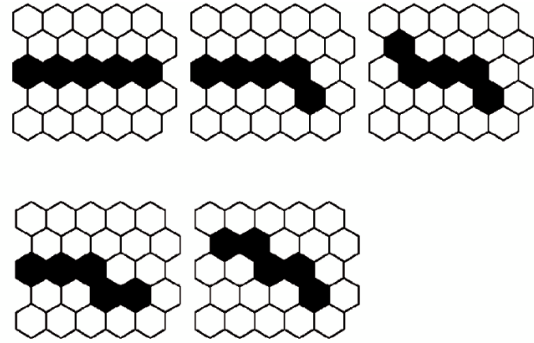
Figure 3.2.5: Basic topological pattern used by the Second Level Trigger [100].

To reject noise events caused mainly by lightning and muon hits on the camera two higher level triggers have been implemented in the data acquisition software of the fluorescence detector. The 'Third Level Trigger' (TLT) is using cuts on several variables like the FLT times of the triggered pixels to reduce the noise rate. It has been extensively studied and optimized [101, 102] and will be discussed in some detail in Sec. 5.1.3. The last trigger layer is the T3-algorithm. After collection of data from all telescopes within one building it performs a rough reconstruction of the event geometry and provides an approximate position and timing of the detected shower. This information is send to CDAS to trigger the readout of the surface array. This cross-trigger possibility is the core of the hybrid data taking of the Pierre Auger Observatory. It allows to gather tank signals of single tanks, which would not pass the SD trigger as described above. This data can be used to enhance the reconstruction of the fluorescence events and lower the energy threshold of the experiment. The merging of the independent data streams from surface and fluorescence detectors into 'hybrid' events is performed offline. Details on the FD-SD cross-trigger and the merging procedure will be discussed in Sec. 4.1.3.

Hybrid events have a lower energy threshold and a better energy resolution compared to surface detector data. They therefore allow for the determination of the cosmic rays flux in a broad energy range including the precise measurement of the ankle up to the flux suppression at the highest energies. Whereas surface detector data have to be cross-calibrated to achieve a reliable energy estimation, the flux determination based on hybrid events has its difficulty in the exposure determination. Due to strong dependencies on atmospheric conditions one has to rely on MC simulations and cannot use analytical calculations. The other drawback is the significantly lower statistics due to the limited duty-cycle of the fluorescence detector.

Routine data collection of the southern observatory has started in beginning of 2004. At that time only two fluorescence buildings ('Los Leones' and 'Coihueco') were operational.

Figure 3.2.6: The amount of collected hybrid data fulfilling basis quality criteria is increasing rapidly as the detector is nearing completion.
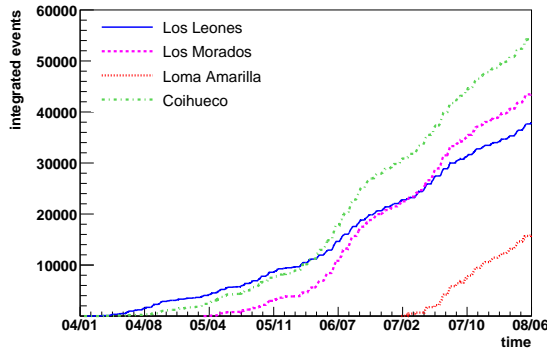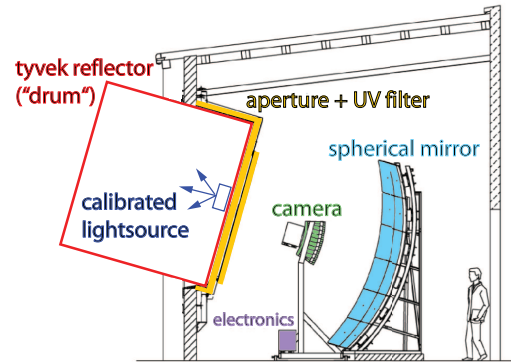

Figure 3.2.7: A calibrated light source is mounted at the telescope aperture during the absolute end-to-end calibration of the fluorescence detector.

The third eye ('Los Morados') was commissioned in early 2005 and the last eye ('Loma Amarilla') became operational in spring 2007. Data of this eye are not yet available for physics analysis due to technical problems. The amount of collected cosmic ray data is already compatible with or exceeds fore-runner experiments. An overview of exposures collected by different experiments is given in Fig. 2.2.10. The integrated number of hybrid events fulfilling basic quality criteria is shown in Fig. 3.2.6. Clearly visible is a seasonal dependence introduced by the longer winter nights, which leads to more time for fluorescence data taking. The small steps visible in Fig. 3.2.6 are reflecting the moon-cycles. FD data is restricted to periods with a moon-fraction of less then 60 %. The current data taking procedures are, in addition, requiring the closing of the telescope shutters if the position of the moon is within 5° of the telescope field of view to avoid damage of the photomultipliers. Between the measurement shifts data taking is stopped and the time is used for maintenance or calibration campaigns.

The calibration of the fluorescence detector is assured in a two-fold way. During absolute calibration campaigns a NIST-calibrated, Lambertian light source of 2.2 m diameter is mounted at the telescope aperture as depicted in Fig. 3.2.7 [103, 104]. The large homogenous surface is illuminating all camera pixels uniformly and the response of the data acquisition system to this known signal can be used to derive the required end-to-end calibration for each pixel.

The time evolution of this calibration is followed very closely by carrying out relative calibration measurements at the beginning and the end of each night of data taking (c.f. Sec. 5.1.2). In addition shots from a portable laser are recorded and used to verify the calibration. It has been realized that the calibration values have to be modified with time [105] in order to correct for a slow decline in sensitivity of some FD cameras. One possible explanation is the aging of the photomultipliers due to their exposure to, mainly background, light. Although the correlation between integrated charge, i.e. integrated noise exposure, and efficiency loss is not completely established [105], it has been decided within the collaboration to limit the operations of the detector to periods with low noise levels. Since the end

(a) FD efficiency loss

(b) time dependent calibration *constants*
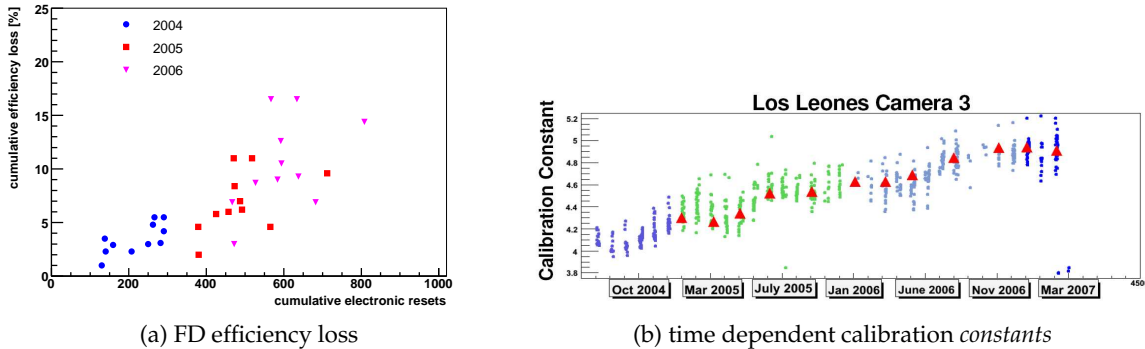
Figure 3.2.8: The observed loss of efficiency of several telescopes might be explained by the frequent resets of the front end electronics (left panel). The loss is taken into account by time dependent pixel calibration *constants* (right panel).

of 2007 the shutters are closing automatically if the camera averaged noise level, given by the average variance of the pixel baseline, is exceeding a limit of $\langle Var \rangle_{\mathrm{cut}} = 100 \, \mathrm{n}^2_{\mathrm{ADC}}$.

The efficiency loss might also be connected to the frequency of electronics resets. It happens sometimes that during data taking the monitoring data of the front end electronics shows abnormal behavior. In the early phase of the FD data taking the usual action taken by the shift crew was to reset the front end boards by ramping the high and low voltages down and cut the power supply of the boards for a limited time period. One might argue that the reboot of the system including the ramping of the high voltage of the PMTs is causing the efficiency loss. To check this hypothesis the number of electronic resets has been obtained from the FD monitoring system [106]. Unfortunately the determination of the efficiency loss requires large data samples and only an average yearly loss could be derived so far [105]. Comparing the integrated number of resets with the cumulative efficiency loss a correlation is found, see Fig. 3.2.8a. Note that, due to the use of the averaged efficiency loss, this correlation might just reflect the time evolution and not the expected dependency on the number of front end electronic resets. Since the beginning of 2007 the loss seems to be negligible [107]. Both the exposure to high background levels and the number of hardware resets have decreased since then and no conclusive answer on the cause of the observed loss can be derived. The pixel calibration constants are following this time evolution in several steps until 01/2007. Later, pixel calibration values are available on a nightly basis.

3.2.1 Hybrid event reconstruction

After an EAS triggered at least one FD telescope, the available information can be summarized as follows

- ADC-traces for each triggered pixel (ADC-counts as function of time, binned in 100 ns)

- pointing direction and calibration constant of each camera pixel

- position of the surface detector stations and timing of the signal

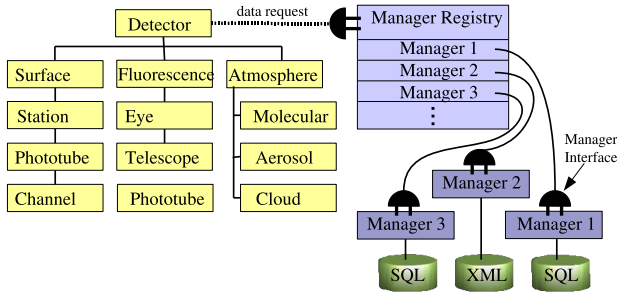Figure 3.2.9: In the $\overline{\text{Off}\underline{\text{line}}}$ framework various detector components are described with a hierarchical structure and access to the changing, i.e. time dependent, detector description is provided via common user interfaces or managers [108].
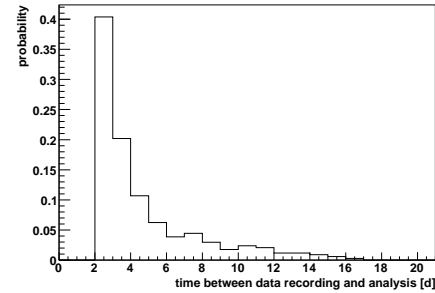

Figure 3.2.10: Due to automatic event reconstruction, which has been developed during this work [109], the time delay between data recording and analysis has become reasonably small.

- atmospheric conditions at the time of measurement (atmospheric profile, attenuation and scattering parameters, cloud coverage)

In the following, reconstruction of data from only one fluorescence detector station (*mono-reconstruction*) is considered. The additional information resulting from the possibility of the Auger Observatory to record the same air shower by different eyes is further improving the reconstruction accuracy. Due to limited statistics these *multi-eye* events are currently used only for cross-checks of the individual reconstructions, validation of the MC simulation (cf. Sec. 5.2) and studies of systematic uncertainties.

The reconstruction and simulation routines of the Pierre Auger Observatory are implemented in a common framework called $\overline{\text{Off}\underline{\text{line}}}$ [108]. The framework, which is developed inside the collaboration is providing access to different sources of additional information needed for the event reconstruction and simulation. This data (e.g. atmospheric monitoring information, calibration constants, etc.) can be stored in various formats ranging from simple XML-steering cards to ROOT-files and MySQL-databases. The access to these data sources is facilitated by 'managers' taking care of the actual data retrieval (cf. Fig. 3.2.9). Other main features of the framework are the modularization of the reconstruction and simulation chains and a sophisticated geometry package. Each step is implemented as a separate module and can therefore be exchanged and compared to competing algorithms very easily. The geometry package is assuring the reconstruction accuracy over the whole array. Due to the size of the Auger detector the curvature of the Earth's surface and atmosphere have to be taken into account [110].

The continuous flow of surface detector data is split into daily files and merged with fluorescence data if available. These *IoAuger*-files are then transfered to the computing center in Lyon (France) for longterm storage and distribution to smaller computing facilities like the one available for the Auger group in Karlsruhe. An automatic event reconstruction has been implemented in order to provide the Auger collaboration with a fully reconstructed dataset in a timely manner as part of the work for this thesis. The time between data taking and full reconstruction is illustrated in Fig. 3.2.10. To make the reconstruction results accessible in an easy way an output format called 'Advanced Data Summary Tree' (ADST, [111]) has

Figure 3.2.11: Data structure of the 'Advanced Data Summary Tree' (ADST, [111]), which has been developed to store all important reconstructed EAS parameters.

been developed. The format is constantly evolving and adjusted to the needs of the various analysis tasks of the Pierre Auger Observatory. The main structure is shown in Fig. 3.2.11.

3.2.2   Calibration and signal determination

As mentioned above, absolute and relative calibration procedures are assuring valid calibration constants. The time dependent calibration constants provided by the relative calibration procedures are stored in a SQL-database and available within the $\overline{\text{Off}}\underline{\text{line}}$ framework. Due to the end-to-end approach they allow one to translate the output of the readout electronics, i.e. ADC counts, directly into the number of detected photons at the telescope aperture. In the first step of the event reconstruction the baseline and its RMS of the recorded signals is calculated and the ADC-trace is converted into number of photons by applying the calibration constants of each pixel.

A *signal over noise* (S/N) maximization algorithm is used to determine the actual EAS signal inside the recorded trace. Starting from the time of the First Level Trigger, the so called *first triggered time bin*, the boundaries of the suspected pulse (start and stop time bin, i_{start} and i_{stop} respectively) are shifted to find the maximal S/N-ratio defined as

$$S/N = \frac{S(\Delta t)}{\sqrt{\Delta t} \times \text{RMS}} \ . \tag{3.2.1}$$

$S(\Delta t)$ is the total signal within the assumed pulse length and $\Delta t = (i_{\text{stop}} - i_{\text{start}})$.
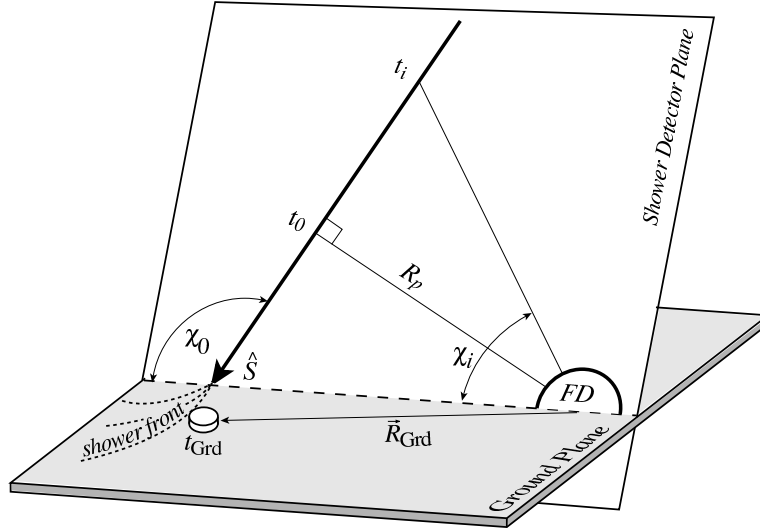
Figure 3.2.12: Data from the surface array and the fluorescence measurements are combined to increase the reliability and accuracy of the shower geometry reconstruction.

In order to reject accidental noise pixels triggered by background radiation, a minimum requirement on this ratio is set and usually only pixels with pulses having a S/N greater than five are kept for the following processes. For further analysis only the *pulse time*, T_i, of pixel i, defined as the centroid of the found pulse, and the total integrated signal, called 'pixel charge', will be needed.

3.2.3 Reconstruction of the EAS geometry

In the subsequent reconstruction step a Hough-transformation pattern recognition algorithm is used to determine all pixels connected to the shower image and further suppress noise pixels. With the remaining pixels and their geometrical pointing direction, $\vec{p}_i$, (determined by the alignment of the camera and verified for example by analyzing star tracks [112]) the plane containing both the air shower and the track on the camera, called shower-detector-plane (SDP), is determined by minimizing

$$Q^2 = \sum_i q_i \cdot \frac{\frac{\pi}{2} - \arccos(\vec{n}_{\text{SDP}} \cdot \vec{p}_i)}{\sigma_i^2} \, , \tag{3.2.2}$$

with q_i being the total signal of pixel i. The uncertainty $\sigma_i = 0.35°$ has been determined with reconstructed CLF laser shots. $\vec{n}_{\text{SDP}}$ denotes the desired vector normal to the SDP. After the SDP has been determined the pointing direction, $\vec{p}_i$, of each pixel can be translated into an elevation angle $\tilde{\chi}_i$ inside the SDP and the minimization of the following χ^2 leads to the determination of the position of the shower axis (for details see [35, 113])

$$\chi^2 = \sum_i \left[\frac{t(\chi_i) - t_i^{\text{meas}}}{\sigma(t_i)} \right]^2 \, . \tag{3.2.3}$$
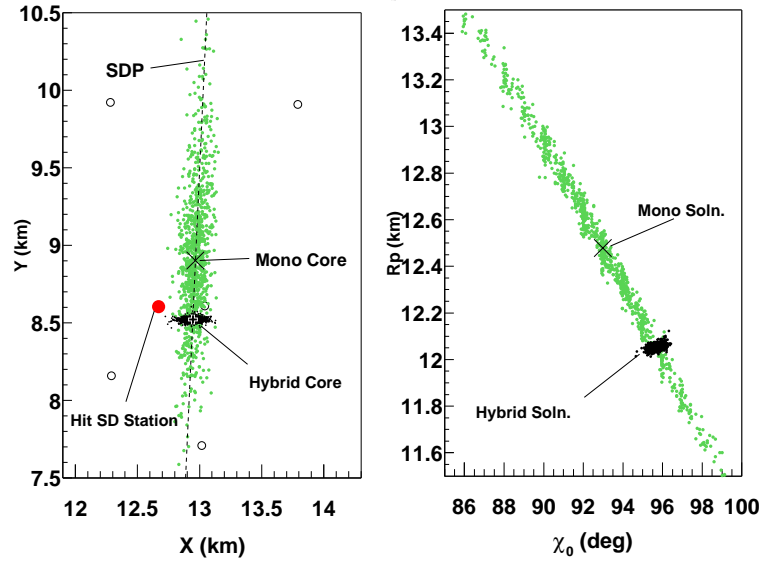
Figure 3.2.13: The strong correlation between the reconstructed parameters describing the geometry of the air shower can be removed in hybrid reconstructions. The use of additional timing information from the surface array is also increasing the accuracy significantly (from [114]).

t_i^{meas} is the measured pulse time of pixel i with the corresponding error σ_i. $t(\chi_i)$ denotes the theoretical expectation and can be derived from geometrical considerations (cf. Fig. 3.2.12):

$$t(\chi_i) = T_0 + \frac{R_p}{c} \cdot \tan\left(\frac{\chi_0 - \tilde{\chi}_i}{2}\right) \ . \tag{3.2.4}$$

The impact parameter R_p, the corresponding time T_0 and the angle between the shower axis and the ground plane χ_0 are free parameters to be determined during the minimization process. They are highly correlated and can usually only be determined with large uncertainties. If the signal of at least one surface detector station is available it can be used to further constrain the 3-parameter fit by adding a term to the χ^2 calculation (3.2.3), which becomes

$$\chi^2 = \sum_i \left[\frac{t(\chi_i) - t_i^{\text{meas}}}{\sigma(t_i)}\right]^2 + \left[\frac{t(\chi_{\text{SD}}) - t_{\text{SD}}^{\text{meas}}}{\sigma(t_{\text{SD}})}\right]^2 \ . \tag{3.2.5}$$

As illustrated in Fig 3.2.13 this hybrid reconstruction breaks the correlation of the parameters and increases the accuracy significantly [38]).

3.2.4   Energy reconstruction

To estimate the total light received at the aperture of the fluorescence telescope the optimal width ξ of the shower image on the camera is determined using a signal-over-noise maximization algorithm [115]. Integrating the signal of all pixels inside the circle with radius ξ one can derive the number of photons at the telescope aperture as a function of time, $N_\gamma^{\text{ap}}(t)$.

(a) fluorescence light   (b) Cherenkov light
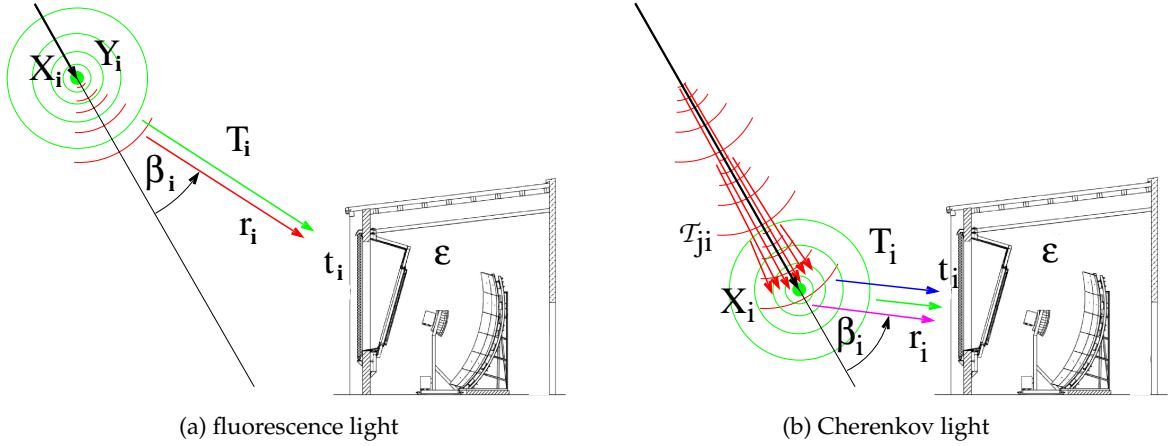
Figure 3.2.14: The reconstruction of the longitudinal shower profile has to account for direct (left panel) and scattered light (right panel) contributions. The recorded light flux is composed of the isotropically emitted fluorescence light (green) and the direct (red) Cherenkov light. In addition also scattered fluorescence (blue) and Cherenkov (magenta) components are considered. [34, 116]

This light flux is composed of three main components: fluorescence light, direct and scattered Cherenkov light. Fluorescence light is emitted by nitrogen molecules in the wavelength band between 300 nm and 400 nm. It is to a very good approximation directly proportional to the energy deposit dE/dX of the electromagnetic particles in the air shower[*]

$$N_\gamma^f(X_i) = Y_i^f \, \frac{dE_i}{dX} \, \Delta X_i \,. \tag{3.2.6}$$

The fluorescence yield Y_i^f is depending on the temperature, pressure [31–33, 117] and, as noticed only recently, on the relative humidity [118, 119]. The current systematic uncertainties of the absolute yield of about 14 % is currently the most important contribution to the energy scale uncertainty of the Pierre Auger Observatory.

As the secondary shower particles have rather high energies ($\mathcal{O}(100\,\mathrm{MeV})$), they emit Cherenkov light while passing through the atmosphere. Peaked in the forward direction a significant 'Cherenkov-light-beam' is building up along the shower axis. Due to the high intensity of this beam, multiple scattering into the field of view of the telescope becomes non-negligible even for geometries where the Cherenkov light cone would not be directly visible (cf. Fig. 3.2.14b). The intensity of Cherenkov light is directly proportional to the number of electrons and positrons N_e above the Cherenkov threshold energy [120]

$$N_\gamma^c(X_i) = Y_i^c \, N_e \, \Delta X_i \,. \tag{3.2.7}$$

The produced light itself is affected by the atmospheric conditions and several light attenuation factors have to be considered. Denoting the distance between the shower and the detector with r_i, a geometrical attenuation factor

$$\mathcal{T}_{\mathrm{geo}} = \frac{\epsilon \, A}{4\pi r_i} \tag{3.2.8}$$

---

[*]In the following the energy deposit and number of photons is considered in a depth segment of ΔX_i along the shower axis.

(a) distance dependence   (b) energy dependence
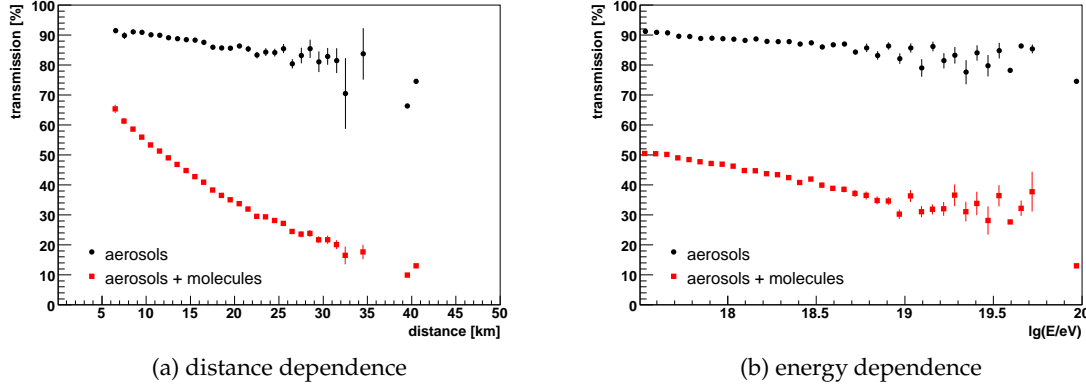
Figure 3.2.15: The transmission coefficients $\mathcal{T}$ due to absorption and light scattering on aerosols and molecules are naturally depending on the light travel distance (left panel). As high energy EAS can be detected to greater distances from the telescope, the mean transmission coefficient used during the reconstruction is energy dependent (right panel).

has to be considered. ϵ denotes the light detection efficiency of the telescope system including the transmissivity of the UV-filter, the mirror reflectivity and the PMT sensitivity and $A \approx 7\,\text{m}^2$ is the aperture of the telescope.

Light attenuation in the atmosphere can be decomposed into two main parts, a *molecular* and an *aerosol* component. The molecular component, i.e. Rayleigh scattering at nitrogen and oxygen molecules over a slant depth distance ΔX, and its wavelength dependence can be expressed analytically as

$$\mathcal{T}_{\text{Ray}} = \exp\left[-\frac{\Delta X}{X_0} \cdot \left(\frac{400\,\text{nm}}{\lambda}\right)^4\right] , \qquad (3.2.9)$$

where X_0 is the Rayleigh attenuation length at a reference wavelength of $\lambda = 400\,\text{nm}$. The actual implementation in the Offline framework is based on a model from Bucholtz [121], which takes into account the anisotropy of the air molecules.

The aerosol, or Mie attenuation $\mathcal{T}_{\text{Mie}}$ on the other hand can be in a first approximation factorized into wavelength dependent and independent parts

$$\mathcal{T}_{\text{Mie}}(h, \lambda) = \mathcal{T}_{\text{Mie}}(h) \cdot \mathcal{T}_{\text{Mie}}(\lambda) . \qquad (3.2.10)$$

The height dependent part $\mathcal{T}_{\text{Mie}}(h)$ can be written as

$$\mathcal{T}_{\text{Mie}}(h) = \frac{\Delta L / l_{\text{mie}}}{\Delta h / h_{\text{mie}}} \cdot \left[\exp\left(-\frac{h_{\text{emission}}}{h_{\text{Mie}}}\right) - \exp\left(-\frac{h_{\text{detection}}}{h_{\text{Mie}}}\right)\right] , \qquad (3.2.11)$$

where l_{Mie} is the aerosol horizontal attenuation length and h_{Mie} is the aerosol scale height. The light is emitted at height h_{emission} and travels over a distance ΔL to the detector at height $h_{\text{detection}} = h_{\text{emission}} - \Delta h$. Both h_{Mie} and l_{Mie} are determined by the observation of vertical laser shots with the fluorescence telescopes. The detected laser light profiles are compared to reference profiles, recorded in clear, i.e. aerosol-free, nights. The wavelength dependence

(a) 3D event overview

(b) reconstructed long. profile
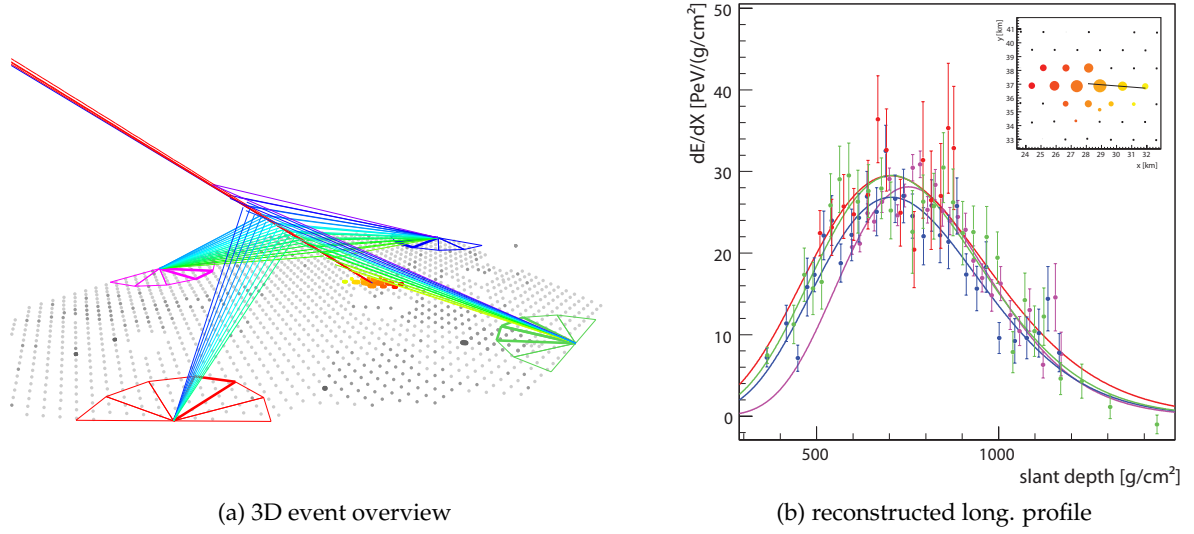
Figure 3.2.16: Example of an EAS detected by all four fluorescence detectors and the surface array simultaneously. The independent reconstructions can for example be used to verify the reconstruction algorithms.

of aerosol scattering is depending on the size and shape of the particles and cannot be calculated analytically. It is typically parameterized as

$$\mathcal{T}_{\mathrm{Mie}}(\lambda) = \mathcal{T}_0 \cdot \left(\frac{\lambda_0}{\lambda}\right)^{\gamma} , \tag{3.2.12}$$

where γ is called the Ångstrøm coefficient and $\lambda_0 = 355\,\mathrm{nm}$ is the reference wavelength used for the Pierre Auger Observatory. During FD data taking hourly attenuation measurements are performed at 5 different wavelengths between $350\,\mathrm{nm}$ and $550\,\mathrm{nm}$ (the region where the efficiency of the telescope is maximal) with the Horizontal Attenuation Monitor (HAM), sending high intensity light pulses over a distance of about $45\,\mathrm{km}$ from the Coihueco to the Los Leones detector site. An average factor of $\gamma = 0.7 \pm 0.6$ [122] is currently used in data analysis.

All these transmission factors are taken into account during the reconstruction of the energy deposit at the shower as a function of traversed depth. The dependence of the transmission factors on the light travel distance is shown in Fig. 3.2.15a. As high energy showers are visible further away this dependence is also reflected in an energy dependence of the mean transmission factors used in the reconstruction (cf. Fig. 3.2.15b).

Based on the measured light flux and with the knowledge of the atmospheric correction factors, the *longitudinal shower profile* (cf. Fig. 3.2.16b) is calculated with a novel matrix algorithm, which uses both light types, fluorescence and Cherenkov, as signal and derives the energy deposit profile in an analytical least-square minimization [34, 123]. Abbreviating the product of the transmission factors from Eq. (3.2.8), (3.2.9) and (3.2.10) with $T = \mathcal{T}_{\mathrm{geo}} \cdot \mathcal{T}_{\mathrm{Ray}} \cdot \mathcal{T}_{\mathrm{Mie}}$, the detected fluorescence light flux y_i^f can be written as (cf. Eq. (3.2.6))

$$y_i^f = T_i\, w_i\, \Delta X\, Y_i^f , \tag{3.2.13}$$

$w_i = \mathrm{d}E_i/\mathrm{d}X$ denotes the energy deposit per unit depth. Given the fraction $f_c(\beta_i)$ of Cherenkov photons per solid angle emitted at an angle β_i with respect to the shower axis due to multiple scattering [124, 125], the light flux at the detector originating from direct Cherenkov light is

$$y_i^{cd} = T_i \, f_c(\beta_i) \, Y_i^c \Delta X_i N_i^e \, . \tag{3.2.14}$$

Neglecting the lateral distribution of the Cherenkov photons, the number of photons in the beam at depth X_i is the sum of Cherenkov light photons at all previous depths X_j. On their way from X_j to X_i they are attenuated by T_{ji}

$$N_\gamma^{\text{beam}}(X_i) = \sum_{j=0}^{i} T_{ji} \, Y_j^c \, \Delta X_j \, N_j^e \, . \tag{3.2.15}$$

Similar to the direct contributions, the Cherenkov light scattered to the detector y_i^{cs} can be written as

$$y_i^{cs} = T_i \, f_s(\beta_i) \sum_{j=0}^{i} T_{ji} \, Y_j^c \, \Delta X_j \, N_j^e \, . \tag{3.2.16}$$

A precise knowledge of the angular dependence of the scattering cross-section, the 'aerosol phase function', is measured at a regular basis as part of the atmospheric monitoring program of the Pierre Auger Observatory [126].

The total recorded light flux is then given by the sum of the direct and scattered contributions

$$y_i = y_i^f + y_i^{cd} + y_i^{cs} \, . \tag{3.2.17}$$

As the total energy deposit along the shower development is just the sum of the electron energy losses, w_i and N_i^e are related via

$$w_i = N_i^e \int_0^\infty f_e(E, X_i) w_e(E) \mathrm{d}E \, . \tag{3.2.18}$$

$f_e(E, X_i)$ denotes the normalized electron energy distribution, which does not depend on the primary energy or mass but is universal in shower age [120, 125, 127]

$$s_i = \frac{3}{1 + 2X_{\max}/X_i} \, . \tag{3.2.19}$$

Due to this universality one can use the known energy deposit $w_e(E)$ of a single electron with energy E and parameterize the integral $\alpha_i = \int_0^\infty f_e(E, X_i) w_e(E) \mathrm{d}E$ (cf. Fig. 3.2.18, [125]). The obtained one-to-one relation

$$w_i = N_i^e \, \alpha_i \tag{3.2.20}$$

can now be used to merge the terms in Eq. (3.2.17) and a direct relation between the light collected at the detector y_i and the energy deposited by the air shower w_i can be formulated as matrix equation

$$\mathbf{y} = \mathbf{C} \cdot \mathbf{w} \, . \tag{3.2.21}$$

The developed algorithm is calculating the solution to this problem via the inversion of the *Cherenkov-fluorescence matrix* $\mathbf{C}$ in an analytical and fast way [116]. It also takes into account the wavelength dependence of the different transmission factors, efficiencies, etc..
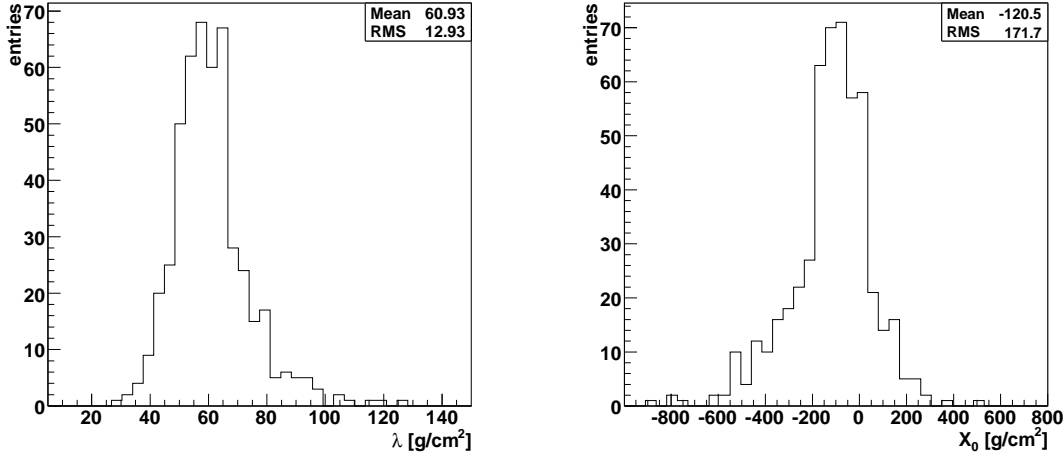
Figure 3.2.17: Highest quality hybrid events can be used to derive average values of the Gaisser-Hillas parameters Λ and X_0, which are used to constrain the profile fit (from [116]).

The derived longitudinal energy deposit profile covers only the observed range inside the field of view of the detector. To extend the shower profile outside the field of view a simple parametric description of the longitudinal evolution of air showers called Gaisser-Hillas function [128]

$$f_H(X) = (dE/dX)_{max} \cdot \left(\frac{X - X_0}{X_{max} - X_0} \right)^{\frac{(X_{max} - X_0)}{\Lambda}} \cdot \exp \left[\frac{X_{max} - X}{\Lambda} \right] \qquad (3.2.22)$$

is used. A fit of this four-parameter function is only reliable for profiles which have been observed over a very long range and having the shower maximum in the field of view. The problem of insufficient experimental information for the reconstruction of all four parameters can be overcome by constraining the two shape parameters denoted X_0 and Λ to their average values during the fit. The corresponding χ^2 is

$$\chi^2 = \sum_i \frac{(y_i - f_{GH})^2}{V_{y_i}} + \frac{(\Lambda - \langle \Lambda \rangle)^2}{V_\Lambda} + \frac{(X_0 - \langle X_0 \rangle)^2}{V_{X_0}} . \qquad (3.2.23)$$

V_{y_i} denotes the variance of the reconstructed energy deposit which has been derived by propagating the uncertainties from the pulse determination and the light collection. $\langle \Lambda \rangle$, $\langle X_0 \rangle$ and V_Λ, V_{X_0} are the mean and variance of the shape parameters, which have been determined from a set of highest quality hybrid events (cf. Fig. 3.2.17). Unfortunately the precision to determine these constrains is limited by the available event statistics. The influence of the currently used constrains on the energy reconstruction has been studied with high statistics MC simulations and will be discussed in Sec. 5.2.

Given a successful profile extrapolation, the determination of the total energy deposit of the shower in the atmosphere E_{cal} is given by the integral over the energy deposit profile:

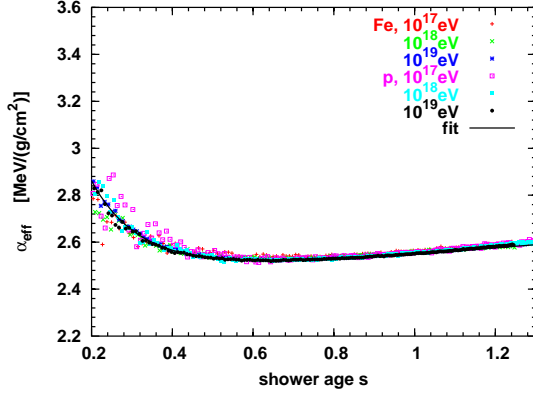$$E_{cal} = \int_0^\infty f_{GH}(X) \, dX . \qquad (3.2.24)$$

Figure 3.2.18: CORSIKA [129] simulation of the energy deposit per electron as function of shower age for different primary energies and particles. The black line denotes the parameterization of the average energy deposit (from [125]).
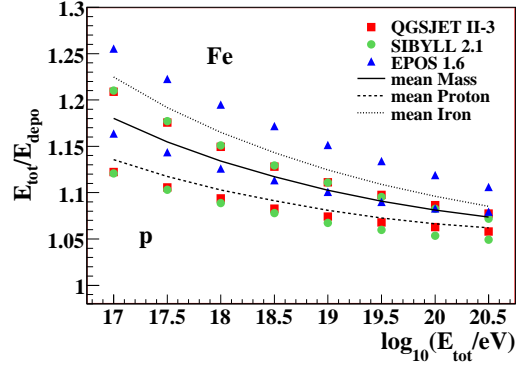
Figure 3.2.19: Invisible energy conversion factor for different hadronic interaction models derived from CONEX [130] simulations (from [131]).

This integral can be solved analytically with the use of the parameter transformation

$$t = \frac{X - X_0}{\lambda} \quad \text{and} \quad w = \frac{X_{\max} - X_0}{\lambda} \tag{3.2.25}$$

in the Gaisser-Hillas function (3.2.22), which leads to

$$f_{\mathrm{GH}}(t) = \mathrm{d}E/\mathrm{d}X_{\max} \cdot \left(\frac{e}{w}\right)^w e^{-t} t^w , \tag{3.2.26}$$

and can be identified with a Gamma distribution Γ. Therefore the above integral is given by

$$E_{\mathrm{cal}} = \mathrm{d}E/\mathrm{d}X_{\max} \cdot \lambda \cdot \left(\frac{e}{w}\right)^w \Gamma(w+1) , \tag{3.2.27}$$

where Γ denotes the Gamma-function. An advantage of this calculation is the possibility to directly estimate the statistical uncertainty of E_{cal}, which can be taken as free parameter in the fit (replacing $\mathrm{d}E/\mathrm{d}X_{\max}$):

$$f_{\mathrm{GH}}(t) = E_{\mathrm{cal}} e^{-t} t^w \Gamma(w+1) \tag{3.2.28}$$

The derived calorimetric or 'electromagnetic' energy estimation has to be corrected for the energy carried away by high energy muons and neutrinos. The total energy deposited by the air shower, i.e. the energy of the primary cosmic particle is therefore

$$E_{\mathrm{tot}} = f_{\mathrm{inv}} E_{\mathrm{cal}} . \tag{3.2.29}$$

The correction factor f_{inv} is a function of the calorimetric energy and has been derived from air shower simulations (cf. Fig. 3.2.19). Its systematic uncertainty is 4 % [131]. A detailed discussion will be given in Sec. 5.1.5.

Other uncertainties arise from the propagation of the uncertainties of the shower geometry. The shower position with respect to the detector is influencing the transmission

Figure 3.2.20: The pull distributions of energy and X_{max} determined by Monte Carlo simulations demonstrate the reliability of the uncertainty estimation (from [34]).

factor $T = \mathcal{T}_{\text{geo}} \cdot \mathcal{T}_{\text{Ray}} \cdot \mathcal{T}_{\text{Mie}}$ and therefore the energy deposit profile. The uncertainty of the shower direction, especial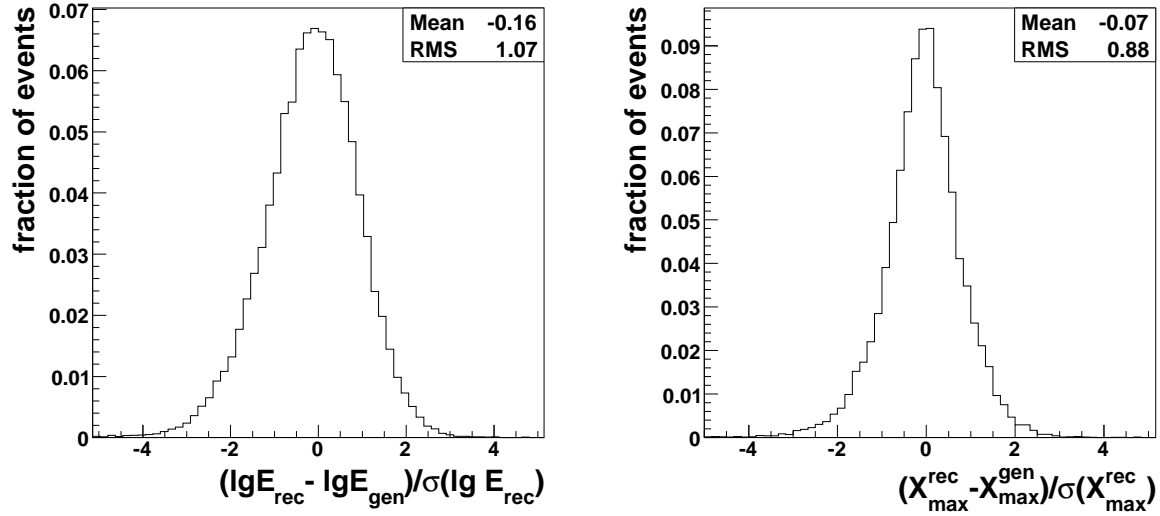ly the zenith angle θ, effects the slant depth calculation via $X_{\text{slant}} = X_{\text{vert}} / \cos \theta$ and thus X_{max}, which then leads to a different shower age and a different Cherenkov electron energy spectrum (cf. Eq. (3.2.18) and Fig. 3.2.18). Both effects are not accessible analytically and are calculated by reconstructing the longitudinal profile 6 times based on different shower geometries. The same approach is used to incorporate the uncertainties of the atmospheric parameters.

The achievable reconstruction accuracy, i.e. the energy resolution of the hybrid measurements, has been derived based on extensive Monte Carlo simulations and cross-checked with events that are observed by more than one fluorescence detector (cf. Sec. 5.2). The reliability of the uncertainty estimation can be seen in the pull-distributions shown in Fig. 3.2.20.

3.2.5 Systematic uncertainties of the energy scale

The energy estimation of fluorescence measurements is relying on the absolute fluorescence yield, which currently is the dominating source of systematic uncertainty (14 % [33, 132]). Further systematic uncertainties of the absolute energy scale are related to the absolute detector calibration (9.5 % [133]) and its wavelength dependence (3 %). The lateral distribution of Cherenkov light, which is neglected in Eq. (3.2.15) can be modeled and leads to a 5 % increase of the reconstructed energy [134]. Correcting the finite spot size of the optical systems and its halo created by dust on the mirrors and UV-filters leads to an additional $3 - 5\%$ increase. Both effects are currently being studied in detail and are not considered in this work. A small energy bias of about 3 % has been observed in the reconstruction of MC simulated events. It is related to the uncertainty in the constrains of the Gaisser-Hillas parameters Λ and X_0 (cf. Fig 3.2.17). The correction for the invisible energy is known to 4 %. Atmospheric effects like the temperature and humidity dependence of the fluorescence yield are currently estimated to yield a combined altitude dependence of about 10 %. The uncertainties of the

aerosol content of the atmosphere contributes 5 % [122]. The total systematic uncertainty of the energy determination can be estimated as 23 % [67, 135]. A detailed summary is given in Table 3.2.5.

Table 3.2.1: Contributions to the systematics uncertainty of the energy scale of the Pierre Auger Observatory.

Source	$\Delta E_{FD}/E_{FD}[\%]$
Absolute Fluorescence Yield	14
Altitude dependence of Fluo. Yield	10
Pressure dependence of Fluo. Spectrum	1
FD absolute calibration	9.5
FD wavelength dependence response	3
Rayleigh atmosphere	1
Wavelength dependence of aerosol scattering	1
Aerosol phase function	1
spot size and Cherenkov LDF	10
Invisible energy	4
Gaisser-Hillas parameters	3
TOTAL SYST.	23

Most of the items contributing to the systematic uncertainty are affecting the amount of light emitted by EAS and the visibility for a given energy with the detector. For example a higher fluorescence yield would result in more photons emitted at the shower, which could be detected from farther away. The available exposure would therefore increase. These effects have been studied extensively and will be discussed in Sec. 7.2.1.

Chapter 4

The uptime of the Pierre Auger Observatory

The efficiency of fluorescence and hybrid data taking is influenced by many effects. These can be external, e.g. lightning storms, or internal, i.e. caused by the data taking itself, e.g. data acquisition (DAQ) failures. In order to be able to determine the UPTIME of our hybrid detector it is therefore crucial to take these possibilities into account and derive a solid description of the (time dependent) data taking quality.

Failures and outages can occur on different levels. Starting from the smallest unit of the FD, i.e. one single pixel readout channel, up to the highest level, i.e. the combined SD-FD-data taking of the Observatory. The desired accuracy of the exposure determination ($\mathcal{O}(\%)$) can only be achieved if disturbances at all levels are taken into account. As illustrated in Fig. 4.0.1, the UPTIME of the hybrid detection mode of the Pierre Auger Observatory is derived from a variety of monitoring information and the cosmic ray data itself. As compromise between accuracy and stability the complete detector status down to the single photomultiplier is given for time intervals of 10 min.

4.1 Uptime determination

4.1.1 Pixel uptime

Possible failures at the photomultiplier or *pixel* level are related either to broken photomultipliers or to failures in the front-end-electronics for example related to the high voltage supply. Usually these failures appear only for a limited time ($\mathcal{O}(days)$) as they are detected during the nightly relative FD-calibration runs and fixed in a short timescale by the staff of the observatory. Based on algorithms implemented directly in the front-end electronics boards, a detailed description of the current status of each fluorescence telescope is available. These algorithms, called *BGLoop*, provide the ADC-variance, baseline, FLT-trigger threshold and trigger-frequency for each pixel every 30s and enable therefore a very accurate determination of the status of all pixels. The ADC-variances, baselines and trigger threshold will also be used in the MC simulations to obtain a realistic description of the FD-trigger response,
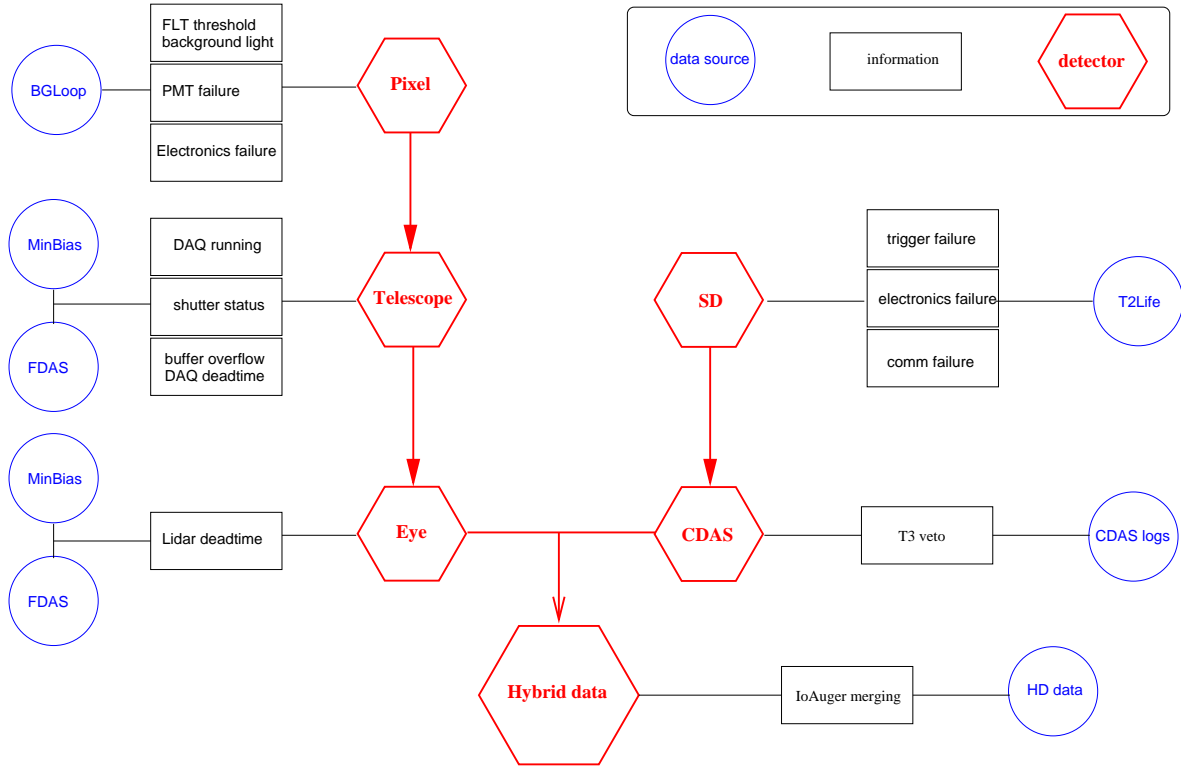
Figure 4.0.1: The determination of the detector status description is based on a variety of data sources (circles). They provide detailed information (squares) on different components of the detector (hexagons).

which is influenced by changing night sky background light, etc. (cf. Sec. 5.1.3).

To obtain the status information of the photomultiplier and the connected readout channel, the full BGLoop information is processed and checked for consistency, i.e. all entries have to yield reasonable values. The trigger-frequency for example is auto-adjusting itself to about 100 Hz and values above 1 kHz are considered to be unphysical and the pixel is discarded from further analysis. This adjustment algorithm is changing the trigger threshold with respect to the baseline and the variance of the ADC signal. Pixels with thresholds below the baseline are, for example, also regarded as problematic and switched off.

The output of this analysis is a description of the status of all 10560 photomultipliers active in the fluorescence detector of the Pierre Auger Observatory in 10 min intervals. It contains the pixel status δ_{pix}, i.e. ON or OFF, as well as the noise-level and the FLT-trigger threshold.

4.1.2 Telescopes uptime

The main contribution to the hybrid-deadtime is related to the moon cycle and the corresponding data taking periods. Data taking is currently limited to a moon-fraction smaller than 60 % leading to 16 nights of data taking per moon cycle. In addition, even during the actual shift period, data taking is not 100% efficient as multitude of problems may arise during the operation of the highly sophisticated fluorescence detector. For example the DAQ-

(a) background noise (b) electronic noise

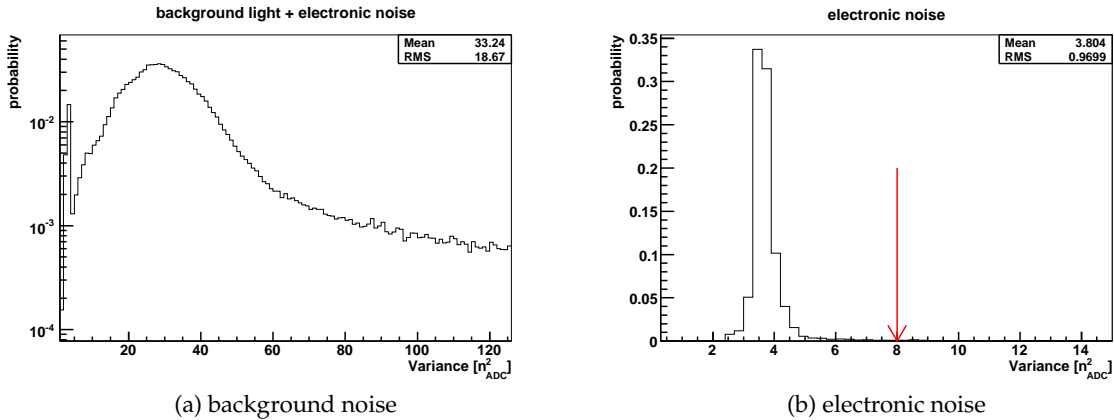Figure 4.1.2: Background variances as recorded in the BGLoop data files. The main contribution to this background noise is the ambient night-sky background light coming from stars and the direct and scattered moonlight (left panel). The peak at low variances is related to time periods with closed telescope shutters. A dedicated analysis confirms that the readout electronics is causing a variance of around $4\,n_{\rm ADC}^2$ (right panel).

software itself, the wireless communication between the detector building and the central control room might fail or power outages might cause a shutdown of parts of the system.

To determine the actual running time of the FD-DAQ we rely on a minimum bias datastream with high event-rate. A fraction of the events which are rejected by the TLT or T3 algorithms are written to a dedicated datastream. As shown in Fig. 4.1.3a, about $5-10$ of these *MinBias* events are recorded per telescope and 10 min, compared to only one or two events for the standard datastream (FDAS). If no MinBias data is available due for example to network or filesystem problems, the FDAS data is used as fall-back solution. This happens in less than 4 % of the time periods and should therefore not influence the accuracy of the status determination. The broad distribution of the number of MinBias events is related to changes in the FD-DAQ to reduce the file size and the modifications of the TLT algorithm discussed in Sec. 5.1.3. Files are written for each *run*, i.e. one datafile is created for each DAQ start-stop period. With the whole data taking becoming more and more stable over the last years, these runs cover longer time periods (usually one night) and the MinBias event rate had to be reduced to stay below the operating system file size limits. These changes are reflected in Fig. 4.1.3b.

If the DAQ is running and one or more events are detected in the given time interval and telescope the corresponding telescope-status $\delta_{\rm tel}$ is set to 1.

Even if the DAQ is running the shutters of the telescope might be closed. Shutter closing is triggered by alarms from the slow control system observing for example the windspeed and rainfall. Another failsafe mechanism has been implemented in 2007 to protect the photomultipliers from to high background light and shutters are automatically closed if the average variance exceeds the threshold of $\langle Var \rangle_{\rm cut} = 100\,n_{\rm ADC}^2$. With closed shutters obviously no cosmic ray data can be collected but muons hitting the camera might lead to noise triggers and spoil the uptime information. The shutter status is not directly available for analysis and indirect methods relying on the background noise fluctuations (variance) from the BGLoop-algorithms have to be applied. As reference, the noise related to the read-
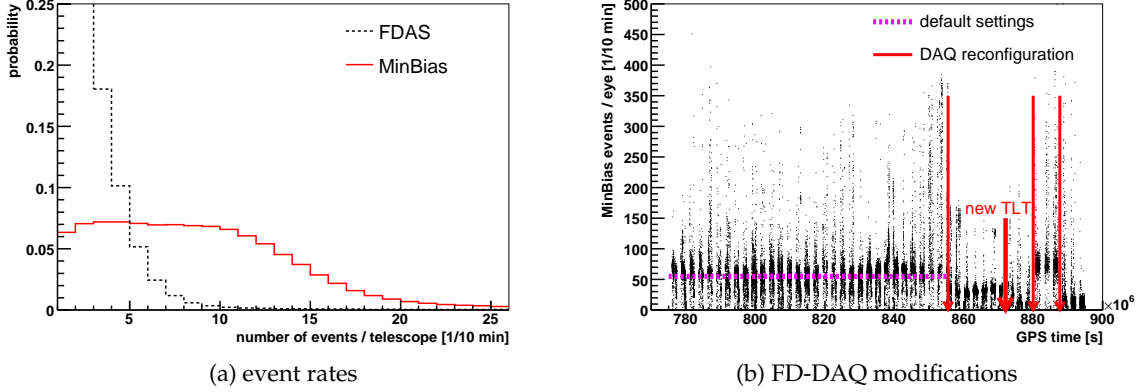
(a) event rates

(b) FD-DAQ modifications

Figure 4.1.3: The *MinBias* data stream is providing detailed information about the status of single telescopes due to its high event rate (left panel). The MinBias event rate is influenced by modification of the TLT trigger algorithm and changes of the DAQ settings (right panel).

out electronics itself could be determined. Each night of data taking relative calibration runs are performed to follow the evolution of the absolute calibration of the system. These measurements are performed with closed shutters and the BGLoop data recorded during these special runs have been used to derive the electronics noise distribution. The mean electronics variance is found to be $\langle Var \rangle \approx 4\,n_{\text{ADC}}^2$ (cf. Fig. 4.1.2b). As the night sky background noise is causing the variance to rise significantly above this level (cf. Fig. 4.1.2a) the probability $\varepsilon_{\text{shutter}}$ of the shutters being open can be derived for each time interval as

$$\varepsilon_{\text{shutter}} = \frac{\#\text{open}}{\#\text{total}}, \tag{4.1.1}$$

where #open denotes the number of BGLoop-entries for the given telescope with mean variance over the whole camera being larger than $8\,n_{\text{ADC}}^2$ (arrow in Fig. 4.1.2b). #total is the total number of BGLoop-entries in the given time interval. If no BGLoop data is available no decision is possible and the telescope status δ_{tel} is set to OFF.

The requirement to have at least one MinBias or FDAS-event per time interval is also eliminating another hardware related problem, which appeared during a limited time in 2005 and 2006. It caused undetected interruptions of the firewire communication between the computer running the DAQ of the single telescopes (MirrorPC) and the main PC collecting the information from different telescopes in the building (EyePC). The final stage of the trigger scheme, the T3 algorithm is running on the EyePC and the event is only stored after passing this condition. A disconnection between MirrorPC and EyePC results therefore in a complete data loss from the concerned telescope without a stop of the DAQ and without interrupting the other monitoring datastreams.

The readout speed and buffer size of the DAQ-system is limited. High event rates might cause the buffers to overflow and lead to an event loss (deadtime). The accumulated deadtime is stored in an event-by-event way in the output format of the fluorescence DAQ and has to be converted into the deadtime during each 10 min time interval denoted $T_{\text{DAQ}}^{\text{dead}}$. This conversion is performed using the MinBias files due to the higher rate, or, if not available, the FD-data. This intrinsic telescope deadtime is then translated into the telescope upfrac-

tion $\varepsilon_{\mathrm{DAQ}}$, which can be interpreted as the probability of the given telescope to be taking cosmic ray data or life-time fraction

$$\varepsilon_{\mathrm{DAQ}} = 1 - \frac{T_{\mathrm{DAQ}}^{\mathrm{dead}}}{T_{\mathrm{DAQ}}} \ . \tag{4.1.2}$$

Here, T_{DAQ} is the total running time of the DAQ in the given time interval.

4.1.3 Eye uptime

Most of the possible hardware or data taking problems at the eye level are rather easy to detect. The by far most abundant are power failures at certain detector stations or over the full array and losses of the wireless connection to the central control room. During these periods no events are recorded in the given building and the system is considered as OFF in the UPTIME.

Currently two additional disturbances are known to affect the data taking at the eye level: veto algorithms rejecting periods with Lidar activity and algorithms rejecting FD-T3 based array readout requests in order to protect the central data taking system (CDAS) from too high event rates.

The Lidar-veto is set by the Lidar atmospheric monitoring system before performing laser shots in the field of view of the fluorescence detector. It disables the FD-DAQ for a certain amount of time depending on the frequency of the Lidar shots. The related deadtime is very small. The veto is acting on a single eye only and the Lidar-system is receiving T3 information from the FD in order to perform dedicated scans in the direction of interesting events. In this configuration, which was changed only at the end of 2007 it might happen that one eye is detecting Lidar scans from another eye. These triggers are then activating the local Lidar system to perform another scan. These Lidar cross-triggers increased the veto-time significantly. The cumulative Lidar veto deadtime is stored on an event-by-event basis in the MinBias or FDAS files. During the determination of the uptime it is taken into account by transforming the deadtime $T_{\mathrm{Lidar}}^{\mathrm{dead}}$ into an eye efficiency $\varepsilon_{\mathrm{Lidar}}$

$$\varepsilon_{\mathrm{Lidar}} = 1 - \frac{T_{\mathrm{Lidar}}^{\mathrm{dead}}}{T_{\mathrm{DAQ}}} \ . \tag{4.1.3}$$

$\varepsilon_{\mathrm{Lidar}}$ can be interpreted as the probability for a cosmic ray event to fall outside the Lidar vetoed period.

To have a high trigger efficiency of hybrid events with energies below the SD trigger threshold of $10^{18.5}$ eV, all FD T3-triggers are sent to CDAS and the surface array is read out. The FD and SD datastreams are later merged to form *hybrid events*. Lightning and other noise events can cause high FD-trigger rates, which would cause significant deadtimes for the surface array due to the finite readout time of the array. To prevent this possible loss of surface detector events, protection veto algorithm are running on both FD and CDAS side. These T3-VETOES are discarding events with a given probability depending on the current FD-trigger rate. Independent information is only available for the CDAS veto algorithms. After the installation of the algorithms end of 2005, every vetoed event is listed in the CDAS

(a) CDAS T3 efficiency vs. time   (b) average CDAS T3 efficiency
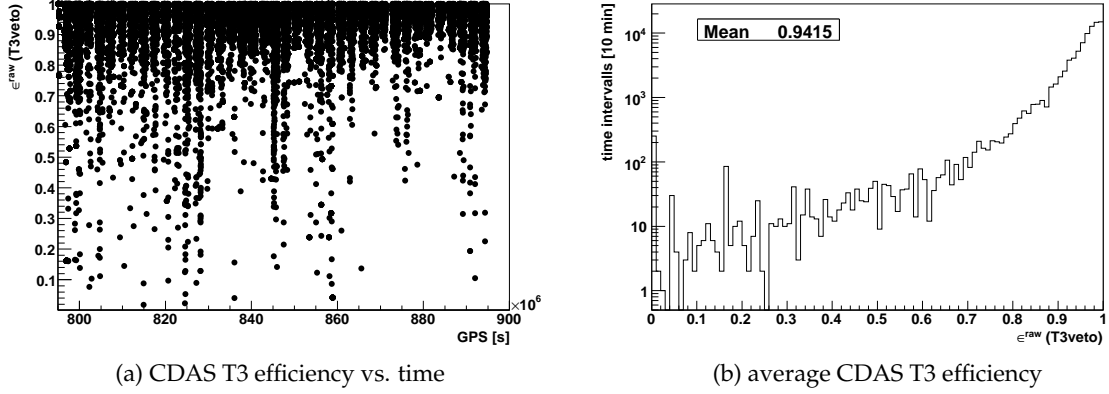
Figure 4.1.4: Veto algorithms are used to protect CDAS from high FD trigger rates, which are very time dependent (left panel) and introduce a significant deadtime for low energy hybrid events (right panel).

logfiles. The efficiency to have a T3 passing the veto algorithms and being sent to the array is given by the fraction of accumulated veto-time ΔT_{veto} over the full time period $T = 10\,\text{min}$:

$$\varepsilon^{\text{raw}}_{\text{T3veto}}(e) = 1 - \frac{\Delta T_{\text{veto}}}{T} \ . \tag{4.1.4}$$

In Fig. 4.1.4 the strong time dependence and the large spread of the deadtime introduced by the veto algorithms, which is reflecting the time dependence of the high trigger rate periods, is illustrated. Most of the events in these periods are related to lightning and background light activity, which usually occur only for a limited time. Averaging over time, about 14 % of all FD-triggers reaching CDAS are not sent to the surface array. The data taking time on the other hand is reduced only by about 6 %, reflecting the time correlation of the lightning bursts (cf. Fig. 4.1.4b).

The raw event loss probability is only valid if a vetoed event is not recovered by an independent SD-trigger. During the off-line merging process between SD and FD events, also previously vetoed events can be merged with their SD counterpart if the air shower was able to trigger the surface detector. This recovery process is energy dependent. The relevant trigger on the SD side is the 3ToT condition $\varepsilon_{3\text{ToT}}$. Its energy dependence has been estimated with the help of air shower simulations (cf. Fig. 4.1.5a and [98]). This energy dependence cannot be taken into account during the calculation of the uptime as the energy distribution of events is depending on the applied quality selection criteria of the analysis. It is therefore not possible to derive the REAL T3-veto event loss probability in a given time interval a priori and only the raw T3-veto efficiency (cf. Eq.(4.1.4)) is stored. The recovering of the lost events can to be taken into account at the last stage of the MC-simulation process on an event by event basis and using the known energy of each simulated air shower, or, based on event by event information in the CDAS-logfiles, all recovered events can be removed. A comparison of both methods will be discussed in Sec. 6.1.

For illustration purposes, an average T3-veto correction factor $< k_{\text{T3veto}} >$ can be derived

(a) 3ToT probability
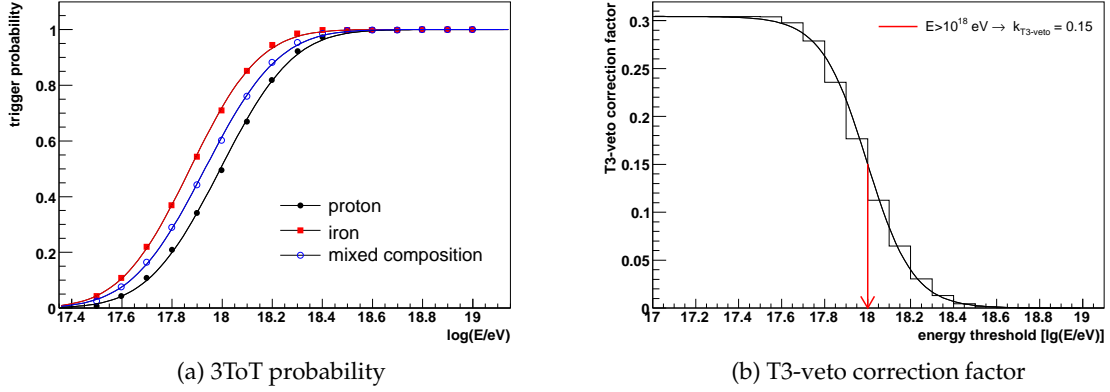

(b) T3-veto correction factor

Figure 4.1.5: The event loss due to the CDAS-protection veto is partly recovered by the SD trigger. The correction factor to be applied to the raw T3-veto loss is therefore depending on the energy threshold of the data sample.

as

$$\langle k_{\text{T3veto}}(E_{\text{thr}}) \rangle = \langle 1 - \varepsilon_{\text{3ToT}}(E) \rangle \tag{4.1.5}$$

$$= \frac{\sum\limits_{E_i > E_{\text{thr}}}^{\infty} 1 - \varepsilon_{\text{3ToT}}(E_i)}{\sum\limits_{E_i > E_{\text{thr}}}^{\infty} 1} \, . \tag{4.1.6}$$

The averaging process takes into account the actual energy distribution of selected events above a given energy threshold E_{thr}. For example, based on the event selection applied for this work (cf. Sec. 6.2) and a threshold of $E_{\text{thr}} = 10^{18}$ eV one obtains $< k_{\text{T3veto}} > = 0.15$. That means that about 85 % of the vetoed events will be recovered by the SD trigger and the IoAuger merging procedure. In figure 4.1.5b, the dependence of the correction factor on the threshold energy is shown. As expected, the event loss due to the T3-CDAS-protection veto algorithms is becoming smaller when using only events closer to the SD-trigger threshold, i.e. having higher energy. Following Eq. (4.1.4), the hybrid detection efficiency in periods with active T3-veto can be written as

$$\langle \varepsilon_{\text{T3veto}} \rangle = 1 - f_{\text{T3veto}}^{\text{raw}} \cdot \langle k_{\text{T3veto}} \rangle \, . \tag{4.1.7}$$

4.1.4 CDAS uptime

To estimate the hybrid uptime of the Pierre Auger Observatory also changes in the surface array configuration and CDAS inefficiencies come into play. During the time period analyzed here, the array grew from about 600 to 1550 stations. This increase is directly influencing the available fiducial volume of hybrid observations as the core position of the showers taken into account in this analysis have to lie inside the active surface array. Changes in the array configuration can happen on very different time scales and magnitudes. Power outages can cause communication losses with sometimes large areas of the array, single stations might show hardware failures, etc.
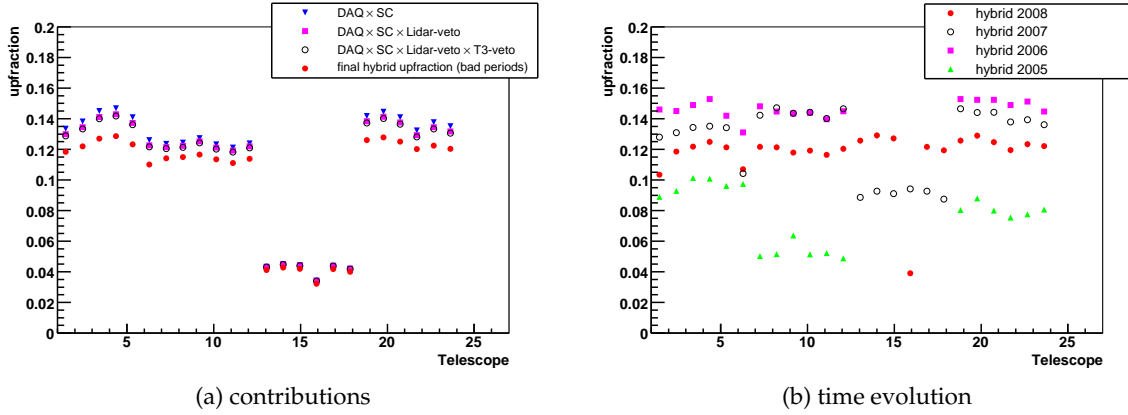
(a) contributions

(b) time evolution

Figure 4.2.6: Main contributions to the hybrid uptime and the evolution of the average hybrid duty-cycle with time.

Similar to the BGLoop algorithm running on the FD side, the surface detector array is constantly monitored and a very detailed description of the array status with a time resolution of 1 second is available. This *T2Life* information allows the perfect description of the surface array status during data taking periods without major problems.

In addition to the usually very localized problems of single tanks, problems on larger scales like the trigger system itself can cause event losses. At the same time the T2Life information becomes inaccurate. Time periods with these problems, i.e. *bad periods*, are detected by a dedicated working group inside the Auger collaboration. They are excluded in the hybrid uptime. Another minor effect is related to a problem with the leap second, which was introduced at the beginning of 2006. Due to a mis-configuration, no hybrid events were detected until January 23rd 2006. This period is therefore removed from the hybrid detection uptime. An additional check for possibly undetected problems like this is requiring at least one hybrid event per 10 min time interval. This requirement is also removing periods in which the merging between FDAS and CDAS files into the final IoAuger hybrid files failed and assures a valid hybrid data taking condition.

4.2   Results and cross-checks

The probability $p(i,t)$ of a given telescope i belonging to eye e to be operational in a given time interval t can then be finally written as

$$
\begin{aligned}
p(i,t) \;=\; & \varepsilon_{\text{shutter}}(i,t) \cdot \varepsilon_{\text{DAQ}}(i,t) \cdot \delta(i,t) \\
& \cdot \varepsilon_{\text{Lidar}}(e,t) \cdot <\varepsilon_{\text{T3veto}}(e,t)> \\
& \cdot \delta_{\text{CDAS}}(t)
\end{aligned}
\tag{4.2.8}
$$

$\delta = [0,1]$ denotes the status flags of the different systems. The time evolution of the full hybrid duty-cycle over $3^{1}/_{2}$ years during the construction phase of the observatory is shown in Fig. 4.2.6b. It should be noted that the telescopes belonging to the building of Los Morados (telescopes 7-12) have become operational only in May 2005 and the ones in the Loma
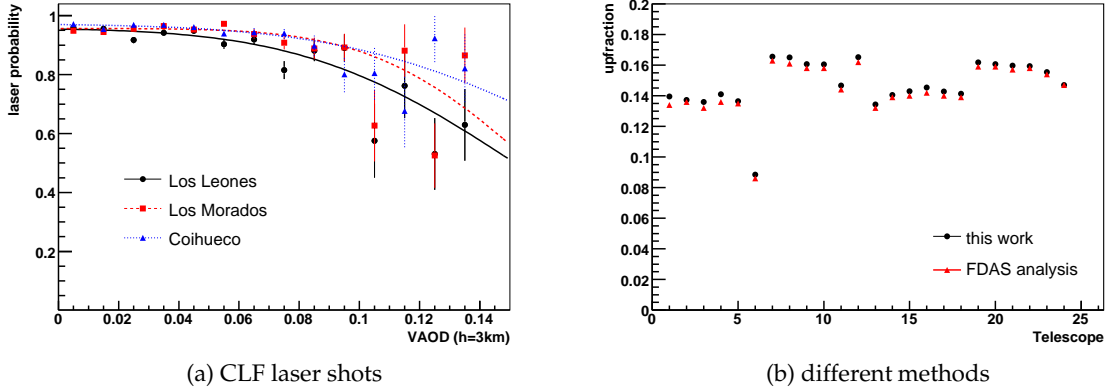
(a) CLF laser shots   (b) different methods

Figure 4.2.7: Cross-checks of the derived uptime using CLF laser shots (left panel, [138]) and FDAS files (right panel, data from [139]).

Amarilla building (telescopes 13-18) have become online in March 2007. In 2008 data taking in telescope 16 was reduced significantly due to hardware failures of the trigger electronics. The reduction of the data taking time in 2007 is related to the automatic closing of the shutters during periods with high background noise contamination (variance $> 100\,\mathrm{n}^2_{\mathrm{ADC}}$) which has been discussed in Sec. 3.2.

The main contributions to the data taking deadtime are shown in figure 4.2.6a. SC stands for *slow control* and denotes, for example, the status of the shutters. An average T3-veto efficiency of $k_{\mathrm{T3veto}} = 0.15$ (cf. Eq. (4.1.7) and Fig. 4.1.5b) has been applied to the time and eye dependent raw T3-veto (cf. Sec. 4.1.3).

The achieved average hybrid data taking efficiency of about 12 % is exceeding the expectations (≈ 10 %, [136]). Still, significant improvements can be expected in the future, especially as soon as the Internet connection to Malargüe is enhanced and stabilized. A project to provide a faster network connection to Malargüe, which would enable and facilitate remote monitoring of the observatory is funded by the European Commission [137].

Validation of the derived uptime is possible, for example, with the help of CLF laser shots. As laser shots can be observed from all four eyes, the probability of recording the laser signal in a particular eye i can be calculated as P(laser in eye$_i$ given at least one laser in any other eye). The expected number of laser shots in eye i can be derived from the uptime of the telescope pointing to the CLF, $p(i)$. The probability to observe a laser shot is naturally depending on the light transmissivity of the atmosphere. Taking into account only scattering on aerosols, the atmospheric quality can be related to the 'vertical optical depth' (VAOD). The dependence of the laser observation probability P on this parameter is shown in Fig. 4.2.7a. More important for the validation of the uptime is the fact that for presumably clear periods, i.e. VAOD ≈ 0, the uptime weighted probability is in agreement with 1 within 4 %. The systematic uncertainty on the overall uptime accuracy can therefore be estimated to be as low as 4 %.

This estimate is also confirmed by an independent uptime determination within the Pierre Auger Collaboration [139]. The analysis is following the approach discussed here, but is relying only on FDAS and BGLoop data to derive an average upfraction at the tele-
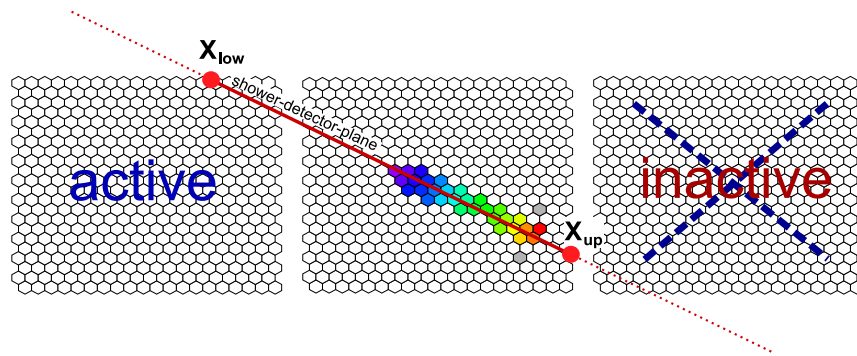
Figure 4.3.8: An accurate calculation of the field of view boundaries is needed for mass composition studies relying on the observation of the shower maximum. The derived telescope duty-cycle is increasing the reliability of these calculations (eg. [55], plot from [13]).
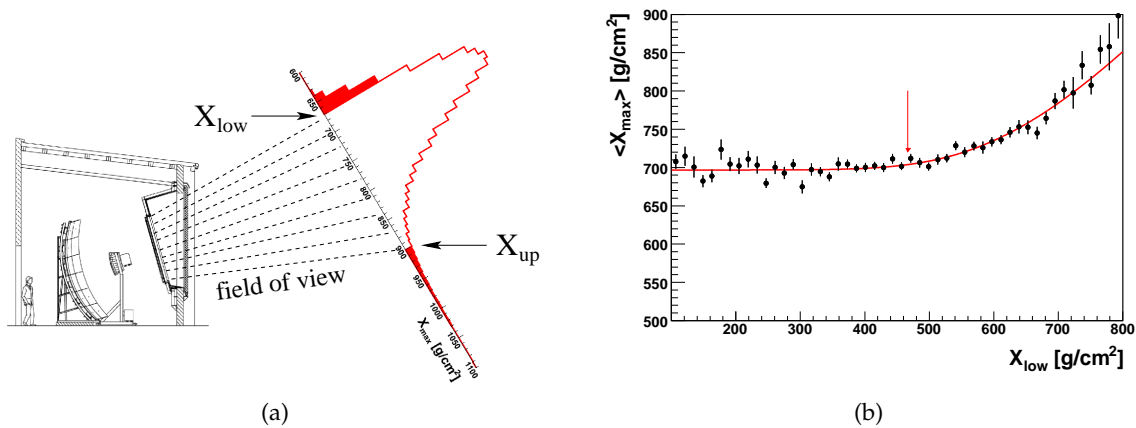
Figure 4.3.9: Illustration of the effect of the field of view of the fluorescence detector on the selected X_{max} distribution (left panel). Fiducial volume cuts have been derived to assure an unbiased X_{max} distribution (right panel) [55, 141].

scope level for each data taking run. The agreement with the life time data derived for this work is better than 2 %. The remaining difference can be attributed to the lower statistics of the FDAS data compared to the MinBias data stream. Additional work on deriving an uptime using a recently introduced performance monitoring system [140] has started.

4.3   Applications

The field of view (FOV) of the fluorescence detectors is limiting the available slant depth observation range depending on the shower geometry. The typical event selection criteria require to have the shower maximum inside the field of view of the detector in order to be able to reconstruct the energy and the position of the shower maximum X_{max} accurately. This condition is biasing the observable X_{max} distribution and consequently the mass

composition sensitivity (cf. Fig. 4.3.9a). In order to achieve equal sensitivity of all possible primary masses, dedicated event selection criteria have been developed in the context of elongation rate studies [55, 141]. Based on the reconstructed air shower geometry, the possible observation range in slant depth is calculated and energy dependent limits on this range are ensuring an unbiased X_{max} measurements. These limits have been derived from reconstructed hybrid data itself. An example of the X_{max} dependence on the lower field of view boundary and the derived selection criteria is shown in Fig. 4.3.9b. It has been realized that, for a precise determination of the observation range, the information on the status of telescopes neighboring the triggered one(s) has to be used too (cf. Fig. 4.3.8). This status information is provided by the uptime information discussed above.

In addition to the initial use for studies of the primary mass composition, the FOV boundary determination is also essential for other studies relying on the measured X_{max} distribution like the determination of the proton-air cross-section [13].

Chapter 5

Time dependent Monte Carlo simulations

Monte Carlo (MC) simulations are a widely used tool in all areas of physical research. Particularly in particle physics they are of special importance as a correct model of the complex detectors is extremely important to prepare analysis, understand the data, etc. Usually the MC detector models are ideal detectors and have to be tuned to reproduce the real world as much as possible. This is especially important for experiments like the Pierre Auger Observatory were the Earth's atmosphere is an important part of the detector. Environmental parameters change on relatively short timescales and alter the data taking conditions significantly. In addition the hardware configuration of the detector setup changed with time as the observatory was in its building phase during the data period analyzed here. It has, therefore, been realized that a static description of the detector setup is not sufficient for a precise determination of the detector properties and especially for an exposure determination. To reproduce the data taking conditions of the experiment as precise as possible, a time dependent detector Monte Carlo approach, called REALMC , has been developed.

The basis of the REALMC scheme is a time dependent detector description, which includes basic parameters like the trigger threshold of each pixel and the background noise contamination (Sec. 5.1.3). The different trigger algorithms of the fluorescence detector are applied to simulated events in the same way as done during data taking. Major changes in the trigger configuration are taken into account. Their influence is discussed in Sec. 5.1.3. The response of the surface detector is modeled and the events are reconstructed using the same algorithms as applied to data. The full MC chain is validated by comparisons with data and basic parameters of the detector like its resolution are derived in Sec. 5.2.

5.1   Air shower and detector simulation

In addition to an accurate detector description, reliable air shower simulations are required to model the response of the observatory and derive the exposure. Different program packages have been developed over the last years to provide this information. All of these air shower simulation packages are relying on hadronic interaction models like SIBYLL [142]

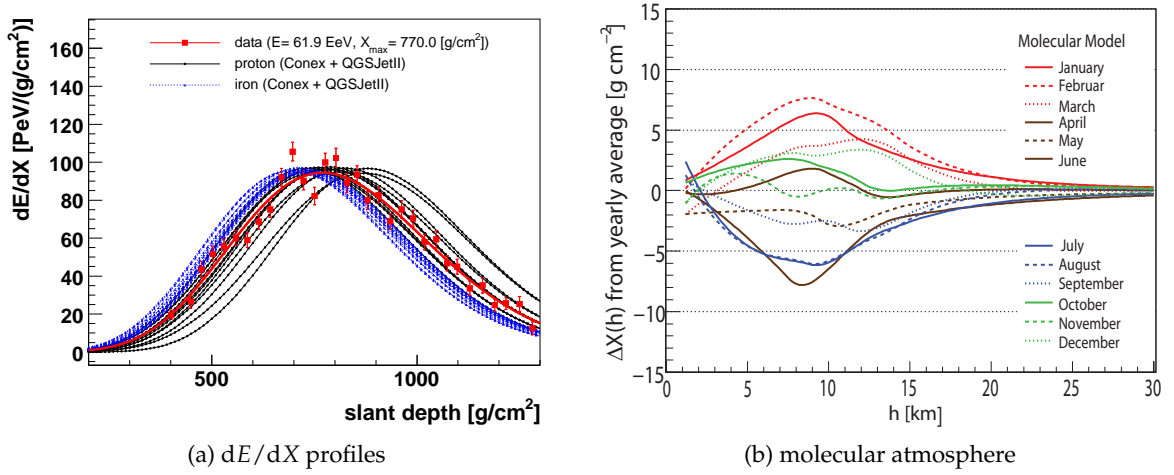(a) dE/dX profiles   (b) molecular atmosphere

Figure 5.1.1: Longitudinal energy deposit profiles simulated with CONEX [130] are the basis of the MC simulations. Comparison between a measured profile (big red markers) with proton (black solid lines) and iron (blue dotted lines) simulations show good qualitative agreement (left panel). Seasonal changes of the molecular atmosphere are parameterized in monthly models, which are used during data reconstruction as well as during REALMC simulations (right panel, from [146]).

or QGSJET-II [143], which extrapolate accelerator measurements at lower energies towards the regime of ultra-high energy cosmic rays interacting with nuclei in the atmosphere. The produced secondary particle cascade, which builds up the air shower is tracked within MC programs like CORSIKA [129] or AIRES [144] to provide a full 3D model of the air shower development. Due to the enormous computational requirements these tools are not suited to achieve the large statistics needed to scan the whole parameter space of primary energy and mass composition needed for this work.

As the fluorescence technique is relying on measurements of the bulk of secondary electromagnetic particles in the EAS, the information about individual particles is not necessary for reliable simulations. Its is sufficient to simulate the development of the electromagnetic and muonic component along the incoming direction of the primary particle. Particles with transverse momentum can be projected back onto this shower axis. In order to further increase the speed of the calculations, *hybrid* event generators like CONEX [130] or SENECA [145] switch after the simulation of the first few ultra-high energetic interactions to numerical solutions of the underlying cascade equations, which govern the evolution of the different shower components. Although the simulations are extremely fast (about 1min CPU time per shower) all important features observed in full MC simulations like average shower variables but also shower to shower fluctuations are reproduced extremely well [130, 131]. Due to the high speed of the calculations the process of *thinning*, during which particles are removed from the simulations and weights are assigned to the remaining ones, is not needed and artificial fluctuations in the shower parameters are reduced.

The most important output of CONEX for this work is the longitudinal profile of the energy deposited by the secondary air shower particles in the atmosphere as shown in Fig. 5.1.1a. This dE/dX profile is the basis for the simulation of the fluorescence light emission. In addition the shower size profile (number of e^+e^-) is needed to calculate the

Cherenkov light emission. As illustrated in Fig. 5.1.1a, the longitudinal development predicted by CONEX agrees qualitatively well with that of a measured air shower. The largest uncertainty is due to the unknown primary mass composition. Using the QGSJETII interaction model and two extreme assumptions for the primary mass, proton and iron, with the same energy as a recorded EAS, one can find a good overall agreement of the profile shape. More detailed comparisons between large samples of measured profiles and simulations confirm this agreement (e.g. [147, 148]). Due to the a priori unknown primary mass composition simulations have to be performed on the full parameter space of primary energy and mass. For this work equal fractions of proton and iron induced air showers have been simulated.

Other systematic uncertainties may arise from the use of different interaction models to describe the hadronic interactions of the primary and secondary particles. The model difference for the predicted longitudinal shower development is reflected in the different $\langle X_{\max} \rangle$ predictions shown in Fig. 2.2.7. The models differ also in the invisible energy correction factor. This factor, which takes into account the energy transfered to high energetic muons and neutrinos, has to be applied to the energy measured with a fluorescence detector. As this fraction of energy is not visible with the fluorescence detector it might change the predicted distance up to which EAS are detectable. This effect is studied in detail in Sec. 6.3. SIBYLL and QGSJETII simulations have been performed to equal parts.

The energy range accessible with hybrid measurements is spanning more than three decades from below 10^{18} eV to above 10^{20} eV. The MC simulations have to cover the full range without loosing statistical power in the relevant region. Therefore, simulations were performed above 10^{17} eV in steps of one decade. Within each decade about 10^6 showers of each primary were simulated following a flat spectrum in $\lg(E)$. The showers from this library are covering a large zenith angle range up to $\theta = 75°$ and are re-sampled in different geometries across the detector according to

$$\frac{\mathrm{d}N}{\mathrm{d}\cos\theta} \propto \cos\theta \, , \tag{5.1.1}$$

where $\cos\theta$ accounts for the projection of the surface detector area.

5.1.1 Light emission and propagation through the atmosphere

The raw air shower signatures from CONEX are passed to the detector simulation software of the Pierre Auger Observatory, the $\overline{\text{Off}}\underline{\text{line}}$ analysis framework [108]. The simulation package is based on earlier works [149] but has been updated in almost all aspects since then [150]. The REALMC approach has been implemented based on these default packages, which are using a static detector description. In order to introduce the time variability of the detector setup, a crucial step is the assignment of an individual timestamp to each simulated event. Timestamps are distributed randomly in the time interval covered by the simulations and should scan it as precise as possible. With the given timestamp, the detector description including the atmospheric parameters is now easily accessible within the framework via high-level user interfaces to expert databases containing the full set of information (cf. Fig. 3.2.9).

(a) light propagation
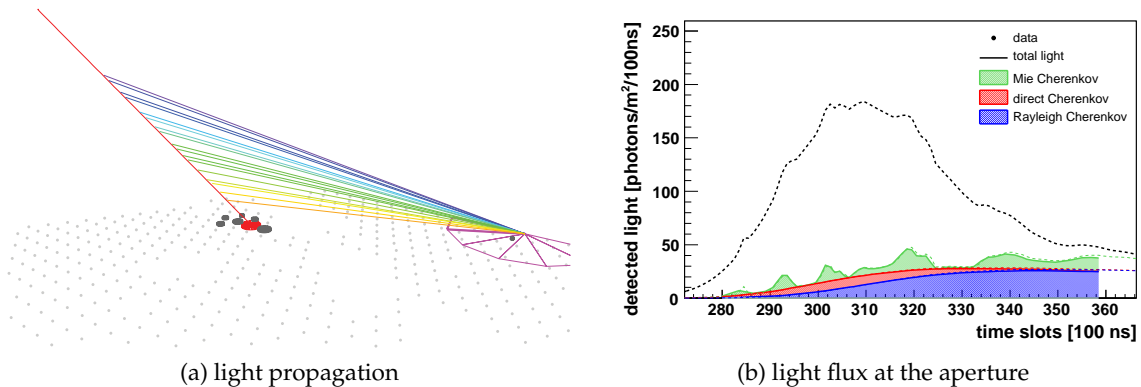

(b) light flux at the aperture

Figure 5.1.2: The emitted light at the shower axis is propagated towards the detector taking into account all measured atmospheric parameters (left panel). The resulting light flux received at the aperture of the telescopes shows very realistic features (right panel).

Important quantities are, for example, the atmospheric conditions at the given time. Balloon based radio-sonde measurement at the site of the experiment in conjuction with measurements at the local airports of Santa Rosa, Cordoba and Mendoza, have been used to derive average models for the pressure and temperature profiles of the atmosphere above the observatory. The differences between these models are shown in Fig. 5.1.1b. They are reflecting mainly seasonal variations. The influence on the energy reconstruction has been studied and found to be about 1 % [151]. The analysis of more radio sonde measurements will in the near future allow for an increased reliability of the monthly models and more detailed studies of the related systematic uncertainties. The molecular atmospheric profiles are needed to convert the longitudinal air shower profiles given as function of slant depth into profiles as function of height above the detector. They are also needed as input for the light emission processes itself. The fluorescence yield is depending on the atmospheric pressure and temperature [33], which are provided by the monthly models. The Cherenkov light emission threshold on the other hand is depending on the local index of refraction, which in turn is a function of pressure and temperature. Finally the density of the atmosphere is responsible for Rayleigh scattering. Although the transmission coefficients can be calculated analytically, a precise knowledge of the atmospheric profile is necessary and provided by the monthly models.

The aerosol content of the atmosphere changes rather rapidly with time and can therefore not be parameterized. One of the important aims of the atmospheric monitoring task of the Pierre Auger Observatory is the determination of the light attenuation and scattering on aerosols. The necessary measurements are performed with different laser beams and the resulting attenuation and scattering coefficients are written to $\overline{\text{Off}}\underline{\text{line}}$ databases. The parameters in that databases are usually valid for one hour and are used for the event simulation. An example for the resulting realistic structures due to Mie scattering in the simulated light signal recorded at the aperture of the telescope system is shown in Fig. 5.1.2b.

The time dependent description of the atmosphere is used to simulate the amount of light emitted by the air shower based on the fluorescence spectrum and its pressure dependence

measured by the Airfly collaboration [33]. The absolute fluorescence yield is taken from Nagano et al. [31]. The temperature dependence of the collision cross sections and the influence of water vapor in the atmosphere [118] are neglected as more data and an improved theoretical description are needed for a reliable implementation. In addition to the fluorescence light, the Cherenkov beam is calculated and all light components are propagated towards the detector taking into account their wavelength spectra.

5.1.2 Fluorescence detector response

Additional $\overline{\text{Off}\underline{\text{line}}}$ tools, *managers*, have been implemented to access the status information from the uptime calculation at this point of the simulation process. The telescopes and eyes, which were active at the given simulated timestamp are determined. If active telescopes are present, the status of all 440 PMTs per telescope is checked and set according to the uptime analysis. A hit-or-miss approach relying on random numbers is used to take into account the derived data taking efficiencies.

The light arriving at the aperture of the telescopes, illustrated in Fig. 5.1.2b, is used as input of a detailed ray tracing algorithm, which has been cross-checked by a full Geant4 [152] simulation of the telescope system [150]. The response of the PMTs is simulated such that it reproduces dedicated measurements of the angular dependence of the photon detection efficiency well [150].

At this stage, the end-to-end pixel calibration constants are applied. It is important that during REALMC simulations the same calibration constants are used as in data reconstruction in order to reproduce the efficiency loss observed in certain FD cameras. As discussed in Sec. 3.2, this loss is compensated by introducing time dependent calibration 'constants'. A change in the sensitivity of the PMTs is directly related to a change in the trigger efficiency, which influences the available fiducial volume and the exposure. By applying the time dependent calibration values, this effect is taken into account in the REALMC simulations.

At this stage of the simulation procedure a possible mismatch between PMTs and their forseen readout channel is taken into account [153]. It has happened several times during the construction of the telescopes and during maintenance work, that PMTs and readout channels have been mis-cabled. This leads to a reduced trigger probability as the needed SLT pattern (cf. Fig. 3.2.5) might be disturbed, but also to a decreased reconstruction accuracy of detected showers. These problems are difficult to detect as shower images contain noise pixels and distorted camera pictures have to be found manually. The time periods with known mismatched readout channels are provided by an $\overline{\text{Off}\underline{\text{line}}}$ manager and taken into account.

The response of the readout electronics itself is well understood. The default simulation is relying on the detailed model given in Ref. [154] and a parameterization of variance induced by background light [155, 156]. In the REALMC approach, measured ADC variances and baselines obtained from the BGLoop data during the UPTIME determination are accessible directly from the implemented managers and fed into the electronics model to improve the agreement between simulated and the real hardware response. The uptime managers provide also access to the complete information needed for a reliable trigger simulation at the level of single PMTs.

(a) threshold stability
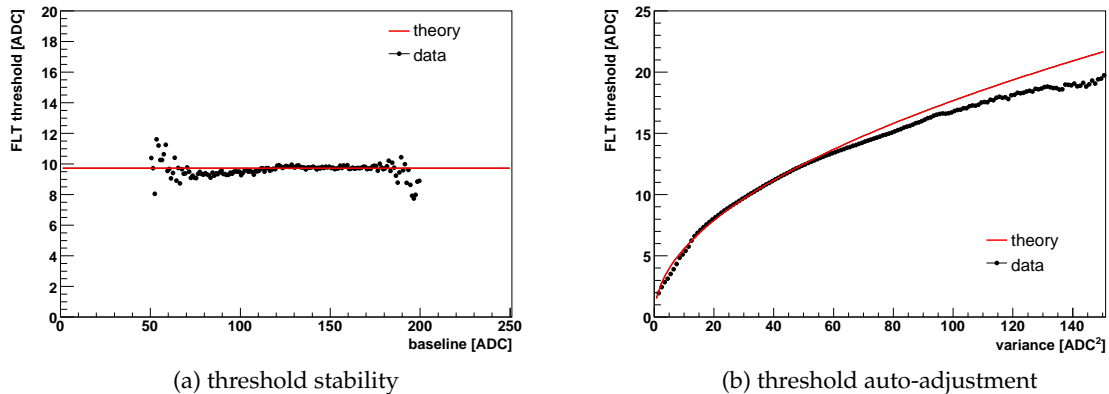
(b) threshold auto-adjustment

Figure 5.1.3: The auto-adjusting threshold of the First Level Trigger is independent of the underlying baseline (left panel) and follows the changing noise level within expectations (right panel).

5.1.3 FD trigger simulation

The different trigger levels of the fluorescence system of the Pierre Auger Observatory [100], have a common task, the rejection of noise events without rejecting air showers. Starting with a simple threshold trigger at the single pixel level the trigger layers become more and more complex and reach a preliminary event reconstruction at the last stage. For the determination of the exposure, the exact reproduction of all trigger levels is essential. Special focus is set here on the time dependence of the FLT due to changing background light conditions and on the TLT, which has been modified significantly recently. The other algorithms have not changed with time. During the MC simulations the code of the trigger algorithms is taken from the same library as during data taking.

First Level Trigger

The FLT-trigger is a simple threshold trigger running on the ADC trace of each pixel. The threshold is self-adjusting to the background noise level to yield an almost constant trigger rate of about 100 Hz per pixel. The adjustment should be independent of the underlying baseline of the ADC trace and proportional to the noise level, i.e. the square root of the signal variance. As shown in Fig. 5.1.3, both dependences are fulfilled to a reasonable degree. The deviation from the square root dependence of the trigger threshold is probably related to periods with fast increases of the variances (lightning bursts). The threshold adjustment is using a time average of the pixel trigger rate and is not able to follow these fast changes. The deviations from the ideal behavior are within the expected range and do not affect the data taking. On the other hand in order to estimate the exposure of the fluorescence detector from MC simulations, the trigger efficiency has to be modeled very accurately and these effects should be taken into account. The value of the trigger threshold is written to the BGLoop monitoring data and can be used to reproduce the trigger threshold even for data taking conditions in which the analytical assumptions are not valid. In the REALMC approach the recorded values of both the trigger threshold and the background variance are used to set the trigger conditions for each pixel independently, which is needed to take into account also

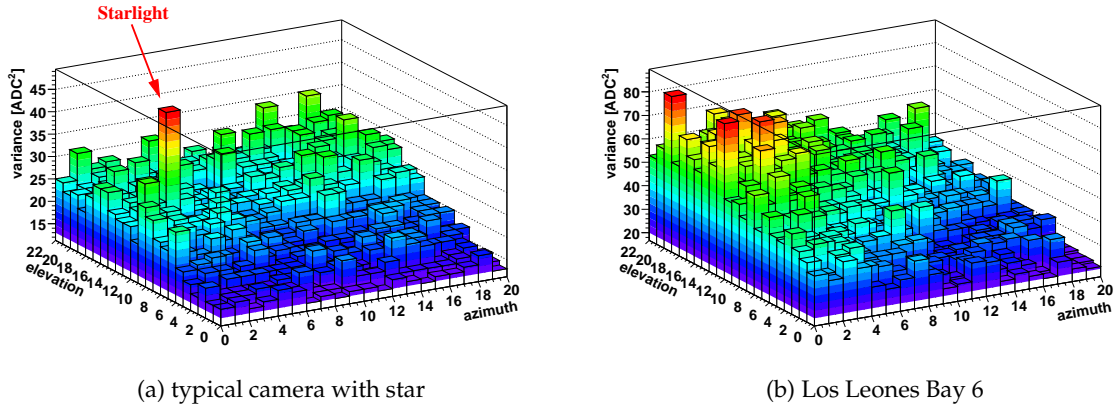(a) typical camera with star   (b) Los Leones Bay 6

Figure 5.1.4: Background variances in the FD camera as recorded in the BGLoop data. The ambient night-sky background light shows a strong elevation dependence (left panel). Single pixels show higher noise levels due to starlight. Telescope 6 in Los Leones is affected by light pollution from Malargüe (right panel).

time and directional dependences.

The main source of background noise is related to a phenomenon called air glow. Its main contribution is light produced by recombining ions in the upper parts of the atmosphere after photoionization by sunlight during the day. Due to the differences in atmospheric thickness and the related light absorption, the night sky background noise is increasing with elevation. As illustrated in Fig. 5.1.4a, this effect is clearly visible in the background noise recorded with the fluorescence detector. It is causing the camera to be less sensitive in the upper part and has to be taken into account. In addition, although the telescope shutters are closed if the moon is approaching the field of view closer than $5°$, scattered moonlight is causing higher background light already for larger distances and should be taken into account. Man-made light pollution can be neglected for almost all telescopes. Only one telescopes in the Los Leones eye is pointing towards the direction of the town Malargüe. Malargüe is about 13 km away from the eye and the additional light flux can clearly be seen in the background noise distribution shown in Fig. 5.1.4b. In addition to the lower uptime of this telescope with respect to other ones (cf. telescope 6 in Fig. 4.2.6b), the higher noise level and the accordingly higher trigger threshold of the telescope is contributing to the lower event rate recorded in the Los Leones station visible in Fig. 3.2.6.

In addition to these background light contributions affecting the whole camera, stars passing through the field of view are causing the variance to rise significantly for a very limited number of pixels and on relatively short time scales. As visible in Fig 5.1.4a, stars passing through the field of view of a pixel are altering the trigger conditions on $\mathcal{O}(\text{min})$ timescales.

This variability at the single pixel level can also clearly be seen in Fig. 5.1.5a were the background noise of one pixel is shown for one night of data taking. The pronounced peak at the beginning of the night is again related to a star passing through the field of view. The approaching dawn is reflected in the rise of the noise level at the end of the data taking period. The FLT threshold is following the variance with the delay it takes the algorithm to adjust the trigger rate to the nominal value of 100 Hz per pixel. Variations at medium

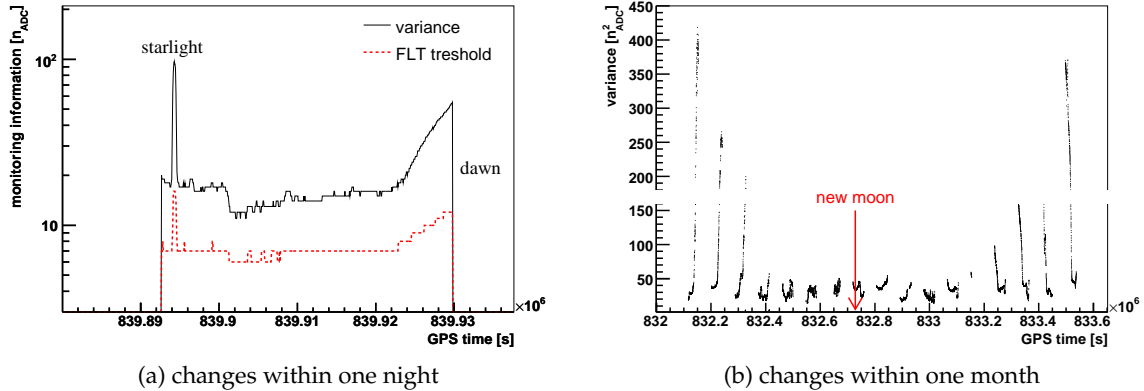(a) changes within one night   (b) changes within one month

Figure 5.1.5: The noise level and the FLT trigger threshold of a pixel are changing on different time scales ranging from minutes (left panel) to days (right panel).

time scales, $\mathcal{O}(\mathrm{day})$, are present due to the changing amount of moonlight. Although the moon is never in the field-of-view of an active telescope scattered moonlight is a significant contribution to the overall noise level. The effect is clearly visible in Fig. 5.1.5b, showing one complete data taking period.

Third Level Trigger

The Third Level Trigger is the first of two trigger levels running as software algorithms. On request it has the full event information from the front end electronics available. From the startup phase of the fluorescence detector until September 2007 a *prototype TLT* was assuring the selection of events and the reduction of noise triggers. It used the full ADC information from all FLT-triggered pixels to remove events caused by random noise triggered pixels. The readout of the ADC-traces is very time consuming and especially during periods with high event rates, mainly induced by lightning and air glow changes, large deadtimes were accumulated. The TLT algorithm has therefore been revised and an optimized version has been introduced [101, 102, 157]. This *multiplicity TLT* is making extensive use of the multiplicity signal, i.e. the number of triggered pixels as function of time, which is directly calculated in the electronics. This fast signal reduces the time needed to perform the selection of the events and reduces the deadtime. During the development of the algorithm, MC studies and tests on background events were used to verify the discrimination power and increased efficiency of the algorithm.

The new TLT algorithm has been imported into the $\overline{\mathrm{Off}}\underline{\mathrm{line}}$ simulation package and dedicated MC simulations have been performed to study the properties of the new algorithm and its influence on the hybrid detector exposure. The same simulated air showers have been passed through both the prototype TLT and the multiplicity TLT and the efficiency of the different algorithms has been derived. Especially important for this work is the dependence of the trigger efficiency on the energy and the distance of the shower to the fluorescence detector. As can be seen in Fig. 5.1.6, the false rejection of simulated events by the multiplicity TLT is reduced with respect to the prototype TLT. This increases the detection range of air showers and the available detector volume and has to be taken into account during the exposure
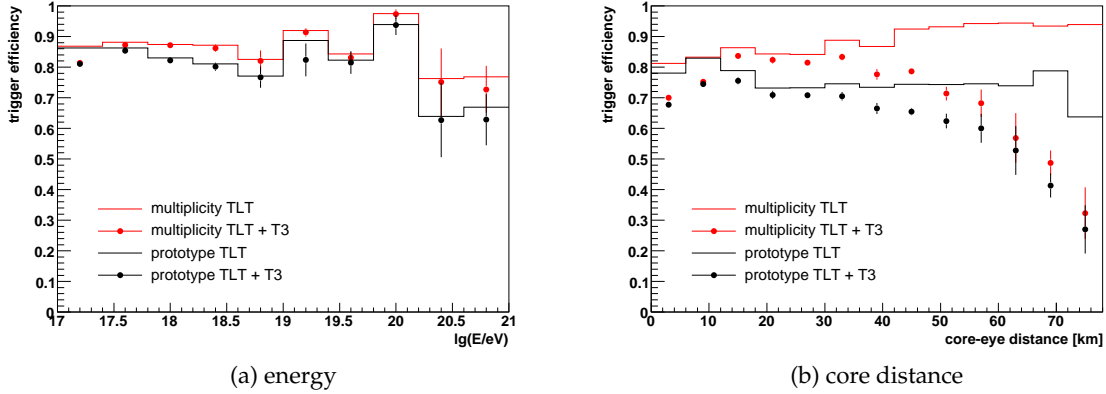
(a) energy

(b) core distance

Figure 5.1.6: Efficiency of the *prototype* and *multiplicity* TLT algorithms together with the T3 trigger derived from MC simulations. False rejection of air shower events has been reduced significantly and the time evolution of the algorithms has to be taken into account during the determination of the hybrid exposure simulations.

determination. As the modified trigger algorithm was implemented in the data taking only in September 2007 both TLT algorithms have to be used during the MC simulations.

In the next step of the data taking process the events are passed through the T3 algorithm. In the simulation study presented here, care has been taken to reproduce the exact settings active in the actual data taking software of the observatory. As can be seen in Fig. 5.1.6b, parts of the TLT enhancements are lost due to the remaining inefficiencies of the T3. It should also be noted that the observed differences between the trigger algorithms are reduced significantly if only high quality hybrid events are used.

5.1.4 Simulation of the surface array response

Surface detector arrays are sensitive to the lateral extend of EAS. Full MC simulations providing a 3D description of the air shower development are very demanding in computation time and the full coverage of the large parameter phase space needed for this study makes their use impossible. The fast hybrid simulation tool CONEX on the other hand does only provide one-dimensional longitudinal profiles of the evolution of the energy deposit, the muon number, etc. Still, this is sufficient to simulate hybrid events measured by the Pierre Auger Observatory as only the timing of the surface detectors is used during the event reconstruction (cf. Sec. 3.2.1). The absolute signal in each detector station is not relevant as only the relative signal height between triggered stations is used to select the station used for the hybrid geometry reconstruction.

The timing of the detector stations is provided by the local station trigger. The relevant trigger algorithm is the *time over threshold* (ToT) trigger, which is sensitive almost exclusively to the muonic part of the air shower. Muons are produced by decaying mesons close to the shower axis and travel due to their large boost-factors of about $\gamma = E/m \approx 2[GeV]/105[MeV] \approx 20$ over large distances without decaying. As they, in contrast to the electromagnetic component, don't suffer much from multiple scattering and energy losses, muons are dominating the leading edge of the shower, which in turn determines the trigger time in the surface de-
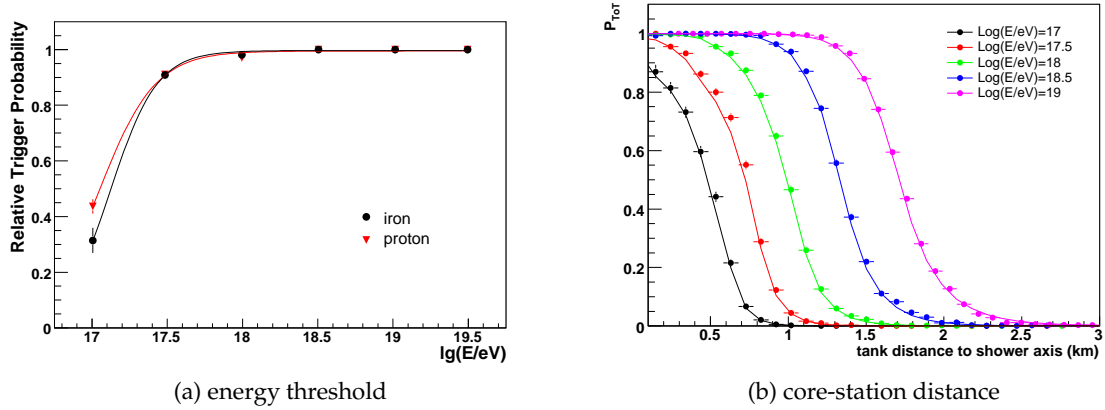
(a) energy threshold

(b) core-station distance

Figure 5.1.7: A full CORSIKA study has shown that the efficiency of the single station trigger is 100 % independent of the primary mass for showers with zenith angles $\leq 60°$ and energies $> 10^{18}$ eV (left panel). The core-station distance dependence (right panel) is taken into account by dedicated event selection criteria (from [158]).

tector station. Using the muon production profile, i.e. the number of muons produced in the EAS as function of geometrical height above the array, one is able to predict the time structure of the (muonic) shower front very accurately [159]. This model, which has been derived from extensive full MC AIRES simulations, has been implemented in the $\overline{\text{Off}}\underline{\text{line}}$ simulation framework as SDSIMPLESIM [160]. It provides a fast simulation of the surface detector response for the use in hybrid simulations. The lateral extend of the air shower is assumed to follow a NKG like functional form [161,162]. Particularly important is the incorporation of noise triggered stations, which could spoil the reconstruction of the events and introduce a difference between data and MC. The trigger threshold of the surface detector is self-adjusting to yield 100 Hz per station. As cross-check the number of noise triggered stations has been derived from the data themselves and the obtained distributions have been parameterized.

A crucial parameter of the hybrid exposure is the trigger efficiency of single surface stations at low energies, i.e. below the SD 3ToT-trigger threshold of $> 10^{18.5}$ eV [98]. It is depending on the total signal deposited in the station, which can not be obtained reliably from SDSIMPLESIM due to uncertainties in the used NKG parameterizations and important shower to shower fluctuations. Dedicated studies on full MC (CORSIKA) events have shown that the single tank efficiency is 100 % for showers in the parameter space [158]

- energy $> 10^{18}$ eV, and

- zenith angle $< 60°$.

The independence of the trigger efficiency of the mass of the primary particle within this range is illustrated in Fig. 5.1.7a. The dependence on the distance of the shower core from the station is shown in Fig. 5.1.7b. During the exposure determination the parameterized distance and zenith angle dependence is used on an event-by-event basis to reproduce the primary mass dependent trigger threshold. In this way the energy threshold of the hybrid

spectrum determination can be extended to energies below 10^{18} eV without biasing the result due to the unknown mass composition. Details will be discussed in Sec. 6.2.2.

During the simulation of the surface detector response with SDSIMPLESIM, the status of the surface array is required. The time evolution and status of each single station has been derived during the uptime determination (cf. Sec. 4.1.4) and the information is readily available by a newly implemented $\overline{\text{Off}\underline{\text{line}}}$ manager. All features of the growing array like missing stations due to deployment delays or hardware failures etc. are reproduced very accurately (cf. Fig. 6.1.4).

5.1.5 Invisible energy correction

As mentioned briefly in Sec. 3.2.4 the energy carried by the primary cosmic ray is transformed only partially into fluorescence or Cherenkov light. Especially charged pions decaying into muons and neutrinos contribute to the fraction of EAS energy not accessible by air shower measurements with fluorescence detectors. The *invisible energy factor f* is given by

$$f = \frac{E_{\text{tot}}}{E_{\text{cal}}} \, , \tag{5.1.2}$$

with E_{tot} being the total energy of the primary particle and E_{cal} the energy deposited by the EAS in the atmosphere. This factor has been extensively studied with full CORSIKA simulations [163] and a parameterization as function of E_{dep} has been derived for the QGSJET01 and SIBYLL 2.1 interaction models. The correction factor has been found to decrease with increasing energy, a fact, which can easily be explained by the increasing probability of pion interactions and the increase of the number of particle generations (see discussion in Sec. 2.1.1). Showers initiated by higher energy primaries are creating pions with higher momentum, i.e. their mean decay length increases. A higher decay length results in an increase of the pion interaction probability with nuclei in the atmosphere and the fraction of decaying pions decreases.

The properties of air showers initiated by heavy nuclei are well described by the superposition model, which has been introduced in Sec. 2.1.1. In this model, the increased invisible energy is due to the reduced primary energy $E \leftarrow {}^{E}/_{A}$. The increase of the invisible energy is enhanced by the increase of pions due to the larger number of hadronic interactions.

In addition also a dependence of the invisible energy correction factor on the zenith angle of the air shower is expected. Inclined showers travel longer through less dense parts of the atmosphere and the interaction probability should decrease. Higher zenith angles should therefore yield more pion decays and the energy transfered into the invisible part should increase. The effect has been found to be $\lesssim 1\,\%$ for zenith angles below $60°$ [163].

In order to take into account modifications of the interaction models, especially the replacement of QGSJET01 with QGSJETII-03, the invisible energy correction factor has been derived from the large sample of CONEX simulations used as input of the REALMC detector simulation. These showers cover a large energy range from 10^{17} eV $- 10^{21}$ eV and a large zenith angle range from $0° - 75°$. Showers were simulated with both proton and iron primaries and based on the QGSJETII-03 and the SIBYLL 2.1 hadronic interaction models. The fraction of energy invisible to the fluorescence detector has been determined on

(a) Sibyll 2.1, proton

(b) Sibyll 2.1, iron
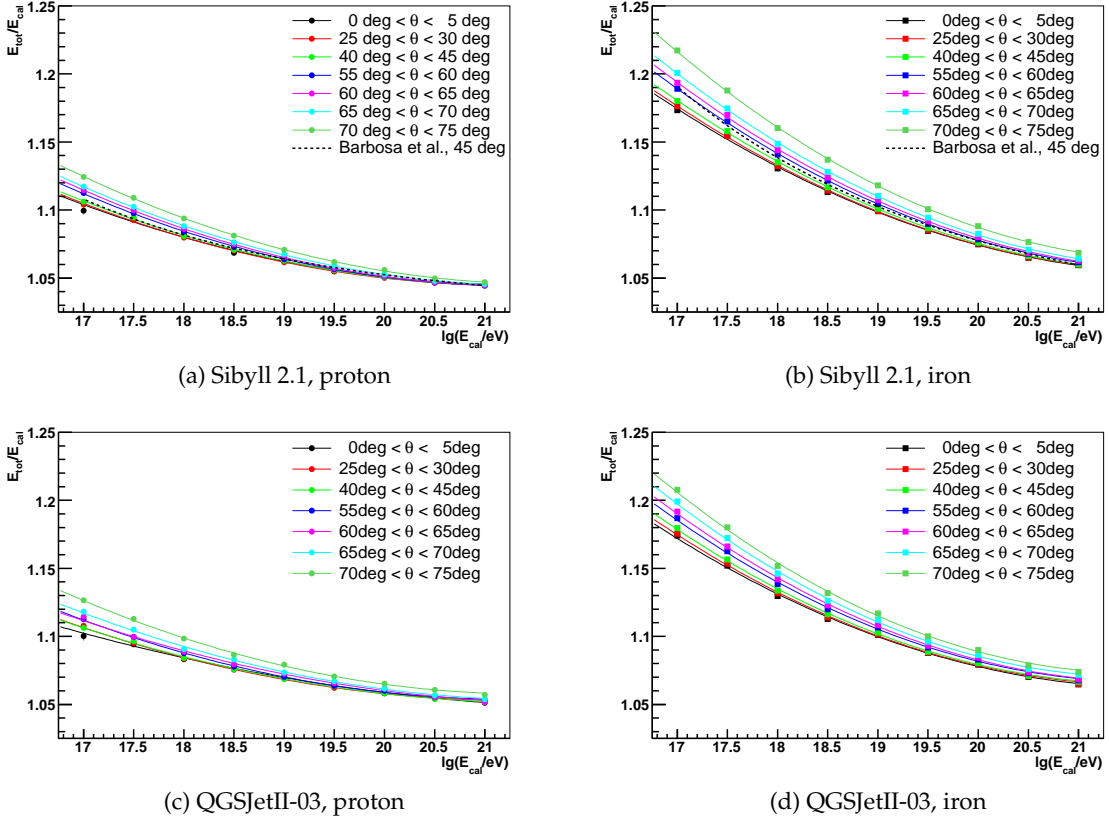
(c) QGSJetII-03, proton

(d) QGSJetII-03, iron

Figure 5.1.8: Invisible energy correction derived from CONEX simulations.

a shower-by-shower basis following the approach of [163]. In CONEX particles falling below the energy threshold during the air shower evolution are assumed to deposit their remaining energy locally taking into account particle type dependent efficiency factors. Their energy is added to the dE/dX profile. The energy deposited in the atmosphere E_{cal}^{atm} can therefore be determined by integrating the dE/dX profile obtained with CONEX. Particles remaining at ground level are taken into account depending on their type. The remaining energy in the electromagnetic component is added completely to E_{cal}^{atm}. The hadronic part of the shower, which includes muons has to be corrected with an efficiency factor ($\varepsilon_{had}(\text{ground}) = 0.61$ [163]):

$$E_{cal} = E_{em}(\text{ground}) + \varepsilon_{had}(\text{ground}) \cdot E_{had}(\text{ground}) + \int_0^{X_{ground}} dE/dX dX \qquad (5.1.3)$$

As can be seen in Fig. 5.1.8, the obtained invisible energy correction factors agree with the ones derived by [163] for the common zenith angle range. Above zenith angles of $60°$ large deviations are observed. The fraction of the total energy transferred into the invisible part is increasing as expected with increasing zenith angles. The zenith angle dependence amounts to a difference of about 2% between the previously used parameterization (Barbosa et al, $45°$) and the new one (SIBYLL 2.1, $75°$) at 10^{18} eV. The obtained correction factors have been parameterized as function of energy and zenith angle. They are applied during the reconstruction of the simulated showers by using the known interaction model and composition.
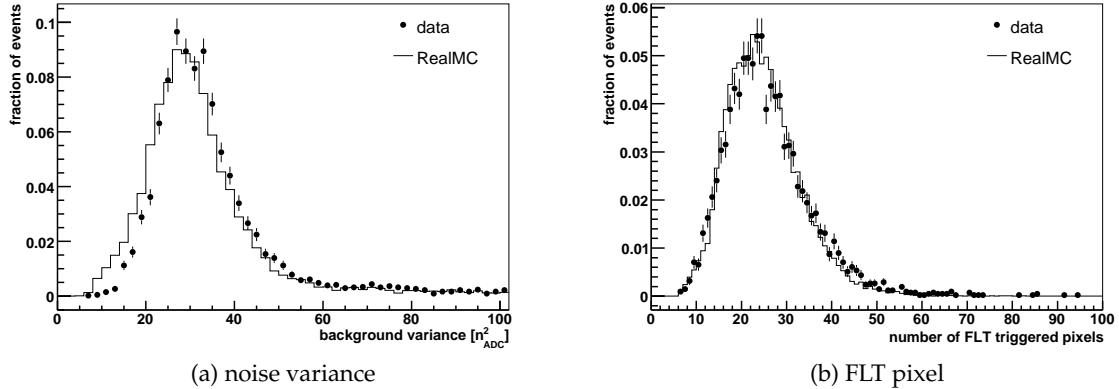
(a) noise variance

(b) FLT pixel

Figure 5.2.9: The developed REALMC scheme is able to reproduce the background noise level (left panel) as well as the number of FLT triggered pixels (right panel).

During data reconstruction the primary composition is a priori not known and a mixed, 50 % proton and 50 % iron, composition is used. As interaction model the recent QGSJETII-03 model is used. The remaining systematic uncertainty due to the difference between the interaction models and mass composition of about 4 % [131] is still valid.

5.2 Validation of the REALMC simulation and results

Probably the most important step in developing MC simulation tools is their validation with the help of real data. These comparisons, that should be done on all scales and simulation steps are described in the following.

5.2.1 Background noise and FLT

The basic level of the simulation of the fluorescence detector is the simulation of the telescope system, the photomultiplier and the readout electronics. Due to the extensive use of monitoring information like the background light variations and the connected FLT thresholds, these simulations have become very realistic. For example the noise level observed in data can be reproduced very well (cf. Fig. 5.2.9a).

A measure of the full simulation chain at the basic level of electronics, including the implemented first trigger level, is the total number of triggered pixels in an event. This basic and important comparison has some subtleties, which need to be taken into account. High energy showers as well as showers close to the detector are causing more pixels to trigger than low energy showers far away from the telescope. Therefore the comparison between simulations and data of the FLT pixel distributions has to use a reasonable assumption of the cosmic ray energy spectrum and scan all possible air shower geometries. This has been done by using the spectrum derived in this work (cf. Sec. 7) and a REALMC simulation covering the same phase space found in the data. As can be seen in Fig. 5.2.9b, the obtained MC distribution is in perfect agreement with the data.

(a) longterm evolution
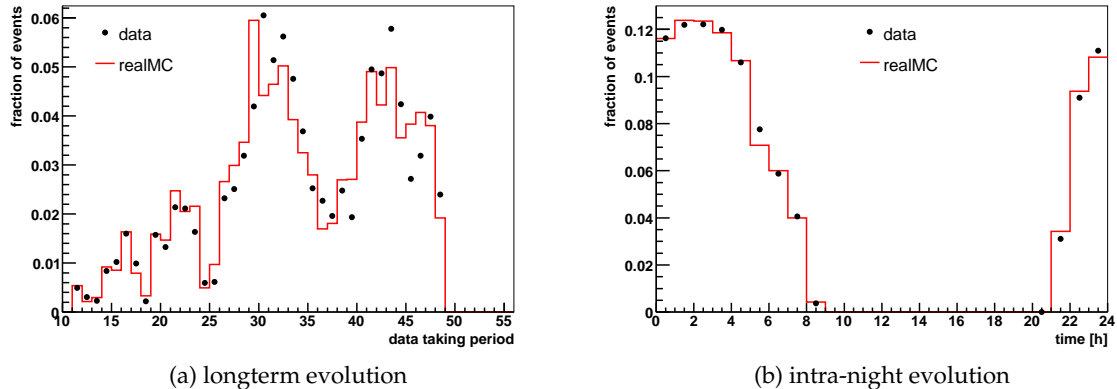

(b) intra-night evolution

Figure 5.2.10: The time dependent MC approach is able to reproduce the evolution of the event rate with time over the last years taking into account the construction of the observatory and seasonal variations (left panel). The event rate is also changing within one night of data taking due to the changing background noise (right panel).

5.2.2   Time dependences

The implemented REALMC scheme is designed to reproduce the actual data taking conditions of the Pierre Auger Observatory over a time period of more than three years. During that time the observatory was in its construction phase. The growing surface array and the commissioning of new fluorescence buildings led to an overall growth in the recorded event rate. The fraction of events recorded per data taking period, i.e. moon cycle, is also sensitive to seasonal variations. During the winter period nights are longer and the data taking time is increased. The MC should reproduce the hardware modifications and take into account the real running times of the experiment. The comparison of the predicted hybrid event rates with the real data is therefore a possible MC validation. Although some differences remain, the overall reproduction of the event rates as function of time is reasonably good (cf. Fig. 5.2.10a).

As can be seen in Fig. 5.1.5a, the changing background noise during one night of data taking influences the data taking conditions quite strongly. Higher noise levels at the beginning and the end of the night causes the FLT thresholds to rise. With higher thresholds only very close or high energy showers are able to trigger the readout. As not only the overall event rate decreases but also the trigger selection is inhomogeneous to different energies this effect has to be reproduced in the MC to increase the reliability of the exposure determination. In addition to this most important correlation, other environmental effects are modulating the event rate over one night to a lesser extend. For example, dust, which has been raised during the day by ranging activities or fires, causes absorption layers in the lower part of the atmosphere, which settle during the night. These layers can cause distortions of longitudinal profiles and consequently affect the event selection efficiency. Based on the hourly CLF aerosol measurements these effects are taken into account in the MC simulations. Another possible effect is the changing temperature and humidity of the atmosphere during one night. At the time being not enough data from radio sonde measurements are available to study or even quantify this effect. More data are going to be collected in the near future

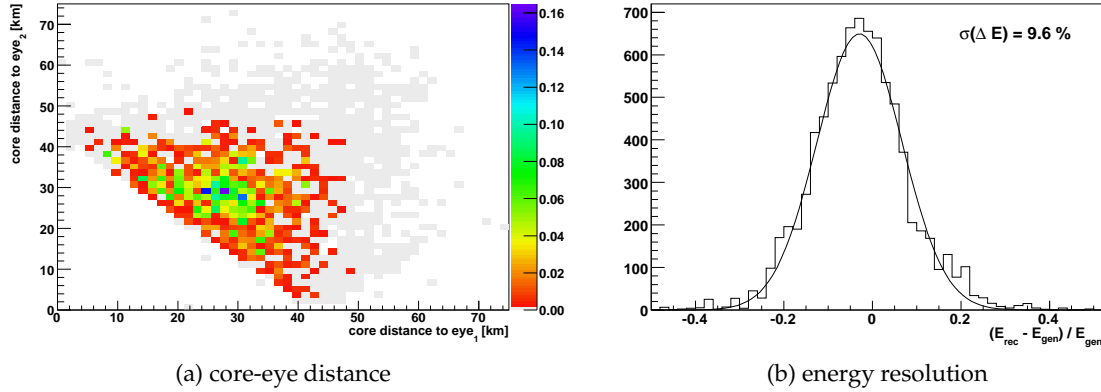(a) core-eye distance

(b) energy resolution

Figure 5.2.11: Multi-eye events are distributed asymmetric with respect to the eyes (left panel). Even applying only basic quality selection criteria the obtained energy resolution is very good (right panel).

and solid statistical analyses will hopefully improve the currently used monthly averaged models of the molecular atmosphere shown in Fig. 5.1.1b.

5.2.3 Multi-eye events

The four eyes of the fluorescence detector of the Pierre Auger Observatory operate independently from each other. This independence is also kept during standard event reconstructions. An air shower detected by more than one fluorescence detector station, a *multi-eye event*, is reconstructed multiple times. An example for such an event is shown in Fig. 3.2.16. The agreement between the reconstruction results can be used to study systematic effects of the applied reconstruction algorithms or the hardware setup itself.

Multi-eye events can also be used to study the overall efficiency of the fluorescence system and compare this fundamental and important quantity with the REALMC simulations. The number of multi-eye events is naturally depending on the energy of the detected air showers. High energy showers produce more light and can be seen also far away from the detector. A direct comparison between data and MC of the number of multi-eye events would therefore require assumptions on the UHECR spectrum $J(E)$. On the other hand, by normalizing the distributions to the total number of detected events in a given narrow energy range this complication disappears. The *multi-eye fraction R_i*, defined as the ratio between the number events that have been detected by i eyes simultaneously, n_i, and events, which have been detected by at least one fluorescence detector, N, reads

$$R_i(E) = \frac{n_i(E)}{N(E)} \propto \frac{J(E) \cdot \prod\limits_{j=1}^{i} \varepsilon(E)}{J(E) \cdot \varepsilon(E)} = \prod\limits_{j=1}^{i-1} \varepsilon(E) \;. \qquad (5.2.4)$$

$\varepsilon(E)$ is the combined efficiency of detection and event selection. The latter is strongly dependent on the used event selection criteria or *cuts*. Typical multi-eye events are rather asymmetric. Although the majority of them are detected in approximately equal distance between the two (or more) eyes, the distribution of events is becoming asymmetric due to the limited
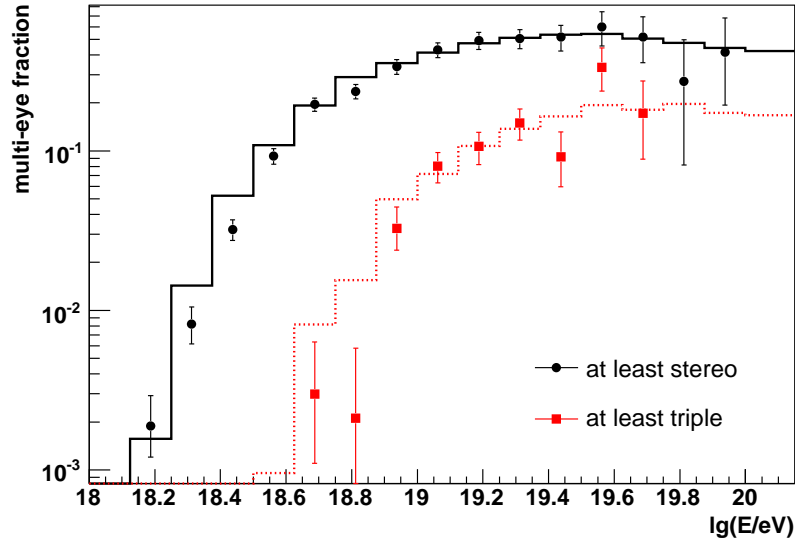
Figure 5.2.12: The fraction of events that have been detected by more than one fluorescence station is sensitive to the overall efficiency of the fluorescence detector including the uptime. Good agreement is found between data and REALMC .

viewing distance of the fluorescence detectors. This effect is illustrated in Fig. 5.2.11a. The cuts have to be applied to all available events and the available high quality multi-eye statistics is dropping significantly. Therefore the high quality selection criteria for the events used in the measurement of the hybrid spectrum as discussed in Sec. 6.2, cannot be used here. To circumvent this problem only basic quality selection criteria have been applied to retain a sufficiently high number of events:

- X_{max} has to be observed,

- energy reconstruction uncertainty $< 50\,\%$,

- zenith angle $< 60°$,

- distance between shower core and closest SD station $< 1.5\,\mathrm{km}$.

The achieved energy resolution of these events ($\approx 10\,\%$, cf. Fig. 5.2.11b) is good enough to be able to derive the energy dependence of R_i reliably. This ratio, shown in Fig. 5.2.12, shows good agreement between data and MC. A small difference at low energies is removed during the hybrid spectrum event selection by applying a fiducial volume criterion.

Thus, the developed MC scheme is able to reproduce the real data on all levels and can, therefore, be used to simulate the exposure of hybrid measurements of the Pierre Auger Observatory (cf. Sec. 6) or study detector properties like its resolution.

5.2.4 Detection and reconstruction accuracy

One goal of MC simulations is the determination of the detector and reconstruction uncertainty, i.e. the resolution of the detector. A reliable estimation of the detector resolution is
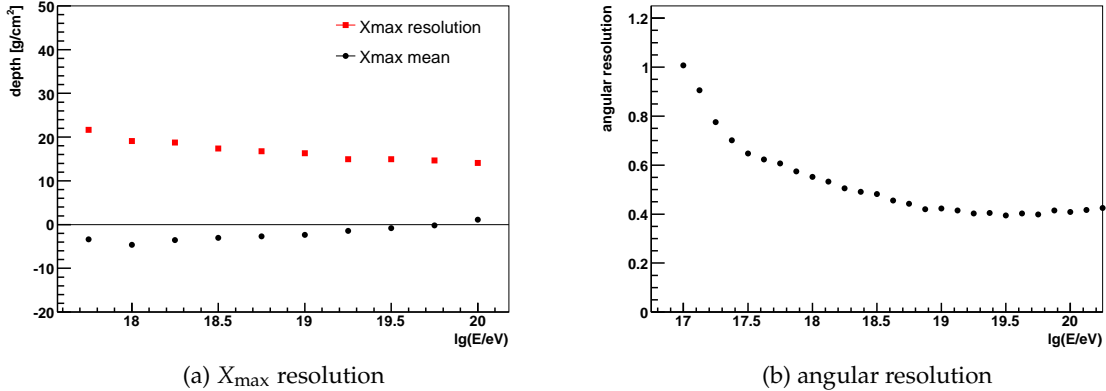
(a) X_{max} resolution

(b) angular resolution

Figure 5.2.13: REALMC simulations are used to determine the accuracy of measuring the shower maximum X_{max} (left panel) and the angular resolution (right panel) of hybrid measurements of the Pierre Auger Observatory.

needed for basically all physics interpretations of measured data. In the case of fluorescence detectors one additional complication comes into play, which underlines the importance of MC simulations. The measurement accuracy is strongly influenced by the event selection criteria. The quality of fluorescence and hybrid events is depending on a variety of parameters like the air shower geometry and the primary energy. Typically, high energy showers produce a stronger signal in the detector and the reconstruction accuracy increases.

The developed MC scheme has been used to determine the resolution for several analyses and only examples can be discussed here. As illustration, the resolution of the parameter sensitive to the primary mass composition, X_{max}, and the angular resolution of hybrid measurement is derived. The energy resolution, which is the most important parameter for this work, is discussed in detail in Sec. 6.2.1 after dedicated event selection criteria have been chosen.

The evolution of $\langle X_{\mathrm{max}} \rangle$ with increasing energy is often studied to search for changes in the primary mass composition (cf. Sec. 2.2.2). To be able to discriminate between air showers initiated by different primary (hadronic) particles, a high accuracy in the determination of the position of the shower maximum X_{max} is essential. As can be seen in Fig. 5.2.13a, a resolution of less than $20\,\mathrm{g/cm^2}$ is achieved with hybrid measurements of the Pierre Auger Observatory. The precise knowledge of this resolution is required for the interpretation of the X_{max} fluctuations, which will allow the reduction of the dependence on the details of the hadronic interaction models. A crucial point of the mass composition analysis is the event selection, which should not introduce a bias in the X_{max} distribution and allow for a high precision in the determination of the primary energy. The quality selection criteria have been derived from extensive REALMC simulation studies [141]. The fiducial volume selection criteria take into account the status of the detection system (cf. Sec. 4.3) and are based on the data themselves.

The angular resolution of the Pierre Auger Observatory has been extensively studied for events recorded with the surface array (e.g. [164]). Due to the high duty cycle their statistical power is superior to hybrid measurements and surface detector events have, for example,

led to the observation of anisotropy, reflected in the correlation between UHECR and nearby AGN [47, 48]. In order to use the additional, mass sensitive, information provided by hybrid measurements the angular resolution of these events has to be determined [51]. No analytical formula can be derived and multi-eye analyses are limited by statistics, REALMC simulations can be used to determine the angular resolution. Again, the result is depending on the applied quality selection criteria and the primary energy. The following selection criteria have been developed within a dedicated working group

- χ^2/ndof of the SDP determination < 7 (cf. Eq. (3.2.2)) ,

- χ^2/ndof of the shower axis determination < 8 (cf. Eq. (3.2.5)) ,

- distance between shower core and closest SD station $< 2\,\text{km}$,

- observed angular track length $> 15°$.

As illustrated in Fig. 5.2.13b, an angular resolution, defined as the angular radius that would contain 68 % of showers coming from a point source, of less than 1° above 10^{17} eV and about 0.5° above 10^{18} eV is found with these criteria. After more statistics has been accumulated in the near future, this extremely good resolution should enable point source studies. Combining the mass sensitivity of hybrid measurements with assumptions on the UHECR sources, galactic and extragalactic magnetic fields, important consistency checks can be performed and additional information on the sources of galactic and extragalactic cosmic rays can be derived [51].

Chapter 6

The hybrid exposure of the Pierre Auger Observatory

The aperture of an optical detector like the fluorescence system of the Pierre Auger Observatory is strongly depending on the air shower energy and atmospheric parameters, especially Rayleigh and Mie scattering lengths. The maximum shower distance up to which the detector will trigger can be estimated based on very basic arguments [165], valid for every optical detector focusing fluorescence light onto an array of photomultiplier tubes. The light produced by an air shower of size N_e passing by the detector at a distance R_p is scattered on molecules and aerosols. Combining both processes into a single extinction length r_{atm}, one can derive the number of recorded photons N_{ph} as

$$N_{ph} = N_e \, Y \, \frac{A_{ap} Q}{4\pi R_p^2} \, \exp\left(\frac{-R_p}{r_{atm}}\right) \, R_p \Delta\theta \, , \tag{6.0.1}$$

where Y is the fluorescence yield given in photons per meter and A_{ap} the aperture of the telescope. The phototubes are characterized by their quantum efficiency Q and their field of view $\Delta\theta$.

During the integration time t_{trig}, which is needed for the trigger threshold calculation, N_{BG} background photons are collected:

$$N_{BG} = \phi_{BG} \, t_{trig} \, A_{ap} \, Q \, (\Delta\theta)^2 \, , \tag{6.0.2}$$

where ϕ_{BG} denotes the background photon flux. With the signal to noise ratio $n_{trig} = N_{ph}/\sqrt{N_{BG}}$, the minimum shower size N_e^{thr}, which is required to be able to trigger the detector at a maximum shower-eye-distance R_p can be written as:

$$N_e^{thr} = n_{trig} \, 4\pi R_p \, \exp\left(\frac{R_p}{r_{atm}}\right) Y^{-1} \sqrt{\frac{\phi_{BG} t_{trig}}{A_{ap} Q}} \, . \tag{6.0.3}$$

It is interesting to note that the trigger threshold N_e^{thr} is not depending on the size of the pixels and depends only weakly on other detector parameters like aperture area, etc. On
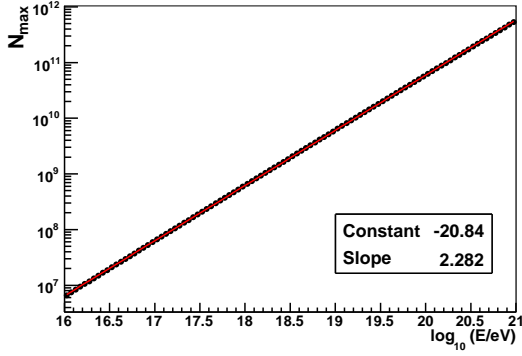
Figure 6.0.1: CONEX simulations allow to derive a simplistic relation between the shower size at the shower maximum and the primary energy.
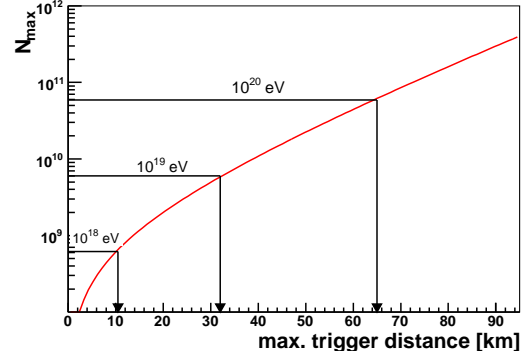

Figure 6.0.2: General features of optical air shower detectors can be used to derive the maximum distance at which the detector will trigger [165].

the other hand, Eq. (6.0.3) underlines the importance of accurate measurements of the atmospheric parameters. For the fluorescence detector of the Pierre Auger Observatory the parameters of this simplistic equation are given as

- $n_{\text{trig}}^{\text{FLT}} \approx 5.5$ per pixel(with at least 4 triggered pixels required for the SLT (cf. Fig. 3.2.5))

- $r_{\text{atm}} \approx 20\,\text{km}$ (cf. Fig. 3.2.15a)

- $Y \approx 4\,\text{m}^{-1}$ [132]

- $\phi_{\text{BG}} \approx 6 \cdot 10^5\,\text{m}^{-1}\text{sr}^{-1}\text{s}^{-1}$ [155, 156]

- $t_{\text{trig}} = 1\,\mu\text{s}$, FLT integration time

- $A_{\text{ap}} = \pi r_{\text{ap}}^2 = \pi (1.7\,\text{m})^2$

- $Q \approx 0.25$

Eq. (6.0.3) cannot be inverted analytically to obtain the shower-eye distance at which the detector will trigger as function of the shower size. On the other hand one can simplify the complex relation between shower geometry and development by assuming that the shower reaches its maximum, i.e. $N_e \equiv N_{\text{max}}$ at the distance R_p. The number of particles at the shower maximum can be converted into primary energy for example with the help of CONEX shower simulations. As shown in Fig. 6.0.1, a simple exponential relation can be derived for a large energy range. With this simplistic translation between shower size N_{max} and energy, a rough numerical evaluation of Eq. (6.0.3) is possible. Fig. 6.0.2 shows the derived minimal shower size as function of the maximum distance between shower and detector.

Whereas the above considerations are very useful to understand the dependence of the FD-trigger volume on the primary energy, detector configuration and atmospheric conditions, a precise determination of the aperture requires detailed MC simulations. Especially the full time dependence of atmospheric and detector parameters can be taken into account.
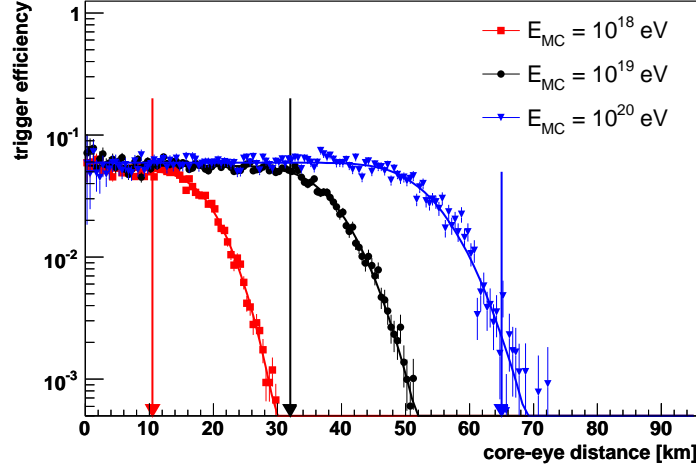
Figure 6.0.3: The simplistic semi-analytical calculation of the maximum distance up to which an air shower will trigger the detector (arrows) shown in comparison with full REALMC detector simulations.

The resulting shower distances at which the trigger becomes inefficient are reproduced much more accurately. On the other hand, given the simplifications of the semi-analytical calculation, it is remarkable that the derived trigger thresholds are at low energies in rather good agreement with the detailed MC simulations. As illustrated in Fig. 6.0.3, deviations appear only at highest energies.

In order to derive an exposure with very small systematical uncertainties, only high quality hybrid events have to be used. The event reconstruction quality and therefore the selection efficiency is depending on a variety of parameters. For example the full shower geometry and not only the distance to the detector has to be taken into account. Other intrinsic parameters like atmospheric conditions, etc. are time dependent. The final selection efficiency ε can therefore not be disentangled from the detector evolution or derived analytically. On the other hand it can be derived from MC simulations scanning an area A_{gen} large enough to contain the full detector array. It should include the efficiencies at the various steps of the analysis, namely the trigger, reconstruction and selection efficiencies and the detector evolution during time T. The exposure $\mathcal{E}$ can be evaluated as

$$\mathcal{E}(E) = \int_T \int_\Omega \int_{A_{\mathrm{gen}}} \varepsilon(E, t, \theta, \phi) \, \mathrm{d}S \, \cos\theta \, \mathrm{d}\Omega \, \mathrm{d}t \, , \tag{6.0.4}$$

where $\mathrm{d}\Omega = \sin\theta \mathrm{d}\theta \mathrm{d}\phi$ and Ω are respectively the differential and total solid angles.

6.1 REALMC **simulation to determine the hybrid exposure**

The MC simulations used to calculate the hybrid exposure have to cover a large parameter space ranging from hadronic interaction models to very different air shower geometries and detector setups.

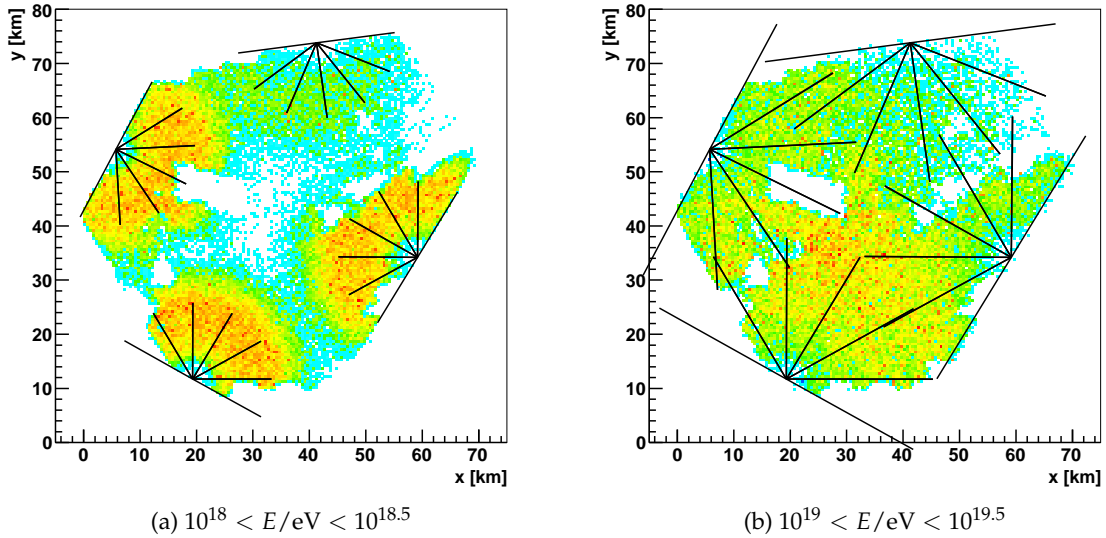(a) $10^{18} < E/\text{eV} < 10^{18.5}$ (b) $10^{19} < E/\text{eV} < 10^{19.5}$

Figure 6.1.4: The surface area covered by hybrid events is limited to the active surface array. The time evolution of the detector is taken into account in these REALMC simulations. The available detection area is growing with increasing energy as high energy shower emit more light and can be seen further away from the detector.

As discussed in Sec 5.1, the basic ingredient to air shower simulations are models describing the hadronic interaction at ultra-high energies. Although their predictions for parameters of relevance such as the shape of the longitudinal energy deposit profile or the invisible energy do not differ much, their influence on the exposure has to be studied. This is done by using two of the currently available models, SIBYLL2.1 and QGSJETII. They have been selected also because their predictions can be considered as the extreme cases among the available models [*]. Showers are simulated with both models in equal parts and their influence on the exposure is discussed below.

The next a priori unknown parameter is the mass composition of the primary cosmic rays. At the highest energies studied in this work, photon and neutrino primaries are (if at all) contributing a very minor fraction of the total flux and can be neglected (cf. Sec. 2.2.2). On the other hand already the two extreme assumptions of hadronic primaries, hydrogen and iron nuclei, are causing rather large differences in the longitudinal development and light emission. Heavy nuclei penetrate less deep in the atmosphere, initiate more hadronic interactions and more energy is transfered to non-visible particles like neutrinos and muons. The influence of these effects on the exposure is studied by simulating both proton and iron primaries to equal parts. Details like dedicated restrictions of the fiducial volume that can compensate the differences are discussed in Sec. 6.2.2.

The geometrical phase space of hybrid observations is, in contrast to pure fluorescence measurements, limited by the condition that the air shower has to fall close the active surface detector array. The layout of the array shown in Fig. 3.1 is reflecting the status at the end of

---

[*]Certain predictions of the first version of EPOS [166] are very different from other models. As EPOS is currently undergoing a major revision [167] it has not been considered for this work.

the data taking period discussed here (05/2008). The full detection area has to be scanned by simulated showers in order to cover all possible air shower geometries. It should be noted that the volume used for the simulations is exceeding the ground area, as inclined shower may develop rather far outside and just hit the ground inside the array. The area, which is covered by the simulations is conservatively enclosed in a $80\,\text{km} \times 80\,\text{km}$ square. The on-going construction of the surface array is taken into account in the REALMC simulations as discussed in Sec. 5.1.4. Integrating over the full time period, the distribution of triggered events is reflecting the construction of the surface array as well as the consecutive commissioning of the fluorescence detectors. As discussed above the available fiducial volume is increasing with energy as high energy showers produce more light and are therefore visible further away from the detector. All these effects are reflected in the obtained core position distributions shown in Fig. 6.1.4.

The REALMC Simulations are based on an UPTIME definition, which does not contain the event loss due the T3-veto algorithms. As discussed in Sec. 4.1.3, the veto algorithms acting on the FD and CDAS side cannot be disentangled due to missing monitoring information. In addition, the independent trigger of the surface array is able to recover large fractions of the vetoed events especially at high energies. The calculation of this recovery has to rely on calculations of the surface detector trigger threshold. This has been done by using CORSIKA simulations [98]. The recovery is taken into account during the exposure calculation on an event-by-event basis using the energy E_i of the simulated air showers. Based on the parameterized 3ToT probability $\varepsilon_{3ToT}(E_i)$ shown in Fig. 4.1.5a and the probability during a given time interval t_i to pass the T3 filters $\varepsilon_{\text{T3veto}}^{\text{raw}}$ (cf. Eq. (4.1.4)), the probability of a triggered fluorescence event to be recorded as hybrid event P_{hybrid} is given by

$$P_{\text{hybrid}} = 1 - \left[(1 - \varepsilon_{\text{T3veto}}^{\text{raw}}(t_i)) \cdot (1 - \varepsilon_{3ToT}(E_i)) \right] \ . \tag{6.1.5}$$

The response of the surface array itself is simulated with SdSimpleSim (cf. Sec. 5.1.4). SdSimpleSim has been conceived to reproduce the essential ingredient of hybrid reconstructions, i.e. the timing resolution of the surface detector stations. The total signal and the related station trigger probability is simulated but the accuracy of the corresponding predictions for the trigger threshold is not sufficient for this work. In order to increase the reliability of the efficiency determination, the applied single station trigger probability is relying on the LTPs derived from full CORSIKA simulations [158]. To avoid double counting of trigger probabilities, the trigger of the closest station to the shower core is set manually during the simulation and only the timing of the station signal is taken from SdSimpleSim. In this way all simulated events have at least one triggered stations, i.e. the event are always simulated as *hybrid*. Although it has been shown that the single tank trigger probability is 100 % for the energies and geometries selected for the spectrum determination, the parameterized trigger probabilities are taken into account in a Hit-or-Miss approach later during the event selection procedure. This ensures the validity of the simulated efficiencies also outside the actual event selection parameter space and removes possible threshold effects.

To numerically calculate the hybrid exposure given in Eq. (6.0.4), the full time period has to be scanned accurately. As discussed in Sec. 4, the time period between 01/2004 and 05/2008 has been subdivided into 10 min bins in order to be able to calculate the detector uptime reliably. With a total of about $5 \cdot 10^7$ randomly selected timestamps over the full time

period T, every 10 min time bin has been sampled about 300 times. This accuracy is needed as the time-sampling is only one parameter in the multi-dimensional parameter space of Eq. (6.0.4). The high density of random time stamps assures that all different detector setups are taken into account in the simulations and that the statistical uncertainty of the calculated exposure is much smaller than the statistical uncertainty due to the number of observed events.

Both the integration over time and the integration over the available surface A_{gen} is performed during the REALMC simulation. The final exposure calculation can therefore be written as

$$\mathcal{E}(E) \;=\; \int_T \int_\Omega \int_{A_{\text{gen}}} \varepsilon(E,t,\theta,\phi)\, \mathrm{d}S\, \cos\theta\, \mathrm{d}\Omega\, \mathrm{d}t \tag{6.1.6}$$

$$\;=\; T\, A_{\text{gen}}\, 2\pi\, \Delta\cos\theta \sum_{\cos\theta_i} \frac{N_{\text{sel}}(E,\cos\theta_i)}{N_{\text{gen}}(E,\cos\theta_i)}\, \langle\cos\theta_i\rangle \ . \tag{6.1.7}$$

The last step is a summation over all zenith angles of a binned distribution with bin-width $\Delta\cos\theta$. The efficiency ε is including both trigger and selection efficiencies.

The raw exposure collected at trigger level is shown in Fig. 6.2.5. The exposure is approaching the one obtained with the surface detector at high energies as the fluorescence detector becomes 100 % efficient over the full array. The event selection for the determination of the energy spectrum from surface array data requires that all six stations surrounding the one with the highest signal are operational. This condition is significantly reducing the available detection surface as boundaries around missing stations are removed. This "T5-condition" is not needed for hybrid events, as already the signal from one surface detector station is sufficient for a reliable reconstruction. The detection surface available for high energy hybrid events is therefore larger than the one used for the surface array spectrum. On the other hand, it is not possible to use most of these events for the spectrum determination due to large reconstruction uncertainties.

6.2 Event selection criteria

The trigger levels of the Pierre Auger Observatory have been designed to avoid the rejection of air shower candidates. Due to the correspondingly low trigger threshold, the bulk of recorded events is noise, i.e. single muon induced triggers. These events cannot be reconstructed and can easily be removed from the data set. On the other hand even measurements of real air showers are very sensitive to different shower geometries, atmospheric conditions, etc. The reconstruction accuracy and reliability of these events is varying very much and stringent quality criteria have to be applied to obtain a sample of high quality EAS measurements. In order to be able to use simulated showers to determine the exposure collected with the selected events, care has to be taken that the selection efficiencies for data and MC agree very well. This is assured by comparing the parameter distribution used for the selection. All event selection criteria are applied to both data and MC events.
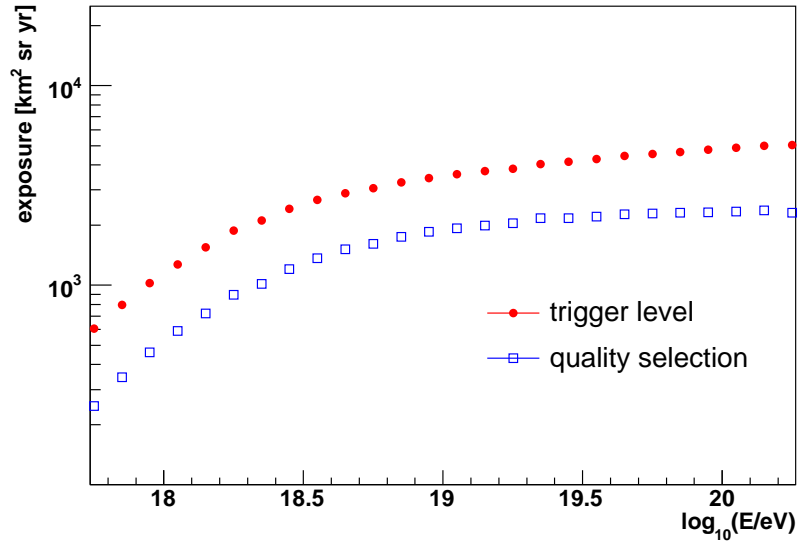
Figure 6.2.5: The hybrid exposure at trigger level and after passing all quality selection criteria.

6.2.1 Quality cuts

Hybrid event selection is usually starting with basic criteria concerning the validity of the analyzed data. The main criterion is the selection of time periods with valid calibration constants. As explained in Sec. 5.1.2, the values obtained during the absolute calibration campaigns have to be corrected for a time dependent shift. The calculation of these time dependent calibrations *constants* is performed by a dedicated working group of the Pierre Auger Collaboration. Currently, calibration data of all four fluorescence buildings are available for basically the complete data taking period of the detectors:

- Los Leones: 12/2004 - 05/2008

- Los Morados: 06/2005 - 05/2008

- Coihueco: 12/2004 - 05/2008

The detection system in Loma Amarilla has not been fully commissioned and its data are not available for physics analysis yet.

During data taking only events passing the latest step of the trigger chain, the T3-trigger, are stored. The T3 algorithm performs a fast reconstruction of the shower geometry before sending a signal to CDAS. The construction of hybrid events by merging the information from the surface array with the fluorescence data is therefore depending on the successful reconstruction of the T3 information. The merging step is not reproducible in the REALMC simulations as the used algorithms are not available within the $\overline{\text{Off}}\underline{\text{line}}$ framework. In order to take possible inefficiencies into account, a valid T3 information is required during the MC event selection.

Very strong light pulses originating usually from showers close to the detector might cause overflows in the dynamic range of the ADCs. The determination of the timing and

(a) distance between shower core and SD-station
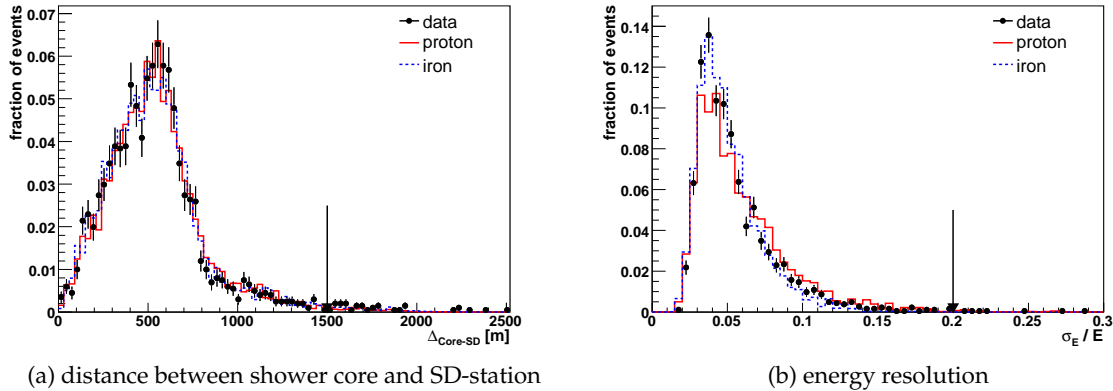

(b) energy resolution

Figure 6.2.6: Comparison between data and MC of the parameters used for the event selection. All event selection criteria, except the depicted one, are applied and the simulated showers are weighted following Eq. (6.2.8). The arrow denotes the event selection criteria.

height of the recorded signal (cf. Sec. 3.2.2) is currently not possible for a saturated ADC-trace and these events have to be discarded. A procedure to recover event with saturated pixels has been developed [168] but is not yet part of the official event reconstruction chain.

Especially for the determination of the cosmic ray energy spectrum, an excellent energy reconstruction is necessary. The energy determination is relying on the extrapolation of the observed longitudinal profiles outside the field of view of the telescopes (cf. Sec. 3.2.4). This extrapolation is only possible if large parts of the profile and especially the shower maximum has been observed. The observation of $X_{\max}$ is therefore a standard event selection criterion. In addition, the used Gaisser-Hillas functional form has to describe the measured profile very well. The selection of events with a reduced χ^2 of less then 2.5 is also an important criterion to remove measurements during unfavorable atmospheric conditions. Dust layers or clouds might obscure or enhance portions of the shower profile and thereby spoil the reconstruction. Extreme cases with parts of the profiles being totally obscured by clouds are rejected by removing events having holes in the longitudinal profile larger than 20 % of the total profile length. This cut also removes events, which are affected by a flaw in the current reconstruction algorithm: Shower signals crossing the boundaries of adjacent telescopes are not reconstructed perfectly and parts of the longitudinal profiles are neglected.

The statistical uncertainties of the shower geometry determination and the atmospheric measurements are propagated to the final statistical uncertainty of the reconstructed energy as discussed in Sec. 3.2.4. Well reconstructed air showers can therefore be selected by requiring a small uncertainty in the energy reconstruction. All events with $\Delta E / E > 20\%$ are discarded.

In addition to the fluorescence light, Cherenkov light is used as additional signal during the reconstruction. As the current reconstruction algorithm is not correcting for the lateral distribution of the Cherenkov light emitting electrons and positrons a reconstruction bias might be introduced. Events with Cherenkov light contributing more than 50 % of the total collected signal are therefore removed from the sample.
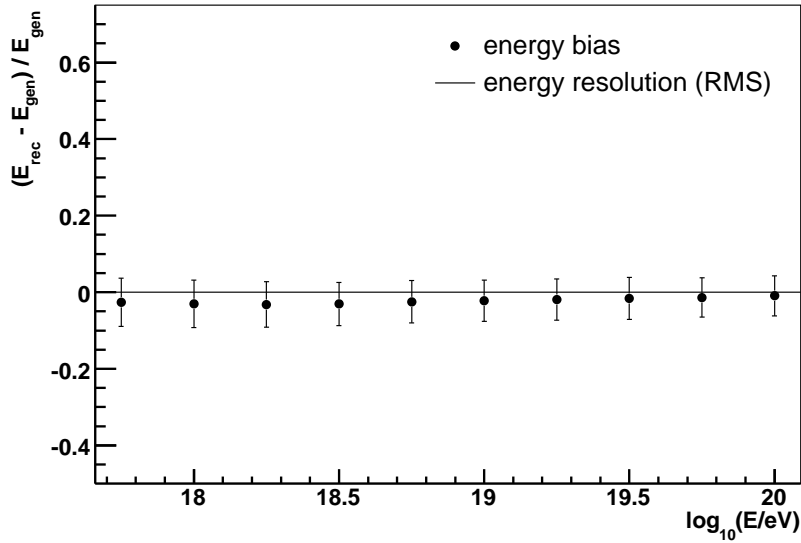
Figure 6.2.7: The energy resolution of the air shower reconstruction determined by REALMC simulations. Due to the strong quality requirements the energy resolution of the selected events is better than 10 % over the full energy range.

All selection criteria are checked for consistency between data and MC by comparing the cut parameter distribution. As most of the parameters are depending on the air shower energy, a realistic comparison is only possible if the simulated events follow approximately the same energy spectrum as the real data. This is achieved by weighting the simulated showers to follow a spectrum constructed by three power-laws $\phi \propto E^{-\gamma}$ with

$$\gamma = \begin{cases} 3.3 & \lg E/\text{eV} \leq 18.7 \\ 2.6 & 18.7 < \lg E/\text{eV} < 19.5 \\ 4.5 & \lg E/\text{eV} \geq 19.5 \end{cases} \tag{6.2.8}$$

All selection criteria, including the fiducial volume cuts described below, except the one under study are applied. Examples for the obtained distributions are shown in Fig. 6.2.6. All other distributions are given in the Appendix Sec. D.1. All distributions show good agreement between data and MC.

The resulting exposure collected over the full time period (11/2005 - 05/2008) is shown in Fig. 6.2.5 in comparison with the exposure at hybrid trigger level.

As can be seen in Fig. 6.2.7, the obtained energy resolution is less than 10 % over the full energy range. A small bias in the energy reconstruction of less than 3 % can be related to the profile extrapolation with the Gaisser-Hillas functional form. Constraints on the two Gaisser-Hillas shape parameters, X_0 and λ, have been derived from a high quality, but statistically limited data set of hybrid measurements (cf. Sec. 3.2.4 and Fig. 3.2.17). Especially at low energy, the derived constrains seem not to match the average shower shape. It is also very likely that the average Gaisser-Hillas parameters are energy dependent [169]. Further studies are ongoing. The related systematic energy reconstruction uncertainty is included in the overall energy scale uncertainty of 23 % (cf. Sec. 3.2.5).

(a) quality selection only

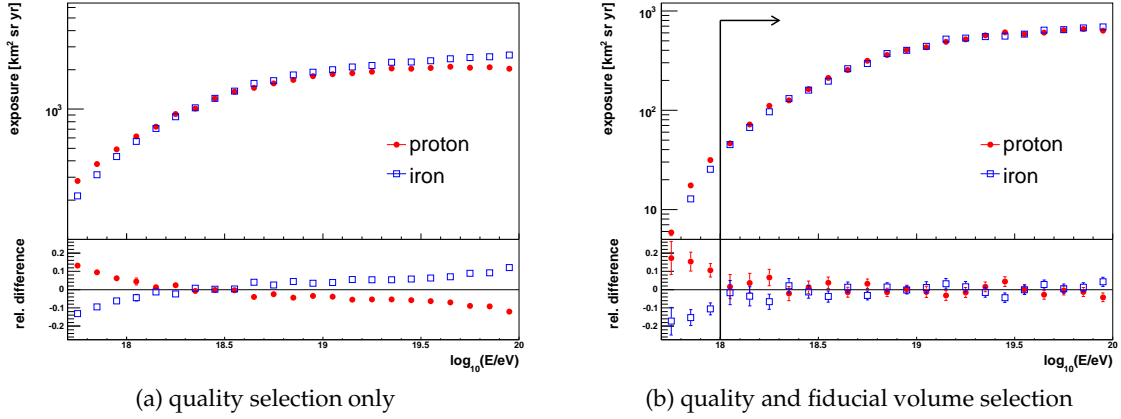(b) quality and fiducial volume selection

Figure 6.2.8: The limited field of view of the telescopes introduces a mass dependence of the selection efficiency (left panel) which is removed by dedicated fiducial volume cuts (right panel). The final hybrid exposure is independent from a priori assumptions on the mass of the primary cosmic rays above the energy threshold of 10^{18} eV.

6.2.2 Fiducial volume cuts

In addition to the above mentioned quality criteria, a set of fiducial volume cuts has been developed. They are assuring the stability of the exposure determination with respect to uncertainties in the trigger threshold, overall energy determination and mass composition.

The limited field of view in combination with the requirement of having the shower maximum inside the field of view of the detector is biasing the observable X_{max} distribution and therefore the mass composition sensitivity (see Sec. 4.3). Due to the a priori unknown mass composition this effect would introduce large systematic uncertainties on the exposure and the energy spectrum. This effect is clearly visible in Fig. 6.2.8a. In order to achieve equal sensitivity for all possible primary masses, i.e. an exposure, which is independent of the mass of the primary particles, dedicated event selection criteria have been developed in the context of the elongation rate studies [55, 141]. The following conditions have to be fulfilled:

$$X_{up}[\text{g/cm}^2] \geq 900 + 6 \cdot (\lg(E/\text{eV}) - 18) \tag{6.2.9}$$

$$X_{low}[\text{g/cm}^2] \leq \begin{cases} 550 - 61 \cdot (\lg(E/\text{eV}) - 19.06)^2, & \lg E/\text{eV} < 19.06 \\ 550, & \lg E/\text{eV} \geq 19.06 \end{cases} \tag{6.2.10}$$

X_{up} and X_{low} denote the upper and lower boundary of the possible telescope field of view depending on the air shower geometry. Only about 45 % of the events pass these stringent criteria and the available event statistics is decreased significantly. On the other hand, as can be seen in Fig. 6.2.8b, the final hybrid exposure is independent of the mass of the primary cosmic rays and the corresponding systematic uncertainty is removed.

Another important fiducial volume criterion has been introduced in order to remove trigger threshold effects and to achieve an exposure which is independent of possible energy scale uncertainties. As discussed above and illustrated in Fig. 6.0.3, the fluorescence detector trigger is fully efficient for short distances between the shower and the detector. At larger distances the trigger probability decreases. The exact position and shape of this

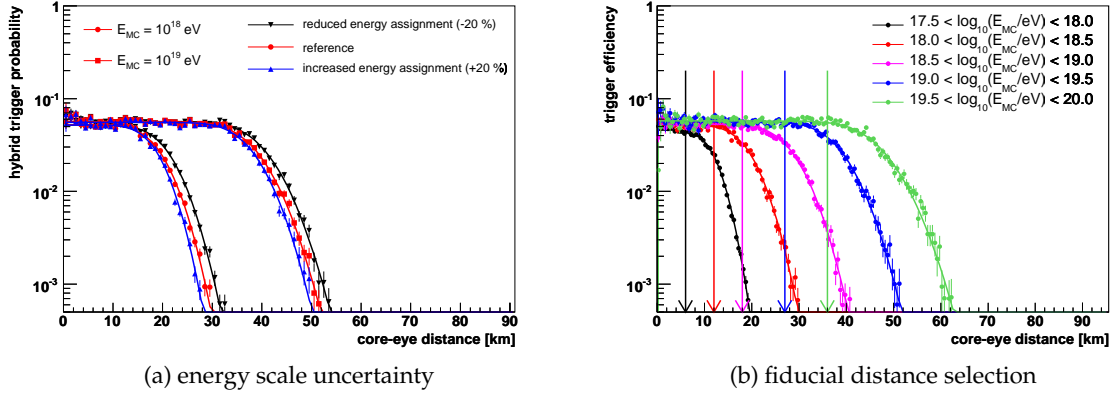(a) energy scale uncertainty

(b) fiducial distance selection

Figure 6.2.9: The systematic uncertainty of the absolute energy scale of about 23 % would cause significant systematic uncertainties of the fiducial volume and the exposure (left panel). Dedicated event selection criteria are used to remove this dependence (right panel).

energy dependent threshold is depending on various quantities like a very precise knowledge of the atmospheric conditions. In addition a possible systematic shift of the energy assignment to detected air showers may alter the derived trigger threshold and the exposure. A qualitative estimate of this uncertainty can be derived from a dedicated REALMC simulation. As illustrated in Fig. 6.2.9a, a false increase in the energy assignment leads to an apparent reduction of the fiducial volume. This effect can be understood for example by attributing the full energy modification to the fluorescence yield, which is currently the largest systematic uncertainty of the energy assignment. Increasing the fluorescence yield during the shower simulations leads to more light emission and the showers will trigger the detector up to larger distances. Decreasing the yield is leading to the opposite effect and a reduced fiducial volume. The modification of the trigger threshold by a systematic shift in the energy assignment shown in Fig. 6.2.9a can be removed by dedicated selection criteria. The available detection volume is limited by a set of fiducial volume cuts which require the shower core to lie within the following range $D_{\max}$ from the fluorescence detectors:

$$D_{\max}[\text{km}] \leq \begin{cases} 24 + 12(\lg(E/\text{eV}) - 19) & \lg E/\text{eV} < 18.5 \\ 24 + 12(\lg(E/\text{eV}) - 19) + 6(\lg(E/\text{eV}) - 18.5) & \lg E/\text{eV} \geq 18.5 \end{cases} \quad (6.2.11)$$

These criteria are illustrated in Fig. 6.2.9b. They are limiting the available detection volume to a region in which the fluorescence trigger is saturated even if the energy scale is changed within the systematic uncertainties. The exposure calculation becomes independent of the trigger threshold and of the absolute energy scale within current estimations of its systematic uncertainty.

6.2.3 Atmospheric conditions

As discussed above the precise knowledge and reproduction of the atmospheric parameters during the REALMC simulations is of utmost importance for the determination of the hybrid exposure. In a quasi-automatic mode, laser shots from the CLF are fired into the field of view
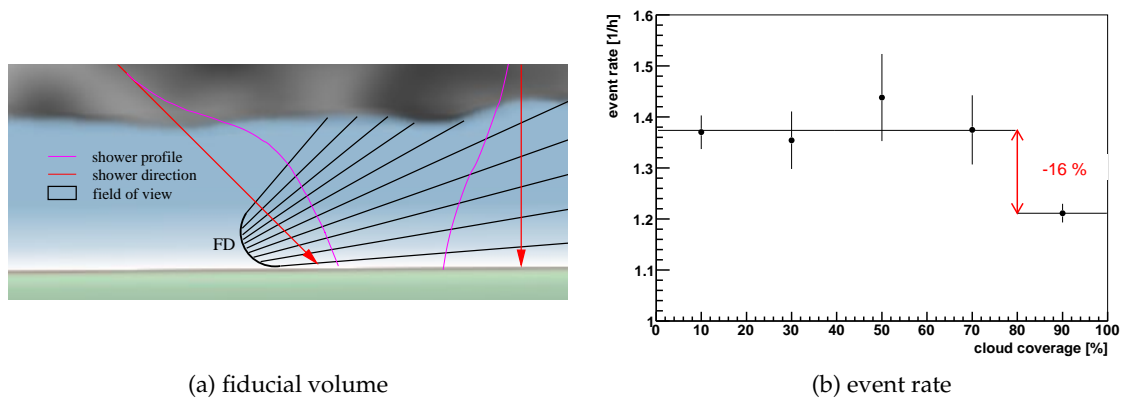
(a) fiducial volume

(b) event rate

Figure 6.2.10: Clouds are limiting the fiducial volume and are affecting air shower detection and reconstruction (left panel, from [170]). The hybrid event rate is significantly reduced during periods with high cloud coverage (right panel).

of the fluorescence detector in regular time intervals during FD data taking. These laser shots are analyzed to determine the light scattering on aerosols. Not the full data taking period is covered by the derived aerosol information. Most of the periods with missing data are related to hardware or software failures but also bad weather conditions could play a role. The analysis of hybrid data and especially the determination of the cosmic ray flux has therefore to be restricted to periods with valid aerosol measurements. This requirement reduces the available data by about 13 %.

It has been realized during this work (see Appendix C.1 and [171]) that clouds above the detector array play an important role for hybrid data analysis. The typical effect of clouds is a disturbance of the longitudinal shower profile. Clouds may obscure parts of the shower evolution causing holes in the reconstructed longitudinal profile. Enhanced light scattering might also lead to the opposite effect and cause spikes in the profile. Both effects are illustrated in Fig. 6.2.10a and visible in the example air shower shown in Fig. C.2.4 in the Appendix. Typically these showers are removed from the dataset by the requirement that the reconstructed profile is in good agreement with a Gaisser-Hillas parameterization as discussed above. In addition, the obscuration of the shower evolution high in the atmosphere is biasing the X_{max} distribution and leads to a modification of the selection efficiency. Both effects are not included in the MC simulation as no analytical model for clouds and their influence on air shower observations is available. Fortunately, a reliable cloud detection is possible based on the data collected by the instruments of the atmospheric monitoring program at the Pierre Auger Observatory. Especially analysis of Lidar scans above the field of view of the fluorescence detector, in order to not disturb the data taking, has been proven to be very useful [171, 172]. Studying the event rate of hybrid events passing all selection criteria mentioned above, a clear dependence on the cloud coverage as determined by Lidar measurements has been found. As shown in Fig. 6.2.10b, the rate is reduced by about 16 %. If the exposure was calculated without detailed cloud analysis, a reduction of the exposure by 16 ± 16 % would have to be applied (e.g. [173]). The related 16 % systematic uncertainty was the main contribution to the systematic uncertainty of the flux measurement. This exposure

Table 6.2.1: Selection efficiencies of the criteria used for the hybrid spectrum event selection.

SELECTION CRITERION	EVENTS	EFFICIENCY [%]
n_{total}	991873	–
commissioned eye	902969	91.0
relative calibration constants	837451	92.7
aerosol measurements	675044	80.6
cloud data	549081	81.3
cloud free period	349761	63.7
no saturated pixels	348499	99.6
hybrid geometry reconstruction	140244	40.2
energy reconstruction	107816	76.9
zenith angle $< 60°$	97955	90.9
$E_{\text{rec}} > 10^{18}\,\text{eV}$	11662	11.9
fraction of Cherenkov light $< 50\,\%$	10818	92.8
X_{max} observed	7526	69.6
Gaisser-Hillas fit $\chi^2/\text{ndof} < 2.5$	7354	97.7
hole in longitudinal profile $< 20\,\%$	6933	94.3
energy reconstruction uncertainty $< 20\,\%$	6651	95.9
fiducial distance	4066	61.1
fiducial FOV	1835	45.1

correction is not necessary if the determination of the hybrid spectrum is restricted to cloud free time periods. As shown in Sec. C.1, they can be identified by Lidar scans with less then 25 % cloud coverage. Restricting the exposure and spectrum determination to these periods, a total of 45 % of the selected events are removed. 17 % have to be removed due to missing Lidar measurements which started routine operation only in 11/2005 and additional 28 % due to detected clouds. The reduction of the systematic uncertainty by 16 % and the related increase in the reliability of the flux determination is clearly justifying this approach.

A summary of the developed selection criteria that are used to select events for the measurement of the energy spectrum are given in Tab. 6.2.1 together with the relative efficiencies.

6.3 The hybrid exposure

The exposure, after applying all quality and fiducial volume criteria, is shown in Fig. 6.3.11 in comparison with other air shower experiments. Although the accumulated exposure and event statistics available for the determination of the energy spectrum is limited by the very strong quality and fiducial volume restrictions it is already compatible with forerunner experiments.

As has been shown in Sec. 5.1.5, different hadronic interaction models are predicting different invisible energy fractions. With more or less energy transfered into visible light, the exposure might be systematically influenced by the chosen interaction model. In addition, different X_{max} predictions might influence the event selection probability and lead to an
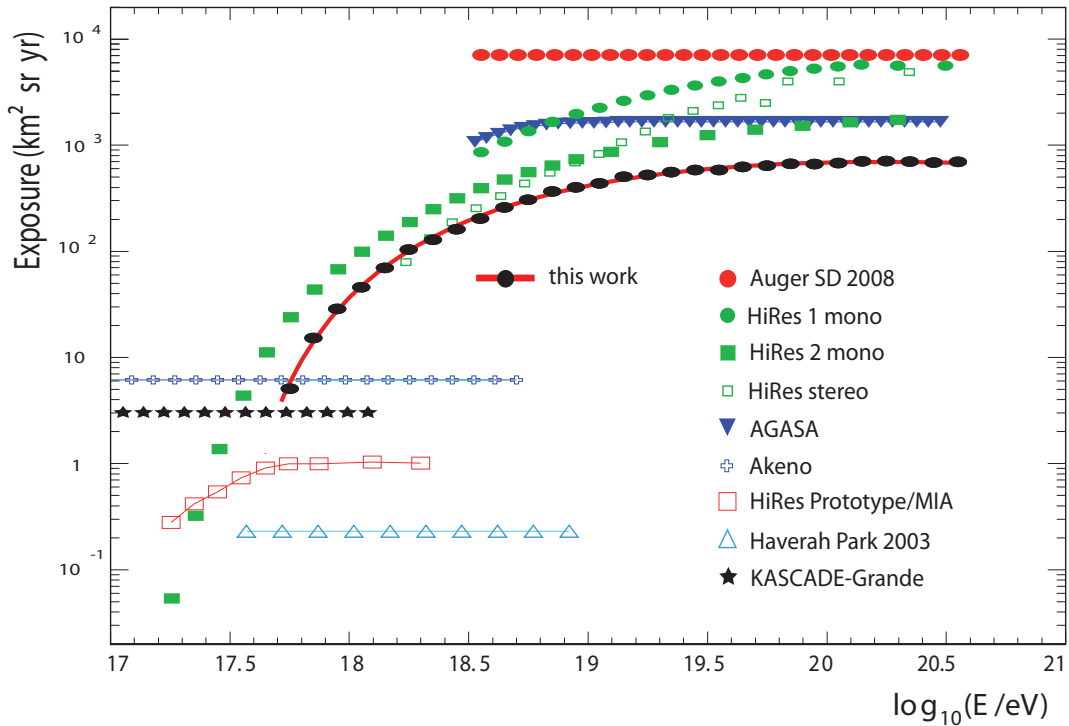
Figure 6.3.11: The final exposure of hybrid air shower detections with the Pierre Auger Observatory derived in this work after all event selection criteria compared to different experiments (modified from [68]).

increasing model dependence. In order to study these effects, two models, QGSJETII-03 and SIBYLL 2.1, have been used as input for the REALMC simulations. As can be seen in Fig. 6.3.12, the derived exposures are in very good agreement. To further reduce the model dependence and the statistical uncertainty of the exposure both MC sets are averaged and used for the exposure determination.

6.4   Validation with surface detector data

The design of the Pierre Auger Observatory with its two complementary air shower detection techniques offers the chance to validate the developed REALMC scheme and the derived hybrid exposure. A dedicated study [170] is comparing the event selection efficiency of hybrid data with predictions from surface array data used as input of REALMC simulations. For showers found in the SD data set, the FD detection probability is calculated with simulations and compared to the number of actually recorded shower images.

The surface array trigger is 100 % efficient above $10^{18.5}$ eV and zenith angles $< 60°$. Events have been selected following these requirements. They also have to fulfill a basic quality criterion called $T5$ which assures a valid reconstruction. Based on the reconstruction, showers with $\cos\theta_{SD} > 0.9$ are discarded from this analysis as they might have their shower maximum below the ground level.

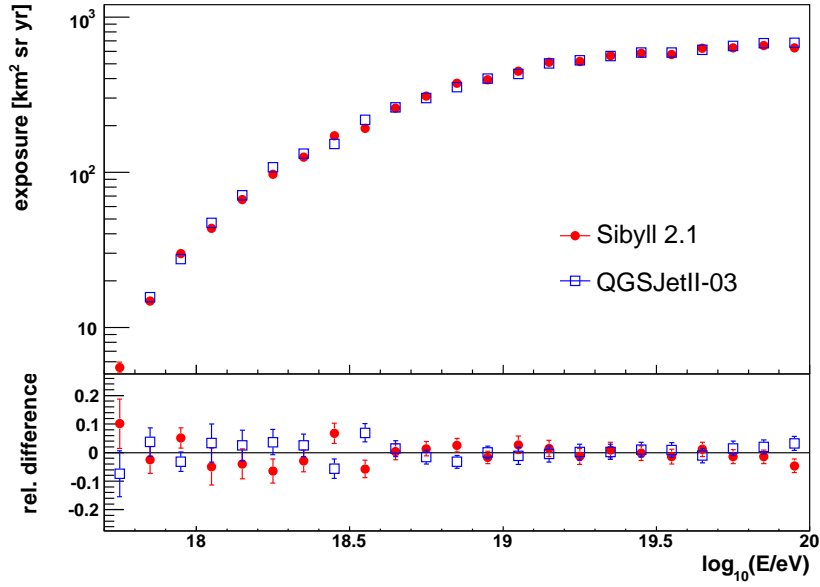For each selected surface event 20 CONEX showers have been simulated. The primary

Figure 6.3.12: The final exposure after all event selection criteria is not depending on the used hadronic interaction model.

energy and shower geometry are chosen according to the reconstruction result of the surface detector event reconstruction. A two component (proton and iron) interpretation of the elongation rate measurement [55] has been used to select the primary mass of these showers. By combining proton and iron simulations in relative fractions reproducing the measured $\langle X_{\mathrm{max}} \rangle$ as function of the energy, a mass composition bias can be avoided. The simulated shower profiles are passed to a full REALMC simulation of the detector response and all quality and fiducial volume cuts discussed above are applied. The combined trigger and selection efficiency of the fluorescence detector can be calculated for each selected surface array event simply as ratio between the N_{sel} selected and the $N_{\mathrm{sim}} = 20$ simulated showers:

$$\varepsilon_{\mathrm{MC}}(FD|MC) = \frac{N_{\mathrm{sel}}(E)}{N_{\mathrm{sim}}(E)} \tag{6.4.12}$$

In addition, the usual hybrid event data stream is used to derive the same efficiency for real data. The available fluorescence data in time-coincidence with the selected surface detector events is passed through the same quality and fiducial volume selection and the probability to find a fluorescence event passing the cuts is given by:

$$\varepsilon_{\mathrm{SD}}(FD|SD) = \frac{N_{\mathrm{sel}}(E)}{N_{\mathrm{SD}}(E)} \ . \tag{6.4.13}$$

As shown in Fig. 6.4.13, both efficiencies agree very well. The statistical uncertainty of the agreement is 5.4 % and can be used to set the upper limit of the overall systematic uncertainty of the hybrid exposure and the hybrid spectrum developed during this work. Additional cross-checks will be discussed in Sec. 7.2.2.
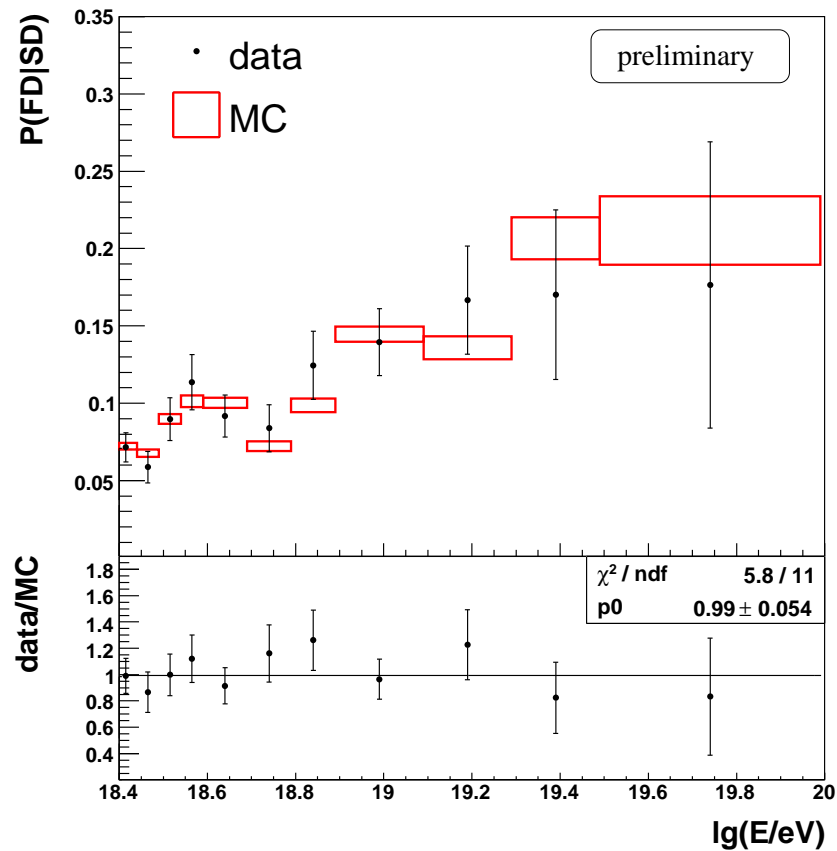
Figure 6.4.13: Events recorded by the surface detector allow for a consistency check of the REALMC simulation and event selection chain (upper panel). The uncertainty of the agreement, which is currently dominated by statistics, can be used as upper limit of the systematic uncertainty of the hybrid exposure and spectrum (lower panel, plot from [138]).

Chapter 7

The UHECR energy spectrum

The flux of cosmic rays J as a function of energy can be written following Eq. (2.2.9) as

$$J(E) = \frac{1}{\Delta E} \frac{N^D(E)}{\mathcal{E}(E)} \, ,$$

(7.0.1)

where $N^D(E)$ is the number of selected data events in the energy bin centered around E and with a width of ΔE. The energy dependent exposure determined with MC simulations as discussed above is denoted by $\mathcal{E}(E)$.

7.1 Hybrid spectrum

After applying all quality and fiducial volume cuts discussed in Sec. 6.2, the hybrid event distribution as function of energy, $N^D(E)$, is obtained. This distribution is shown in Fig. 7.1.1.

Following Eq. (7.0.1), the hybrid spectrum is derived by dividing this distribution by the exposure shown in Fig. 7.1.2. The exposure is calculated as function of the reconstructed energy of the simulated air showers to avoid a bias due to the finite energy resolution of the events. Details about this effect are discussed below (cf. Sec. 7.2).

The derived energy spectrum is given in Fig. 7.1.3 as

$$\frac{dN}{d\ln E} \propto E \cdot J(E) \, .$$

(7.1.2)

The error bars include both the statistical uncertainties of the data (68 % C.L. [174]) and the statistical uncertainty of the MC used to determine the exposure. The visibility of spectral features can be enhanced by rescaling the spectrum. An example is given in Fig. 7.1.4, where a scaling with E^3 has been performed. Clearly visible are deviations from the pure power-law behavior. The measured characteristics of the ankle and possible interpretations of the spectral shape will be given below in Sec. 7.3.
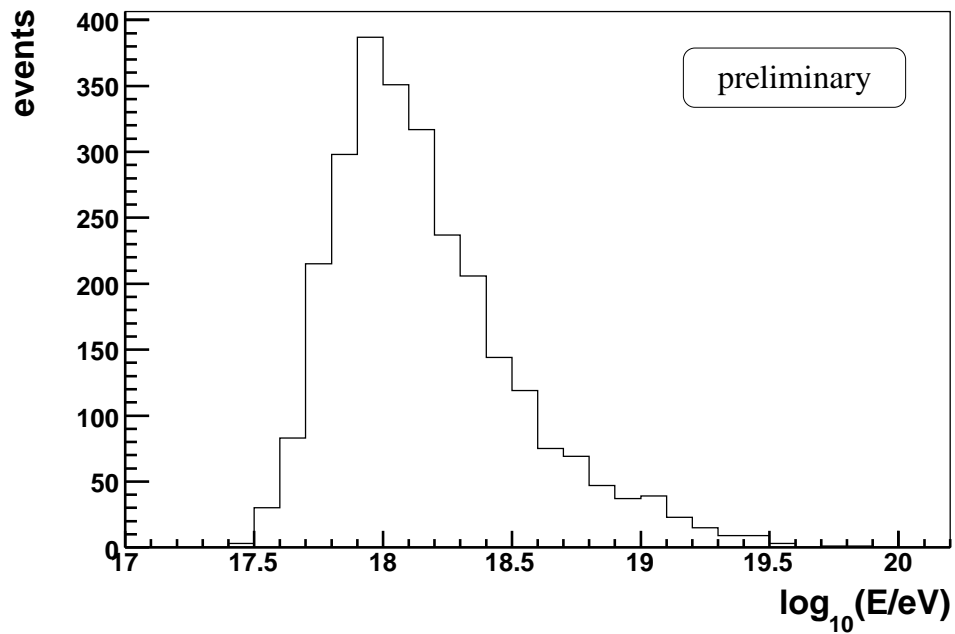
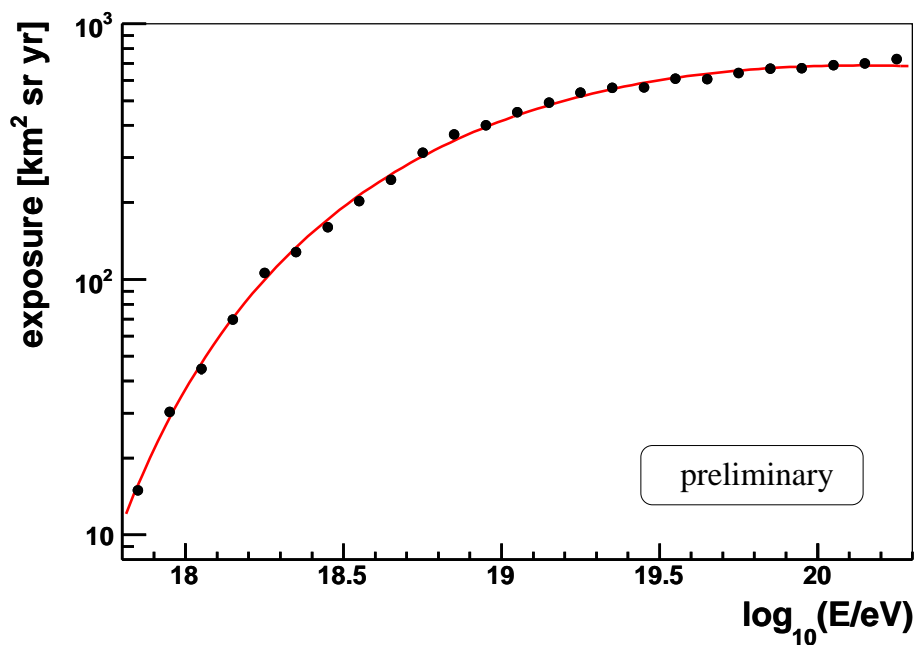Figure 7.1.1: Hybrid events selected for the determination of the energy spectrum.

Figure 7.1.2: The hybrid exposure after all quality and fiducial volume criteria. The statistical uncertainties are smaller than the symbol size. The curve is a fit to guide the eye.
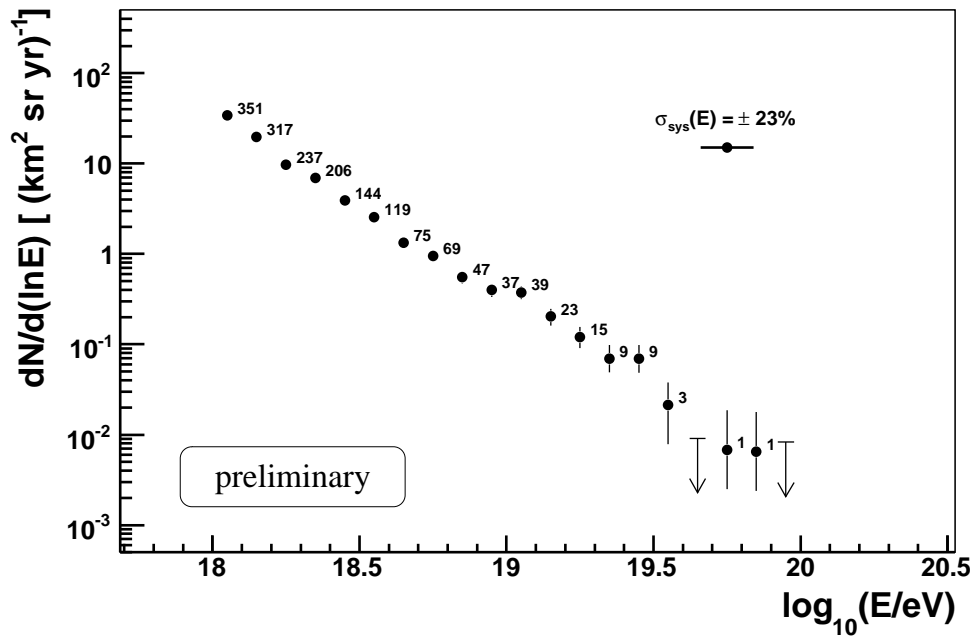
Figure 7.1.3: The energy spectrum of UHECR derived from hybrid data of the Pierre Auger Observatory taken during the period 11/2005 - 05/2008.
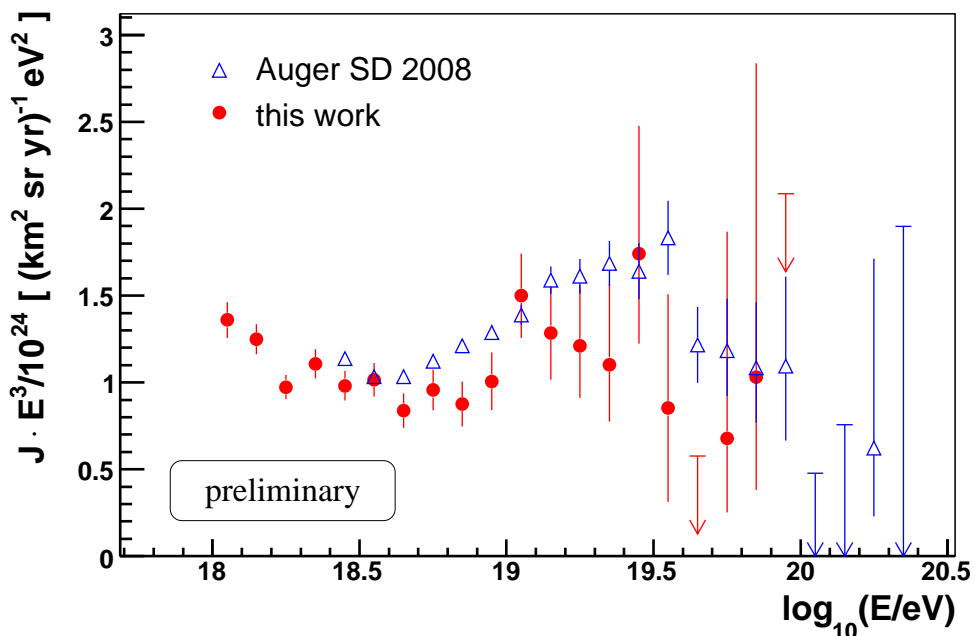

Figure 7.1.4: The hybrid spectrum derived in this work together with the spectrum measured with the surface detector of the Pierre Auger Observatory [67]. The visibility of spectral features is enhanced by multiplying the UHECR flux with E^3.

(a) simulated vs reconstructed events

(b) flux bias due to energy resolution
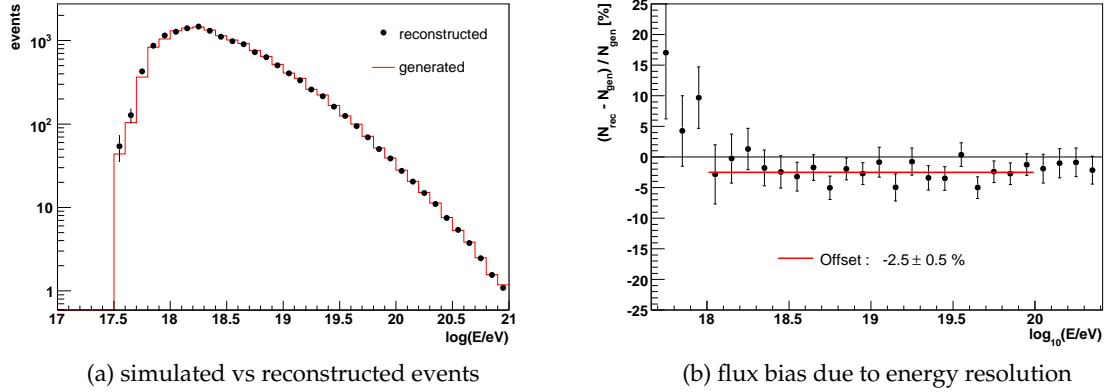
Figure 7.2.5: The finite resolution of the detector and the event reconstruction introduces a small bias in the reconstruction of a steeply falling energy spectrum (here $\phi \propto E^{-3}$). The bias can be removed by using a bin-by-bin unfolding for the determination of the spectrum.

(a) spectrum

(b) difference
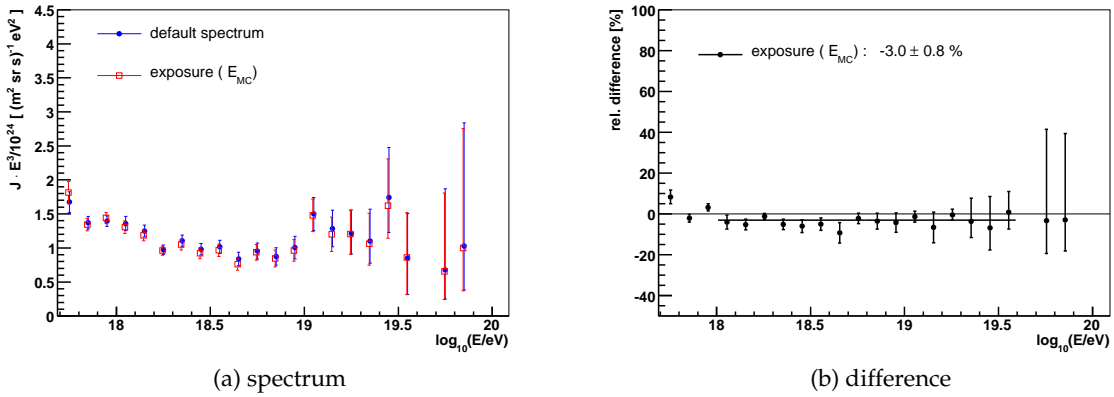
Figure 7.2.6: A small bias due to the finite energy resolution has been removed by a bin-by-bin unfolding of the exposure. The uncorrected spectrum is shifted by about 3 %.

7.2 Systematic uncertainties and cross checks

Possible systematic uncertainties may arise from different aspects of the spectrum determination. In previous works (e.g. [175]) the most problematic uncertainty was related to the uncertainties in the hadronic interaction models and the primary mass composition. It has been shown in Sec. 6.2.2 and 6.3 that these uncertainties could be removed with dedicated event selection criteria in this work.

All energy spectrum determinations suffer from the intrinsic uncertainty due to the finite energy resolution of the detector. The very strong quality requirements applied for the selection of events, reduced the energy reconstruction uncertainty significantly. As illustrated in Fig. 6.2.7, the obtained resolution is better than 10 % and almost independent of the energy. The distributions for different energy bins are given in the Appendix Sec. D.3. As illustrated in these plots, the energy uncertainty is reasonably well described by Gaussian distributions. The influence of a Gaussian resolution σ_E on a cosmic ray flux ϕ, which follows a power law

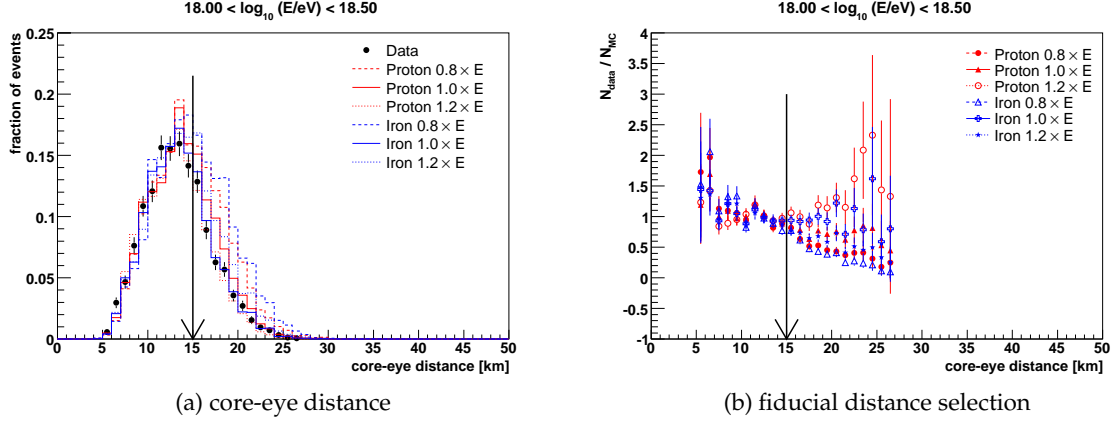(a) core-eye distance

(b) fiducial distance selection

Figure 7.2.7: The distribution of selected air showers with respect to the detector is depending on the absolute energy scale of the event reconstruction and the primary mass (left panel). Selecting events within the fiducial distance range, this dependence is removed, i.e. data and MC agree (right panel).

with index γ can be approximated analytically by [176]

$$\phi \quad = \quad A \cdot E^{-\gamma} \tag{7.2.3}$$

$$\rightarrow \quad \hat{\phi} \quad = \quad A \cdot E^{-\gamma} \left(1 + \gamma(\gamma - 1) \frac{\sigma_E^2}{2E^2} + \dots \right). \tag{7.2.4}$$

With $\sigma_E = 10\,\%$ and $\gamma = 3$, one obtains a flux bias of about $\Delta\phi \approx 3\,\%$. This approximation has been verified using REALMC simulations. As shown in Fig. 7.2.5, the average shift between the event distribution derived from an input spectrum following a power-law flux with $\gamma = 3$ and the distribution of reconstructed events is in very good agreement to the analytical approximation ($\Delta\phi \approx 2.5\,\%$). The bias can be removed by using a bin-by-bin unfolding for the determination of the spectrum, i.e. calculating the exposure as function of the reconstructed instead of the true MC energy. The MC simulations have been weighted to follow the spectral shape defined in Eq. (6.2.8) for this purpose. The difference with respect to a spectrum derived without this procedure, i.e. using the simulated energy, is shown in Fig. 7.2.6.

7.2.1 Energy scale

The developed set of fiducial distance criteria is limiting the exposure calculation to a volume in which the fluorescence detector is $100\,\%$ efficient. The exposure becomes independent of trigger threshold details and is insensitive to a possible change of the absolute energy scale. This important feature can be verified with the help of dedicated REALMC simulations and real hybrid data. Fig. 7.2.7a shows the shower-detector distance distribution of real hybrid events passing all quality and the mass composition field of view cuts (Eq. (6.2.9)) in comparison to REALMC simulations. The distribution is depending on the mass of the primary particle. As iron initiated air showers have a higher invisible energy fraction, i.e. they emit less light and are visible only up to a smaller distance. In addition, a possible energy mis-assignment is causing a similar effect. Both effects are illustrated in Fig. 7.2.7a. Corresponding distribution for the other energy intervals can be found in the Appendix Sec. D.2. The

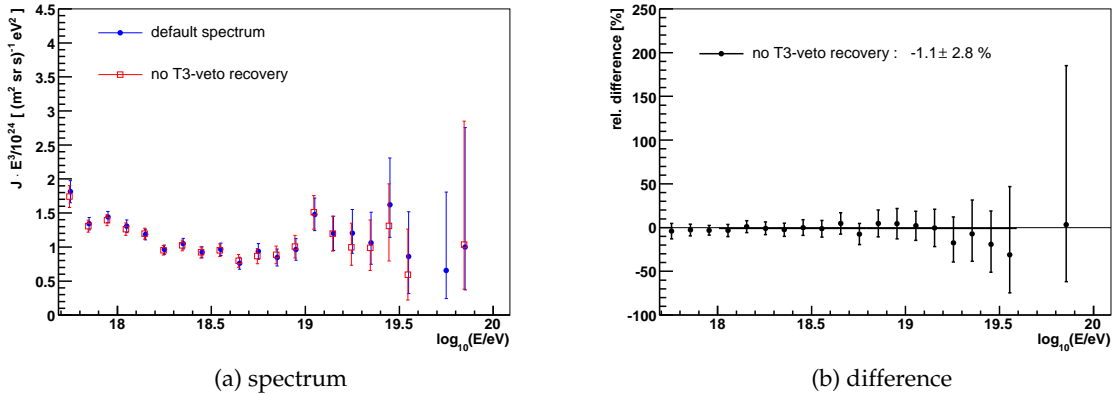(a) spectrum   (b) difference

Figure 7.2.8: The hybrid spectrum is independent of the treatment of the event loss due to the CDAS protection T3 veto and the recovery by the independent trigger of the surface array.

agreement between data and MC is verified by comparing the ratio between data and MC as function of the core-eye distance with the expected value of $N_{\text{data}}/N_{\text{MC}} = 1$. As can be seen in Fig. 7.2.7b, good agreement is found within the fiducial distance defined by Eq. (6.2.11). As the applied fiducial distance cuts are defining a volume in which data and MC agree, even after a modification of the energy scale within current systematic uncertainties, the related systematic effect on the hybrid spectrum is removed. It can be noted, that this comparison between data and MC favors an increase of the energy assignment of about $10 - 20\,\%$, which is in agreement with earlier estimations [177, 178].

7.2.2   Subsample analysis and cross-checks

The overall systematic uncertainty has been derived from cosmic ray data itself. As discussed in Sec. 6.4, based on data recorded by the surface array of the Pierre Auger Observatory, a total systematic uncertainty of less than $6\,\%$ could be deduced. Most aspects of the hybrid spectrum determination are covered by this study. An additional verification of the spectrum determination and its consistency is possible by comparison of spectra from various subsamples. It should be noted that these cross-checks are only able to check for deviations from the expected behavior, i.e. one checks the assumption that the derived spectrum is not dependent on the variable chosen to divide the dataset. The performed tests cannot be used directly to derive the total systematic uncertainty as double counting of statistical fluctuations would be unavoidable [179].

A first cross-check consists of calculating the hybrid exposure without the recovery of events that were rejected by CDAS veto algorithms (cf. Sec. 4.1.3 and Sec. 6.1). Based on the CDAS logfiles only events for which the surface array readout was triggered by a T3 trigger from the fluorescence detector are selected. Events that were rejected by the T3-veto algorithms but recovered by the surface array trigger are not used. The exposure is calculated based on the full T3 veto derived following Eq. (4.1.4). This cross-check is sensitive to problems of the T3-veto determination itself but it is also important because it has been realized, that currently available hadronic interaction models are not able to reproduce some of the details of observed air showers [177]. Especially the muon content of air showers seems to be

(a) spectrum

(b) difference
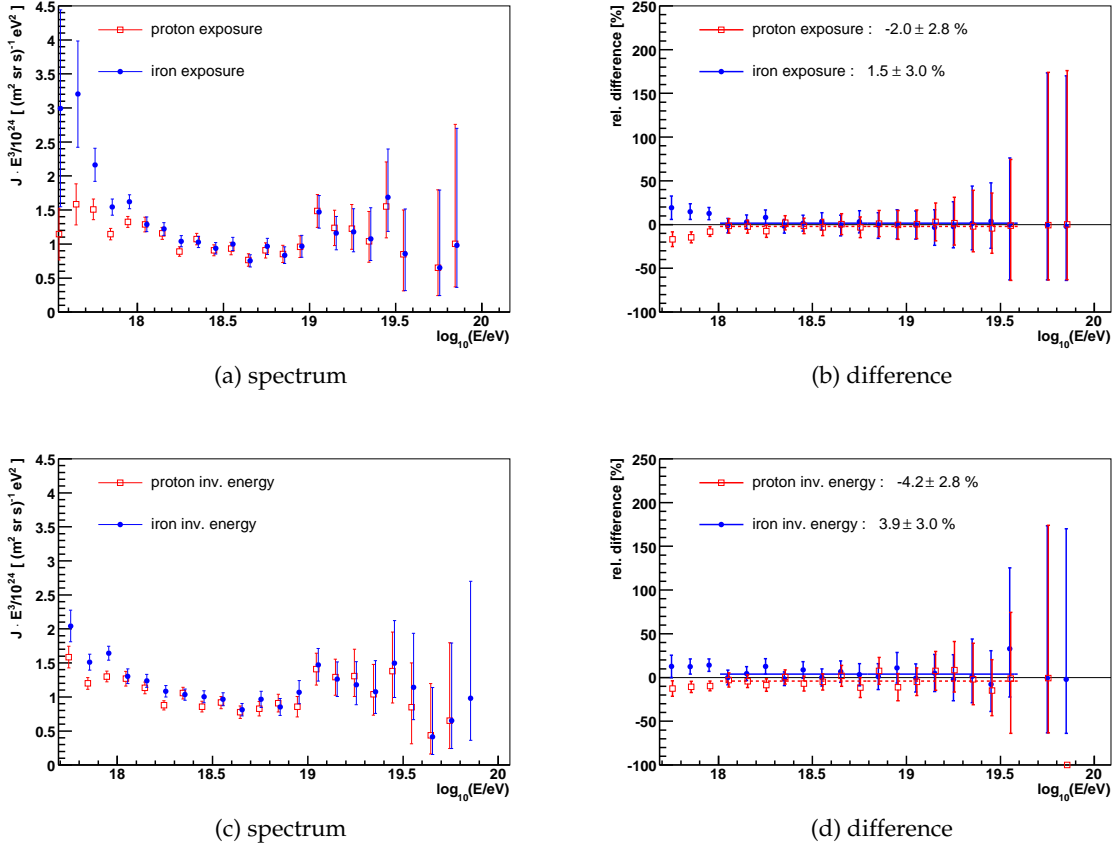

(c) spectrum

(d) difference

Figure 7.2.9: The derived hybrid spectrum is independent of the assumed mass of the primary particles (top panel). Reconstruction of the measured data based on different invisible energy correction factors introduces an overall shift (lower panel). This shift is already taken into account in the systematic uncertainty of the energy scale.

underestimated. This would lead to an underestimation of the trigger efficiency in the MC simulations and is therefore influencing the estimation of the T3-veto recovery efficiency. In addition, also the unknown primary mass composition is influencing the trigger efficiency of the surface detector at energies below the 100 % threshold. A mixed proton and iron is assumed here. As shown in Fig. 7.2.8, no statistically significant difference between the two spectra is found.

It could be shown in Sec. 6.2.2 that the derived exposure is independent of the mass of the primary particles. Nevertheless, the same independence has to be verified for the final hybrid spectrum. The spectra derived by calculating the exposure only with proton or iron induced showers is shown in Fig. 7.2.9a.

The hybrid spectrum presented here is based on the official event reconstruction of the Pierre Auger Observatory (details are given in the Appendix Sec. B). A mixed primary mass composition of 50 % proton and 50 % iron is assumed for the invisible energy correction. This correction is energy dependent as discussed in Sec. 5.1.5 and a modification of the spectral features might be introduced. The overall energy shift is already included in the systematic energy uncertainty and would naturally lead to a shift of the exposure. In order to esti-
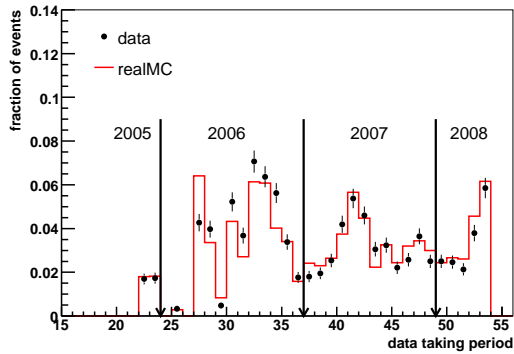
Figure 7.2.10: The time evolution of the event rate is reproduced well with REALMC simulations and no clear time dependent modification is found.
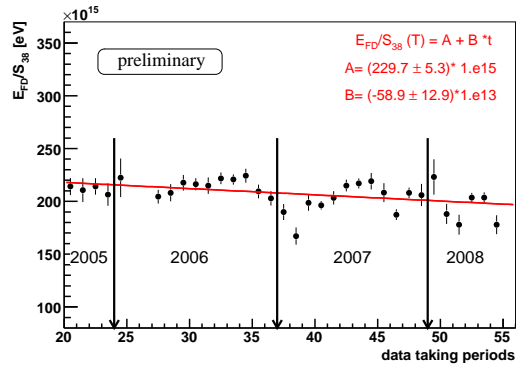

Figure 7.2.11: The time evolution of the ratio of the energy determined by the fluorescence detector and the corresponding surface detector parameter S_{38} hints to a decrease in the energy assignment.

mate the maximum effect of the primary mass assumption on the hybrid spectrum, a full re-reconstruction of the data set with the proton (iron) invisible energy correction has been performed. As shown in Fig. 7.2.9c, the spectral shape is stable and only the expected overall flux bias is found.

Effects directly related to the detector hardware are studied by calculating independent spectra for all available fluorescence detector stations. As shown in Fig. 7.2.12a, no significant difference is found. Another hardware related effect is concerning the surface detector. It has been realized that PMTs in some of the deployed detector stations show unusual behavior which might influence the trigger efficiency. This effect can be excluded by dividing the surface array in a *bad array* of stations showing the unusual behavior and a *good array* without these problems. The data set is then subdivided based on the classification of the station used for the hybrid geometry determination into two groups. As can be seen in Fig. 7.2.12c, no significant difference between the two spectra is found.

As shown in Fig. 7.2.12e, the same agreement is found for spectra of different zenith angle ranges. Comparing the energy spectrum derived from data with zenith angles $< 40°$ and inclined showers with zenith angles between $40°$ and $60°$ no systematic effect is found.

As depicted in Fig. 7.2.13c, a statistically significant difference is found if the data is subdivided into different time periods. Seasonal effects can not account for this difference (cf. Fig. 7.2.13a). If the observed difference was related to the trigger or event selection efficiency it should be reflected in the time evolution of the number of selected events, which is shown in Fig. 7.2.10. Only a small deviation between data and MC is visible in 2006. No modification of the hardware or software configuration, which could explain this difference, is currently known. The most likely source of the time dependence of the energy spectrum is a time dependence of the energy assignment. Thanks to the independent measurement of the surface array, this effect can be investigated by comparing the energy derived from fluorescence measurements with the variable used for the energy reconstruction of surface events (S_{38}, for details see [180]). This comparison is performed on an event-by-event basis by selecting events that have both a valid SD reconstruction and fulfill strict hybrid quality

criteria. In addition to the expected seasonal variation introduced by the temperature dependence of the surface detector signal [181], a significant trend is visible in Fig. 7.2.11. Based on the assumption that the signal derived from the surface detector is stable over time scales longer than one year, a significant decline of the energy reconstructed from the fluorescence measurements is observed. Possible explanations are an underestimation of the PMT aging effect discussed in Sec. 3.2 during the derivation of the calibration constants or an underestimation of the aerosol content of the atmosphere, which might be due to not taking this aging effect into account in the aerosol analysis. Recent investigations on the effect of dust on the UV-filters and mirrors of the fluorescence system have also pointed to a similar effect on the reconstructed energy [134]. As demonstrated in Fig. 7.2.13f, the energy shift needed to account for the observed flux difference (-2% for 2006 and $+6\%$ for 2008) is well within the systematic uncertainties given in Table 3.2.5. Further investigations are ongoing within the Pierre Auger Collaboration.

(a) fluorescence detector station

(b) difference

(c) surface array
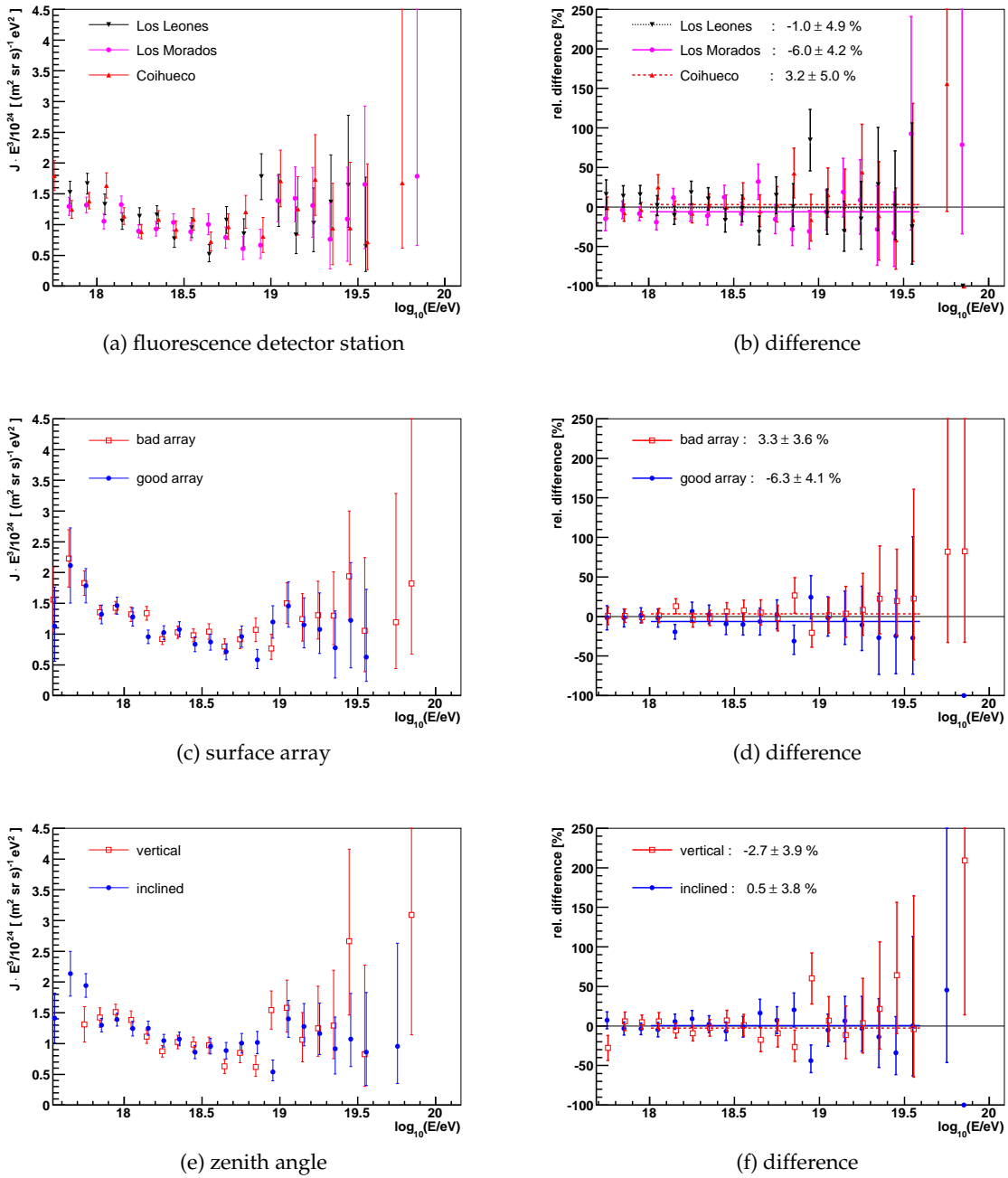
(d) difference

(e) zenith angle

(f) difference

Figure 7.2.12: The determined energy spectrum is independent of the detector hardware, i.e. different fluorescence detectors (top panel) and different areas of the surface detector (middle panel). The spectrum does not depend on the zenith angle range (lower panel).
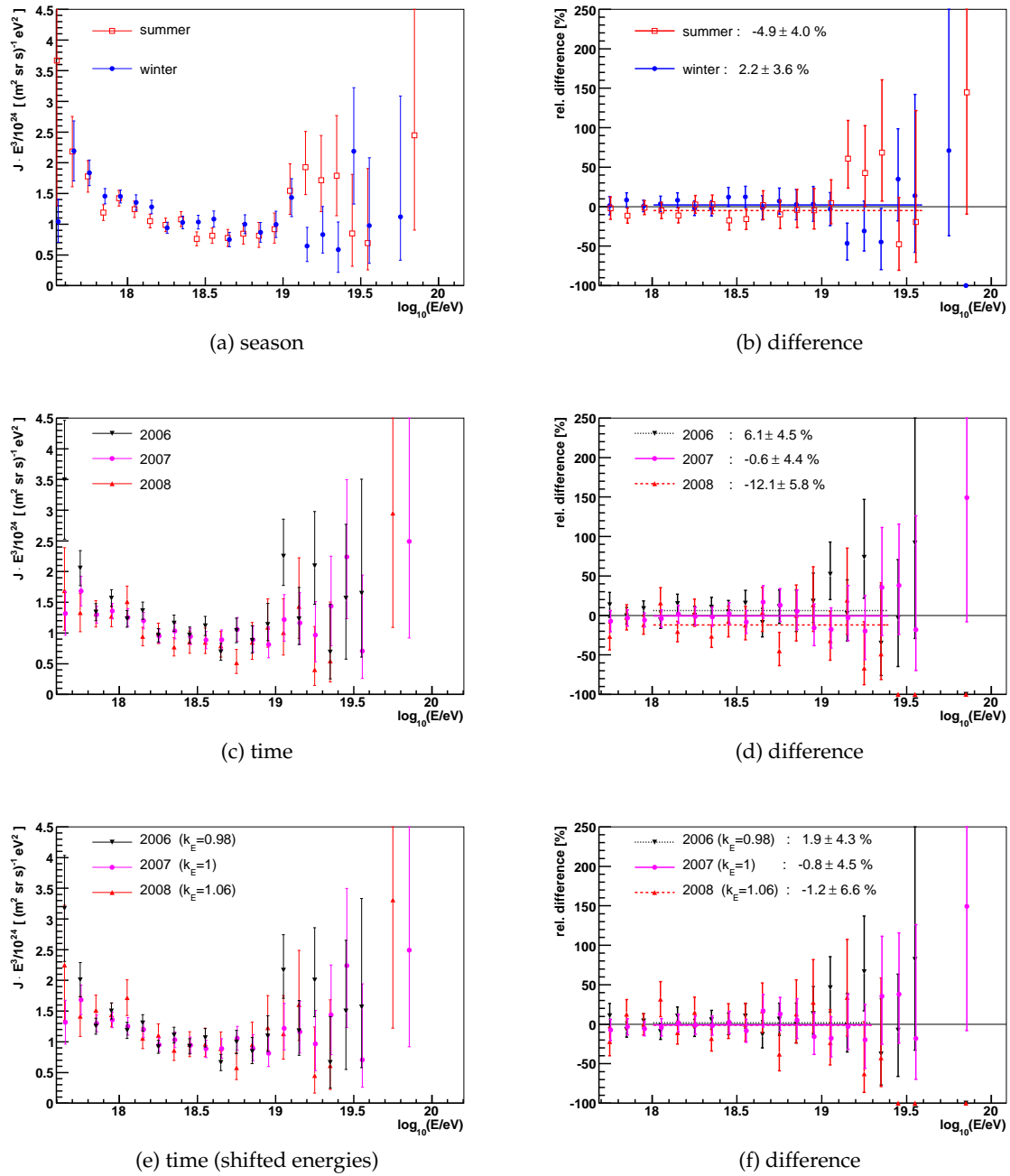
(a) season

(b) difference

(c) time

(d) difference

(e) time (shifted energies)

(f) difference

Figure 7.2.13: The determined energy spectrum is independent of seasonal effects (top panel). The time dependence (middle panel) can be explained by a shift of the energy assignment (lower panel).
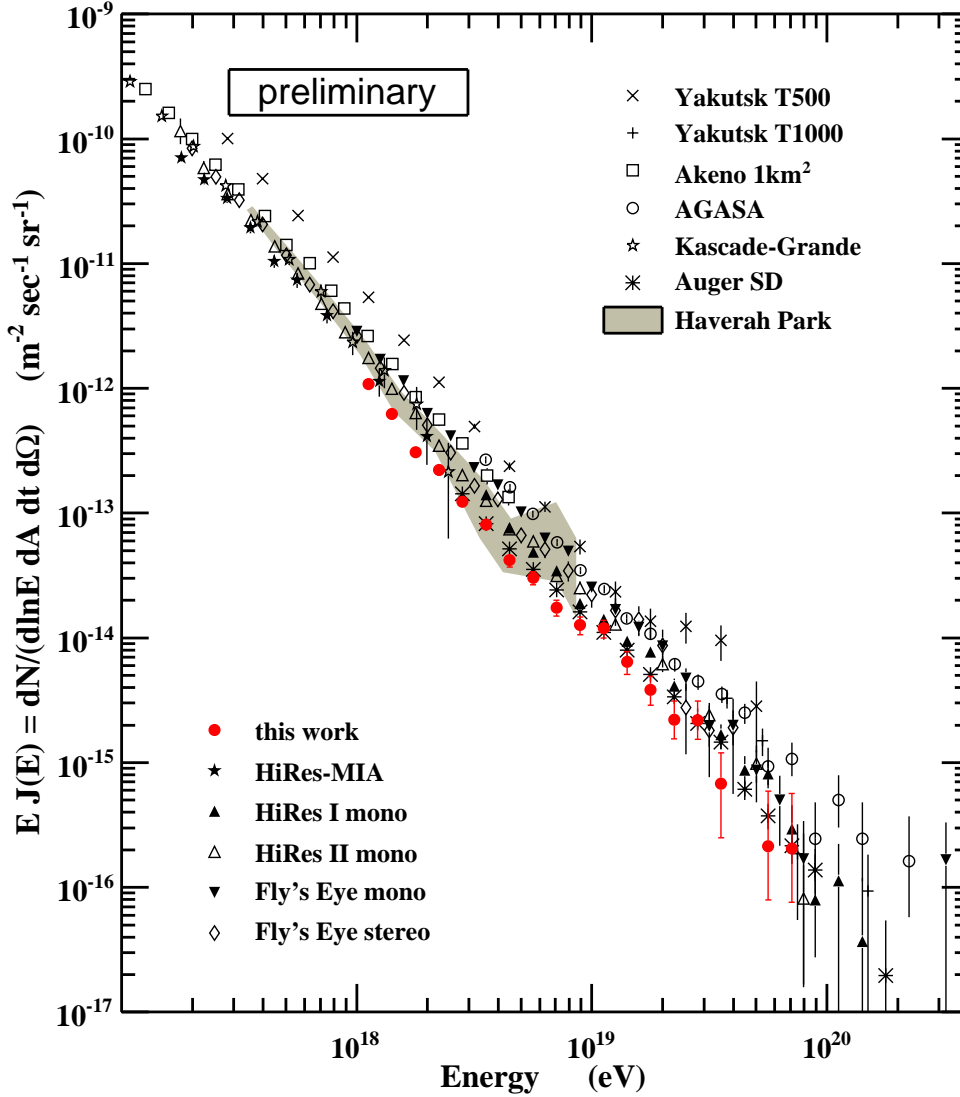
Figure 7.3.14: The flux of cosmic rays determined in this work in comparison to data from Akeno/AGASA [64,65], Fly's Eye [182], Haverah Park [183], HiRes [66], HiRes-MIA [53], KASCADE-Grande [63], Yakutsk [184] and the surface array of the Pierre Auger Observatory [67].

7.3   Spectral analysis and model comparison

The energy spectrum of ultra-high energy cosmic rays determined in this work is shown in Fig. 7.3.14 in comparison with other measurements.

The energy spectrum shows a pronounced break of the spectral index around $10^{18.7}$ eV. A pure power-law behavior between $10^{18} - 10^{19.5}$ eV is disfavored by the data (χ^2/ndof = 26.3/13, $P = 0.02$). A fit with a broken power-law in the same energy range is shown in Fig. 7.3.15. The reduced χ^2/ndof = 10.9/11 ($P = 0.45$) reflects the good description of the data. Although no direct physical interpretation of this simplistic model is possible, it allows
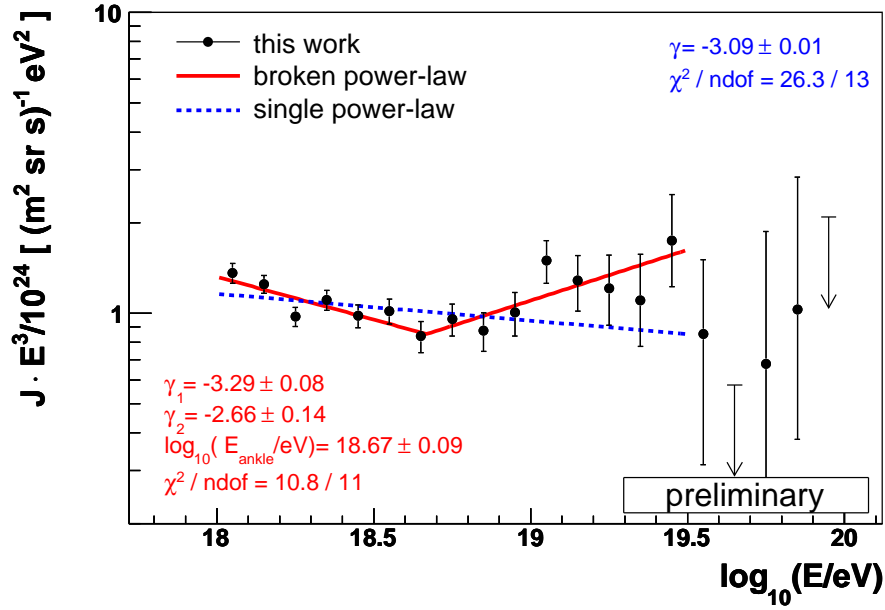
Figure 7.3.15: The determined energy spectrum is well described by a break in the power-law at $10^{18.7}$ eV.

to quantify the characteristic features of the ankle. The ankle is identified simply as the energy at which the spectral index of the power-law spectrum changes. Thanks to the high resolution achieved with the hybrid measurements used for this study, the spectral break could be resolved with unprecedented precision. The following parameters and statistical uncertainties have been derived:

- $E_{\text{ankle}} = 10^{18.67 \pm 0.09}$ eV

- $J \propto E^{-3.29 \pm 0.08}$ $10^{18} < E/\text{eV} \leq 10^{18.67}$

- $J \propto E^{-2.66 \pm 0.14}$ $10^{18.67} < E/\text{eV} < 10^{19.5}$

A more realistic, but still simplistic, model is following the classical description of the ankle as transition between galactic and extragalactic cosmic rays [88, 185, 186]. The total flux can be decomposed into a steeply falling (galactic) component and a (extragalactic) component which is much harder, i.e. less steep. The ankle would be caused by the cross-over between these components. As depicted in Fig. 7.3.16, the agreement with the measured flux is very good ($\chi^2/\text{ndof} = 10.5/12$, $P = 0.57$). In this model the position of the ankle can be defined as the energy where the two components have equal intensity. Naturally this definition will identify the ankle at higher energies compared to the simple description given above. Based on the hybrid energy spectrum $E_{\text{ankle}}(J_{\text{gal}} \equiv J_{\text{egal}}) = 10^{18.8 \pm 0.3}$ eV is found.

Due to the limited statistical power, only hints of the flux suppression at highest energies can be derived from the hybrid spectrum. Its existence has been proven by the HiRes analysis [66] and surface detector data of the Pierre Auger Observatory [67] with high significance.
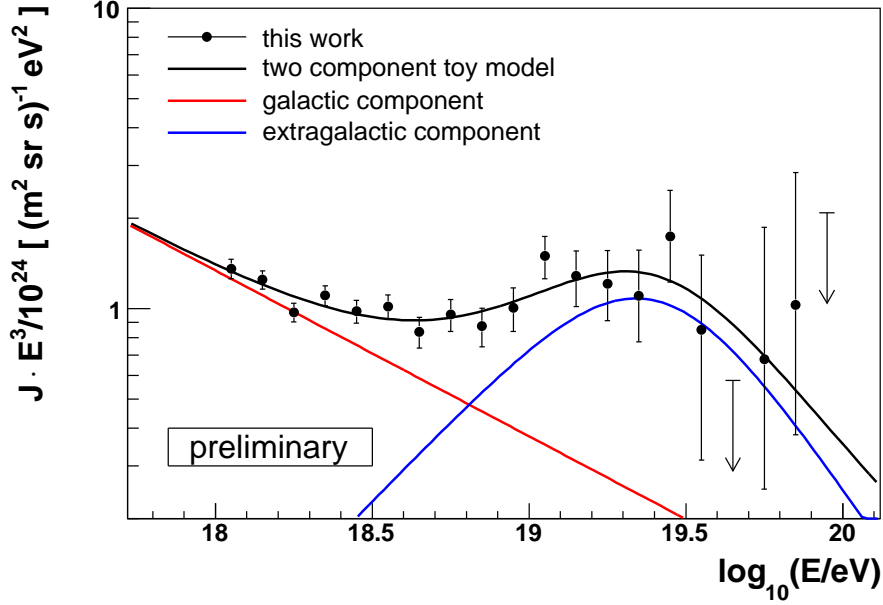
Figure 7.3.16: The classical model, in which the ankle is described as the transition of two flux components is in good agreement with the data.

Fitting the spectrum with the functional form

$$J(E) = A_1 \cdot E^{-\gamma_1} + A_2 \cdot E^{-\gamma_2} \left(1 + \frac{\lg E - \lg E_{\mathrm{cutoff}}}{\lg W_{\mathrm{cutoff}}}\right)^{-1} , \qquad (7.3.5)$$

a suppression setting in at $\lg(E_{\mathrm{cutoff}}/\mathrm{eV}) = 10^{19.4\pm0.4}$ eV can be derived (cf. Fig. 7.3.16). The other relevant parameters have been determined to $\gamma_1 = 3.55 \pm 0.28$, $\gamma_2 = 1.92 \pm 0.42$ and $\lg(W_{\mathrm{cutoff}}/\mathrm{eV}) = 0.17 \pm 0.11$.

Whereas several experiments have observed the ankle in the cosmic ray spectrum, only few estimates of its energy are available in literature [187]. In addition, systematic uncertainties are typically not considered. For comparison the spectra of the experiments with the highest exposures are shown in Fig. 7.3.17.

The derived cosmic ray flux has been compared with the two phenomenological models discussed in Sec. 2.2.3. The first model assumes that the extragalactic sources accelerate only protons [84]. The ankle is interpreted as Bethe-Heitler e^+e^- pair production which causes a dip in the energy spectrum. The spectral shape predicted by this model has been derived from a full MC cosmic ray propagation performed with CRPROPA [188]. Protons are propagated over variable distances, i.e. redshifts. All known energy loss processes are modeled based on realistic assumptions on the intergalactic radiation fields like the cosmic microwave background. The energy distribution of the propagated particles has been used as input to a minimization routine. During the fitting procedure, the normalization of the predicted flux, the source spectrum $\phi_{\mathrm{source}} \propto E^{-\gamma}$ and the source evolution $(z+1)^m$ have been re-weighted. As illustrated in Fig. 7.3.18, a very good description of the measured spectral shape has been found ($\chi^2/\mathrm{ndof} = 14.8/15$, $P = 0.46$). Following the original dip-model, i.e. without constraining the maximum energy of the accelerator(s), the following
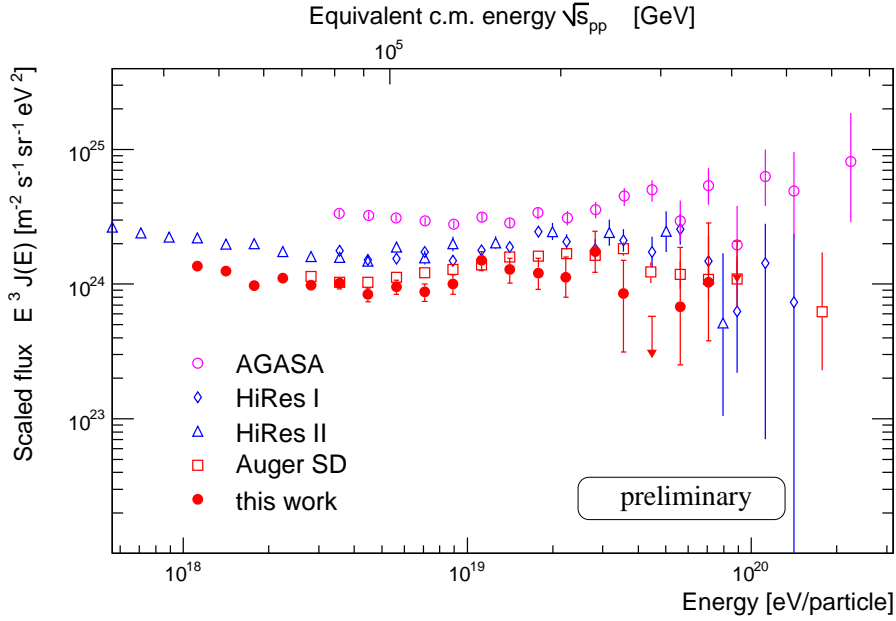
Figure 7.3.17: The hybrid energy spectrum in comparison with other experiments [65–67].

source parameters could be derived:

- source spectrum: $\phi_{\text{source}} \propto E^{-2.43 \pm 0.01}$

- source evolution: $(z + 1)^{2.52 \pm 0.47}$

These values are in perfect agreement with parameters derived by comparison with other measurements (see for example [84, 85, 189]). Although the sensitivity to derive the source evolution is limited, the derived value seems in agreement with astrophysical observations, for example, of the evolution of quasi stellar objects (quasars), which are considered as possible UHECR acceleration sites [60]. It should be noted that the dip-model with its pure proton composition is not favored by the mass composition data derived with the Pierre Auger Observatory [55]. As discussed in Sec. 2.2.2, the interpretation of the measured elongation rate, i.e. $\langle X_{\text{max}} \rangle (E)$, in terms of primary mass is strongly dependent on the modeling of the hadronic interactions at ultra-high energies. This intrinsic systematic uncertainty prevents currently the exclusion of the proton hypothesis. These ambiguities will be partially resolved by the analysis of the mass sensitive and less model dependent X_{max} fluctuations in the near future.

The dependence on the hadronic interaction models is also the limiting factor for the comparison with the second UHECR model. Following the analysis by [83, 85], the extragalactic sources are assumed to accelerate a mixed composition with nuclear abundances similar to those found in low energy, i.e. presumably galactic, cosmic rays. Sources are distributed uniformly and are assumed to have a maximum energy modeled with a simple exponential cutoff at an energy E_{max}. The acceleration process itself is assumed to be rigidity-dependent, i.e. a nucleus of charge Z can reach a maximum energy Z times higher than that
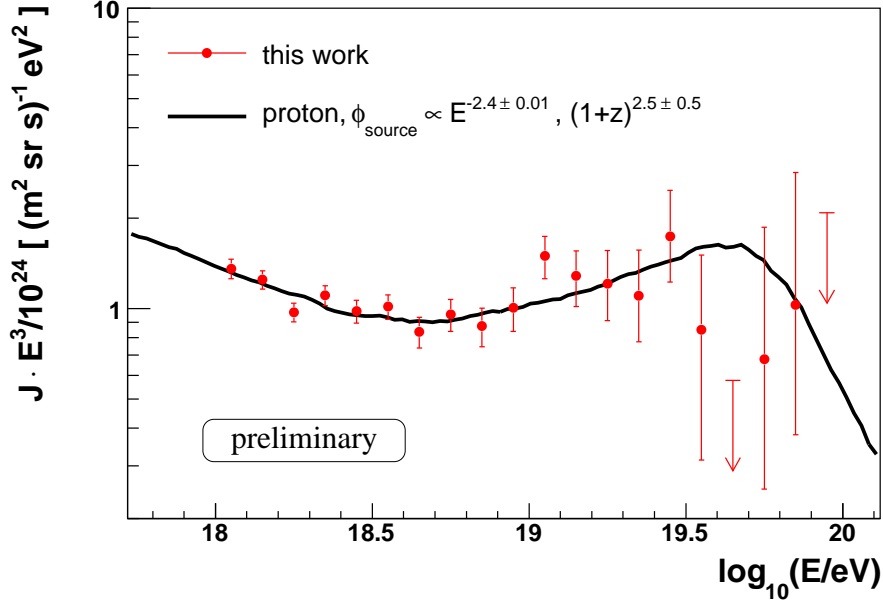
Figure 7.3.18: The hybrid spectrum compared to a model assuming extra-galactic sources with a pure proton composition derived from a full propagation MC [188]. The agreement is very good ($\chi^2/\text{ndof} = 14.8/15$, $P = 0.46$).

of protons: $E_{max}(Z) = ZE_{max}(p)$. The nuclei are propagated through the intergalactic radiation fields, where, in addition to energy losses via e^+e^- pair production of protons, different processes of nuclei photo-erosion are taken into account in a full MC approach. The energy spectrum after the propagation can then be compared to the measured flux. The model describes only the extragalactic part of the energy spectrum. The fitting range has to be restricted to energies above the ankle as the lower part of the spectrum is assumed to be of galactic origin. At the same time, the predicted relative abundances of the different nuclei arriving at Earth can be used in conjuction with a hadronic interaction model to derive a prediction for the elongation rate, i.e. the evolution $\langle X_{\max} \rangle$ as function of energy. Based on a full set of model data [190], a combined fit of the spectrum measured in this work and $\langle X_{\max} \rangle$ data [55] has been performed. As can be seen in Fig. 7.3.19, the mixed composition model is in very good agreement with both measurements if the QGSJET01 [191] interaction model is used for the interpretation of the mass composition. The combined fit yields $\chi^2/\text{ndof} = 13.3/13$ ($P = 0.42$) for the following parameters:

- source spectrum: $\phi_{\text{source}} \propto E^{-2.2}$

- maximum energy: $E_{\max} \approx Z \cdot 10^{19.5}$ eV

- negligible source evolution

The systematic differences between different hadronic interaction models translate directly to a large uncertainty of these values. Although the obtained results are similar, the agreement between the model and both the UHECR flux and mass composition is reduced for
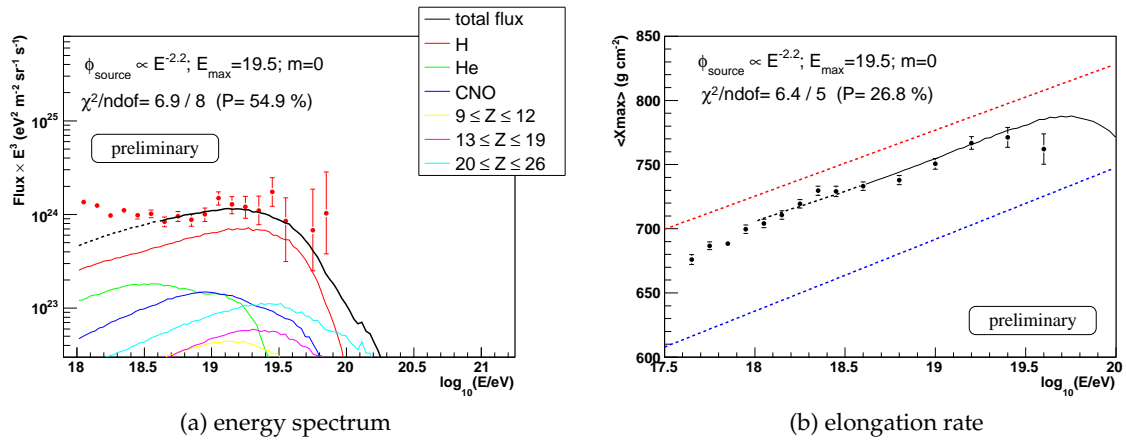
Figure 7.3.19: The 'mixed composition model' [85] assuming extra-galactic sources with a mixed mass composition similar to the galactic abundances is able to explain both the derived energy spectrum and the elongation rate measurements [55] (model data (QGSJet01) from [190]).

other hadronic interaction models. Comparisons based on the QGSJETII-03 and the SIBYLL model are given in the Appendix Sec. E.2.

Although the shape of the spectrum determined in this work can be reproduced equally well by both the proton dip model and the mixed composition model, the latter is clearly favored as it is in much better agreement with mass composition measurements.

Chapter 8

Summary

The energy spectrum of ultra-high energy cosmic rays is one of the most fundamental measurements required for the understanding of the highest energy particles in the universe. Especially the region above 10^{18} eV contains valuable and complementary information about possible sources and the acceleration mechanisms at highest energies. The energy spectrum in this region has been derived in this work from hybrid data of the Pierre Auger Observatory. These measurements use the combined information from fluorescence and surface detectors to obtain optimal accuracy and reliability of the reconstruction of air shower parameters.

Both data reconstruction as well as the determination of the exposure are key elements for the determination of the energy spectrum. An automatic system for the event reconstruction has been set up during this work and tools for data storage and visualizations have been developed. To derive the exposure of hybrid measurements, several novel analyses and techniques have been introduced. The analyzed time period comprises the construction and startup phase of the observatory. During this time the detector configuration changed substantially and failure rates were elevated. To derive the overall time dependent air shower detection efficiency with high accuracy all available monitoring and cosmic ray data have been used. This uptime information accounts for all known inefficiencies at all scales from the single PMT to the full hybrid data taking of the observatory. Among the most important aspects are

- Changes of the hardware configuration and running conditions are taken into account at all scales, from electronics failures to the commissioning of new fluorescence detector stations and surface detectors.

- Based on measured noise levels and using the actual trigger thresholds, the exact trigger conditions are reproduced at the single PMT level. Changes of the trigger thresholds due to moon or starlight are reproduced.

- Measurements of calibration constants performed each night are used to follow modifications of the camera sensitivity.

- The atmospheric conditions, especially the important and very time-variable scattering on aerosols, are reproduced by the use of measured atmospheric properties.

The detailed uptime information is used as basis of a new Monte Carlo simulation technique. In order to model the changing data taking conditions of the hybrid mode of the Pierre Auger Observatory, a time dependent detector Monte Carlo (REALMC) has been developed.

Extensive comparisons between simulated air showers and data showed an excellent agreement at all levels.

The combined systematic uncertainty of the uptime determination and the REALMC simulations could be derived by comparison with independent data from the surface array. A perfect agreement with a statistical uncertainty of less than 6 % has been found.

The exposure of hybrid observations with the Pierre Auger Observatory could be derived from extensive REALMC simulations covering a large parameter space in time, energy, primary mass, event geometry etc. Detailed studies of the reconstruction quality led to the definition of dedicated quality selection criteria. The developed quality cuts assure an unprecedented energy resolution of less than 10 % over the full energy range and all parameter distributions show perfect agreement between data and Monte Carlo.

Comparison of atmospheric monitoring data provided by different laser systems enabled a detailed study on the influence of clouds on hybrid data analysis. Based on this study, the influence of clouds on the energy spectrum could be removed. It could also be shown that the derived exposure is independent of the hadronic interaction model used in the Monte Carlo simulations. The systematic uncertainty of the derived exposure and the energy spectrum is further minimized by the application of dedicated fiducial volume selection criteria.

- Dependences on details of the trigger threshold and on the systematic energy uncertainty are removed by reducing the distance from the fluorescence detector up to which measured air showers are taken into account.

- A set of field-of-view restrictions has been found that achieves an exposure which is independent of the mass of the cosmic primary and removes the systematic uncertainty which was inherent to previous fluorescence based measurements.

Extending the nominal energy range of the Pierre Auger Observatory, the energy spectrum of cosmic rays above 10^{18} eV has been determined. Using hybrid data from the period 11/2005 - 05/2008, the spectrum could be measured with high precision and a systematic uncertainty of the overall flux normalization of 6 %. In the overlap region good agreement with the published spectrum derived from surface detector data of the Pierre Auger Observatory is found. The derived spectrum has been interpreted within different phenomenological models. Although the spectral shape can be explained by both, the 'dip' and the 'mixed composition' models, the latter is clearly favored as a consistent description of the derived spectrum and mass composition data is possible. Systematic uncertainties of hadronic interaction models are currently limiting the accuracy to constrain important model parameters like the source injection spectrum. This dependence will be reduced significantly in the future as soon as an increased event statistics allow for the analysis of additional mass sensitive parameters.

Chapter 9

Acknowledgments

Bibliography

[1] C.D. Anderson. Cosmic-ray negative and positive electrons. *Phys. Rev.*, 43:491–494, 1933.

[2] J. C. Street and E. C. Stevenson. New Evidence for the Existence of a Particle of Mass Intermediate Between the Proton and Electron. *Physical Review*, 52:1003–1004, 1937.

[3] C.M.G. Lattes, H. Muirhead, G.P.S. Occhialini, and C.F. Powell. Processes involving charged mesons. *Nature*, 159:694–697, 1947.

[4] C.M.G. Lattes, G.P.S. Occhialini, and C.F. Powell. Observations on the tracks of slow mesons in photographic emulsions. 1. *Nature*, 160:453–456, 1947.

[5] C.M.G. Lattes, G.P.S. Occhialini, and C.F. Powell. Observations on the tracks of slow mesons in photographic emulsions. 2. *Nature*, 160:486–492, 1947.

[6] J. Abraham et al. (Pierre Auger Collaboration). Properties and performance of the prototype instrument for the Pierre Auger Observatory. *Nucl. Instr. Meth.*, 523:50–95, 2004.

[7] V.F. Hess. Über Beobachtungen der durchdringenden Strahlung bei sieben Freiballon-fahrten. *Phys. Zeits.*, 13:1084–1091, 1912.

[8] B. Rossi. *Ric Sci. Suppl.*, 1:579, 1934.

[9] P. Auger, P. Ehrenfest, R. Maze, J. Daudin, and R. A. Fréon. Extensive Cosmic-Ray Showers. *Review of Modern Physics*, 11:288–291, 1939.

[10] J. Knapp. Corsika School 2005, Lauterbad, http://www-ik.fzk.de/~corsika/corsika-school2005/program.htm.

[11] J.F. Carlson and J.R. Oppenheimer. On Multiplicative Showers. *Physical Review*, 51:220–231, 1937.

[12] W. Heitler. *The Quantum Theory of Radiation*. Oxford University Press, 1954.

[13] R. Ulrich. *Measurement of the Proton-air Cross Section using Hybrid Data of the Pierre Auger Observatory*. PhD thesis, University of Karlsuhe, 2007.

[14] J. Matthews. A Heitler model of extensive air showers. *Astroparticle Physics*, 22:387–397, 2005.

[15] B. K. Lubsandorzhiev. Photodetectors of Lake Baikal Neutrino experiment and TUNKA Air Cherenkov Array. *Nuclear Instruments and Methods in Physics Research A*, 442:368–373, 2000.

[16] Falcke, H. et al. (LOPES Collaboration). Detection and imaging of atmospheric radio flashes from cosmic ray air showers. *Nature*, 435:313–316, 2005.

[17] T. Huege, R. Ulrich, and R. Engel. Monte Carlo simulations of geosynchrotron radio emission from CORSIKA-simulated air showers. *Astroparticle Physics*, 27:392–405, 2007.

[18] A. van den Berg for the Pierre Auger Collaboration. Radio detection of high-energy cosmic rays at the Pierre Auger Observatory. *Proc. 30th Int. Cosmic Ray Conf. (Merida, Mexico)*, 2007. see also arXiv: 0708.1709v1 [astro-ph].

[19] R. Engel. Very High Energy Cosmic Rays and Their Interactions. *Nucl. Phys. B (Proc. Suppl.)*, 151:437–461, 2006.

[20] J. Linsley, L. Scarsi, and B. Rossi. Energy Spectrum and Structure of Large Air Showers. *Journal of the Physical Society of Japan Supplement*, 17:C91, 1962.

[21] T. Hara and others (Akeno Collaboration). The Akeno Air Shower Project. *Proc. 16th Int. Cosmic Ray Conf.*, 8:135–140, 1979.

[22] N. Chiba and others (AGASA Collaboration). Akeno Giant Air Shower Array (AGASA) covering 100 km^2 area. *Nucl. Instr. Meth. A*, 311:338–349, 1992.

[23] M. Fukushima. Telescope Array Project for Extremely High Energy Cosmic Rays. *Progress of Theoretical Physics Supplement*, 151:206–210, 2003.

[24] D. M. Edge et al. The cosmic ray spectrum at energies above 10^{17} eV. *Journal of Physics A (Mathematical General)*, 6:1612–1634, 1973.

[25] T. Antoni et al. (KASCADE Collaboration). The cosmic-ray experiment KASCADE. *Nucl. Instr. Meth. A*, 513:429, 2003.

[26] G. Navarra et al. (KASCADE-Grande Collaboration). KASCADE-Grande: a large acceptance, high-resolution cosmic-ray detector up to 10^{18} eV. *Nucl. Instr. Meth. A*, 518:207–209, 2004.

[27] T. Antoni et al. (KASCADE Collaboration). KASCADE measurements of energy spectra for elemental groups of cosmic rays: Results and open problems. *Astroparticle Physics*, 24:1–2, 2005.

[28] M. Amenomori, et al. (Tibet ASγ Collaboration). The All-Particle Spectrum of Primary Cosmic Rays in the Wide Energy Range from 10^{14} to 10^{17} eV Observed with the Tibet-III Air-Shower Array. *Astrophysical Journal*, 678:1165–1179, 2008.

[29] J. Linsley. Evidence for a Primary Cosmic-Ray Particle with Energy 10^{20} eV. *Phys. Rev. Lett.*, 10:146–148, 1963.

[30] D.J. Bird and others (Fly's Eye Collaboration). Detection of a cosmic ray with measured energy well beyond the expected spectral cutoff due to cosmic microwave radiation. *Astrophysical Journal*, 441:144–150, 1995.

[31] M. Nagano et al. New measurement on photon yields from air and the application to the energy estimation of primary cosmic rays. *Astroparticle Physics*, 22:235–248, 2004.

[32] T. Waldenmaier, J. Blümer, and H. Klages. Spectral resolved measurement of the nitrogen fluorescence emissions in air induced by electrons. *Astroparticle Physics*, 29:205–222, 2008.

[33] M. Ave et al. (Airfly Collaboration). Measurement of the pressure dependence of air fluorescence emission induced by electrons. *Astroparticle Physics*, 28:41–57, 2007.

[34] M. Unger, B. R. Dawson, R. Engel, F. Schüssler, and R. Ulrich. Reconstruction of longitudinal profiles of ultra-high energy cosmic ray showers from fluorescence and Cherenkov light measurements. *Nucl. Instr. Meth. A*, 588:433–441, 2008.

[35] R. M. Baltrusaitis et al. (Fly's Eye Collaboration). The Utah Fly's Eye detector. *Nucl. Instr. Meth. A*, 240:410–428, 1985.

[36] T. Abu-Zayyad and others (HiRes/MIA Collaboration). HiRes/MIA Measurements of EAS Development Between 10^{17} and 10^{18} eV:Detector description and Performance. *Proc. 26th Int. Cosmic Ray Conf. (Salt Lake City, USA)*, 1999.

[37] J. H. Boyer, B. C. Knapp, E. J. Mannel, and M. Seman. FADC-based DAQ for HiRes Fly's Eye. *Nucl. Instr. Meth. A*, 482:457–474, 2002.

[38] P. Sommers. Capabilities of a giant hybrid air shower detector. *Astroparticle Physics*, 3:349–360, 1995.

[39] M. Kachelrieß. Anisotropies and clustering of extragalactic cosmic rays. *Nuclear Physics B (Proceedings Supplements)*, 165:272–279, 2007.

[40] A. Cuoco, G. Miele, and P. D. Serpico. First hints of large scale structures in the ultra-high energy sky? *Phys. Rev. D*, 74:123008, 2006.

[41] G. Sigl, F. Miniati, and T. Ensslin. Ultrahigh energy cosmic rays in a structured and magnetized universe. *Phys. Rev. D*, 68:043002, 2003.

[42] J. Alvarez-Muñiz, R. Engel, and T. Stanev. Ultrahigh-Energy Cosmic-Ray Propagation in the Galaxy: Clustering versus Isotropy. *Astrophysical Journal*, 572:185–201, 2002.

[43] J. Blümer and K.-H. Kampert. Die Suche nach den Quellen der kosmischen Strahlung. *Physikalische Blätter*, 56:39–45, 2000.

[44] K. Dolag, D. Grasso, V. Springel, and I. Tkachev. Constrained simulations of the magnetic field in the local Universe and the propagation of ultrahigh energy cosmic rays. *Journal of Cosmology and Astroparticle Physics*, 1:9, 2005.

[45] S. Lee, A. V. Olinto, and G. Sigl. Extragalactic Magnetic Field and the Highest Energy Cosmic Rays. *Astrophysical Journal*, 455:L21+, 1995.

[46] G. Sigl, F. Miniati, and T. Ensslin. Ultrahigh energy cosmic ray probes of large scale structure and magnetic fields. *Phys. Rev. D*, 70:043007, 2004.

[47] J. Abraham et al. (Pierre Auger Collaboration). Correlation of the Highest-Energy Cosmic Rays with Nearby Extragalactic Objects. *Science*, 318:938–943, 2007.

[48] J. Abraham et al. (Pierre Auger Collaboration). Correlation of the highest-energy cosmic rays with the positions of nearby active galactic nuclei. *Astroparticle Physics*, 29:188–204, 2008.

[49] R. U. Abbasi et al. Search for Correlations between HiRes Stereo Events and Active Galactic Nuclei. *ArXiv e-prints: 0804.0382v1*.

[50] M.-P. Véron-Cetty and P. Véron. A catalogue of quasars and active nuclei: 12th edition. *Astron. Astroph.*, 455:773–777, 2006.

[51] F. Schüssler, J. Blümer, R. Engel, R. Ulrich, M. Unger, D. Veberič. Investigation of AGN correlations with hybrid and stereo FD data. *Auger Technical Note*, GAP-2007-094, 2007.

[52] M. Ave, P. J. Boyle, F. Gahbauer, C. Höppner, J. R. Hörandel, M. Ichimura, D. Müller, and A. Romero-Wolf. Composition of Primary Cosmic-Ray Nuclei at High Energies. *Astrophysical Journal*, 678:262–273, 2008.

[53] T. Abu-Zayyad et al. (HiRes/MIA Collaboration). Measurement of the cosmic ray energy spectrum and composition from 10^{17} to $10^{18.3}$ eV using a hybrid fluorescence technique. *Astrophysical Journal*, 557:686–699, 2001.

[54] Y. Fedorova for the HiRes Collaboration. Cosmic Rays composition measurements by the HiRes-Stereo. *Proc. 30th Int. Cosmic Ray Conf. (Merida, Mexico)*, 2007.

[55] M. Unger for the Pierre Auger Collaboration. Study of the Cosmic Ray Composition above 0.4 EeV using the Longitudinal Profiles of Showers observed at the Pierre Auger Observatory. *Proc. 30th Int. Cosmic Ray Conf. (Merida, Mexico)*, 2007. see also arXiv: 0706.1105v1 [astro-ph].

[56] M. Unger for the Pierre Auger Collaboration. Composition studies with the Pierre Auger Observatory. *to appear in Proc. CRIS 2008*, 2008.

[57] J. Abraham et al. (Pierre Auger Collaboration). An upper limit to the photon fraction in cosmic rays above 10^{19} eV from the Pierre Auger Observatory. *Astroparticle Physics*, 27:155–168, 2007.

[58] J. Abraham et al. (Pierre Auger Collaboration). Upper limit on the cosmic-ray pho-
ton flux above 10^{19} eV using the surface detector of the Pierre Auger Observatory.
Astroparticle Physics, 29:243–256, 2008.

[59] J. Abraham et al. (Pierre Auger Collaboration). Upper Limit on the Diffuse Flux of
Ultrahigh Energy Tau Neutrinos from the Pierre Auger Observatory. *Physical Review
Letters*, 100:211101, 2008.

[60] E. Waxman and J. Bahcall. High energy neutrinos from astrophysical sources: An
upper bound. *Phys. Rev. D*, 59:023002, 1999.

[61] J. Bahcall and E. Waxman. High energy astrophysical neutrinos: The upper bound is
robust. *Phys. Rev. D*, 64:023002, 2001.

[62] R. Engel, D. Seckel, and T. Stanev. Neutrinos from propagation of ultrahigh energy
protons. *Phys. Rev. D*, 64:093010, 2001.

[63] A. Haungs et al. (KASCADE-Grande Collaboration). Kascade Grande results. *Proc.
XV ISVHECRI*, 2008.

[64] M. Nagano et al. Energy spectrum of primary cosmic rays above $10^{17.0}$ eV determined
from extensive air shower experiments at Akeno. *Journal of Physics G (Nuclear Physics)*,
18:423–442, 1992.

[65] M. Takeda et al. Energy determination in the Akeno Giant Air Shower Array experi-
ment. *Astroparticle Physics*, 19:447–462, 2003.

[66] R. U. Abbasi et al. First Observation of the Greisen-Zatsepin-Kuzmin Suppression.
Physical Review Letters, 100:101101, 2008.

[67] J. Abraham et al. (Pierre Auger Collaboration). Observation of the suppression of the
flux of cosmic rays above 4×10^{19} eV. *Physical Review Letters*, 101:061101, 2008.

[68] K-H Kampert. Ultra high-energy cosmic ray observations. *Proc. TAUP 2007 (Journal of
Physics: Conference Series)*, 120(6), 2008. see also ArXiv e-prints: 0801.1986.

[69] A. Haungs, H. Rebel, and M. Roth. Energy spectrum and mass composition of high-
energy cosmic rays. *Reports on Progress in Physics*, 66(7):1145–1206, 2003.

[70] J. R. Hörandel. Models of the knee in the energy spectrum of cosmic rays. *Astroparticle
Physics*, 21:241–265, 2004.

[71] T. K. Gaisser. Cosmic Rays at the Knee. In K. Sato and J. Hisano, editors, *Energy Budget
in the High Energy Universe*, 2007.

[72] V. S. Ptuskin et al. Diffusion and drift of very high energy cosmic rays in galactic
magnetic fields. *Astronomy and Astrophysics*, 268:726–735, 1993.

[73] J. Candia, E. Roulet, and L. N. Epele. Turbulent diffusion and drift in galactic magnetic
fields and the explanation of the knee in the cosmic ray spectrum. *Journal of High
Energy Physics*, 12:33, 2002.

[74] E. G. Berezhko and H. J. Völk. Spectrum of Cosmic Rays Produced in Supernova Remnants. *Astrophysical Journal Letters*, 661:L175–L178, 2007.

[75] M. A. Lawrence, R. J. O. Reid, and A. A. Watson. The cosmic ray energy spectrum above 4×10^{17} eV as measured by the Haverah Park array. *Journal of Physics G (Nuclear Physics)*, 17:733–757, 1991.

[76] D.J. Bird and others (Fly's Eye Collaboration). Evidence for correlated changes in the spectrum and composition of cosmic rays at extremely high energies. *Phys. Rev. Lett.*, 71:3401–3404, 1993.

[77] J. R. Hörandel. A review of experimental results at the knee. *Journal of Physics: Conference Series*, 47:41–50, 2006.

[78] A. A. Penzias and R. W. Wilson. A Measurement of Excess Antenna Temperature at 4080 Mc/s. *Astrophysical Journal*, 142:419–421, 1965.

[79] K. Greisen. End to the Cosmic-Ray Spectrum? *Phys. Rev. Letters*, 16:748–750, 1966.

[80] G.T. Zatsepin and V.A. Kuz'min. Upper Limit of the Spectrum of Cosmic Rays. *Sov. Phys. JETP Lett. (engl. transl.: Journal of Experimental and Theoretical Physics)*, 4:78–80, 1966.

[81] J. L. Puget, F. W. Stecker, and J. H. Bredekamp. Photonuclear interactions of ultra-high energy cosmic rays and their astrophysical consequences. *Astrophysical Journal*, 205:638–654, 1976.

[82] F. W. Stecker and M. H. Salamon. Photodisintegration of Ultra-High-Energy Cosmic Rays: A New Determination. *Astrophysical Journal*, 512:521–526, 1999.

[83] D. Allard, N. G Busca, G. Decerprit, A. V. Olinto, and E. Parizot. Implications of the cosmic ray spectrum for the mass composition at the highest energies. 2008. ArXiv e-prints: 0805.4779v1 [astro-ph] (to appear in JCAP).

[84] V. Berezinsky, A. Gazizov, and S. Grigorieva. On astrophysical solution to ultrahigh energy cosmic rays. *Phys. Rev. D*, 74:043005, 2006.

[85] D. Allard, E. Parizot, and A. V. Olinto. On the transition from galactic to extragalactic cosmic-rays: Spectral and composition features from two opposite scenarios. *Astroparticle Physics*, 27:61–75, 2007.

[86] T. Stanev, R. Engel, A. Mücke, R. J. Protheroe, and J. P. Rachen. Propagation of ultra-high energy protons in the nearby universe. *Phys. Rev. D*, 62:093005, 2000.

[87] T. Yamamoto, K. Mase, M. Takeda, N. Sakaki, and M. Teshima. Signatures of ultra-high energy cosmic ray composition from propagation of nuclei in intergalactic photon fields. *Astroparticle Physics*, 20:405–412, 2004.

[88] J. Szabelski, T. Wibig, and A. W. Wolfendale. Cosmic rays of the highest energies: the case for extragalactic heavy nuclei. *Astroparticle Physics*, 17:125–131, 2002.

[89] A.M. Hillas. Can diffusive shock acceleration in supernova remnants account for high-energy galactic cosmic rays? *J. Phys. G: Nuclear Part. Phys.*, 31:95–131, 2005.

[90] H. Klages for the Pierre Auger Collaboration. HEAT: Enhancement Telescopes for the Pierre Auger Southern Observatory in Argentina. *Proc. 30th Int. Cosmic Ray Conf. (Merida, Mexico)*, 2007.

[91] A. Etchegoyen for the Pierre Auger Collaboration. AMIGA: A muon detector and in-filled array for the Auger Observatory. *Proc. 30th Int. Cosmic Ray Conf. (Merida, Mexico)*, 2007. see also arXiv: 0710.1646v1 [astro-ph].

[92] D. Nitz for the Pierre Auger Collaboration. The Northern Site of the Pierre Auger Observatory. *Proc. 30th Int. Cosmic Ray Conf. (Merida, Mexico)*, 2007. see also arXiv: 0706.3940v1 [astro-ph].

[93] J. Oehlschläger. private communication, 2008.

[94] X. Bertou et al. Calibration of the surface array of the Pierre Auger Observatory. *Nucl. Instr. Meth. A*, 568:839–846, 2006.

[95] B. Fick et al. The Central Laser Facility at the Pierre Auger Observatory. *JINST*, 1:P11003, 2006.

[96] S. Y. BenZvi et al. The Lidar system of the Pierre Auger Observatory. *Nucl. Instr. Meth. A*, 574:171–184, 2007.

[97] D. Veberič, M. Roth. SD Reconstruction (Offline Reference Manual). *Auger Technical Note*, GAP-2005-035, 2005.

[98] E. Parizot et. al. for the Pierre Auger Collaboration. Aperture calculation of the Pierre Auger Observatory surface detector. *29th Int. Cosmic Ray Conf. (Pune, India)*, 2005. see also: astro-ph/0511104v1.

[99] D. Allard et al. for the Pierre Auger Collaboration. The trigger system of the Pierre Auger Surface Detector: operation, efficiency and stability. *29th Int. Cosmic Ray Conf. (Pune, India)*, 2005. see also: astro-ph/0510320.

[100] H. Gemmeke et al. Design of the trigger system for the AUGER fluorescence detector. *IEEE Transactions on Nuclear Science*, 47:371–375, 2000.

[101] T. Asch, H. Gemmeke, M. Kleifges, R. Ulrich, M. Unger. Proposal for a New Third Level Trigger for the Fluorescence Telescopes. *Auger Technical Note*, GAP-2005-069, 2005.

[102] A. Schmidt, T. Asch, M. Kleifges, H.-J. Mathes, H. Gemmeke. New Third Level for the Fluorescence Telescopes. *Auger Technical Note*, GAP-2007-118, 2007.

[103] J. Brack, R. Meyhandan, G. Hofman, J. Matthews. Absolute photometric calibration of large aperture optical systems. *Astroparticle Physics*, 20:653, 2004.

[104] P. Bauleo et al. for the Pierre Auger Collaboration. Absolute Calibration of the Auger Fluorescence Detectors. *29th Int. Cosmic Ray Conf. (Pune, India)*, 2005.

[105] C. Delle Fratte et al. On the stability of the FD cameras. *Auger Technical Note*, GAP-2007-111, 2007.

[106] K. Daumiller. private communication, 2008.

[107] C. Delle Fratte et al. On the stability of the FD cameras - update 1. *Auger Technical Note*, GAP-2008-129, 2008.

[108] S. Argiro et al. The Offline Software Framework of the Pierre Auger Observatory. *Nucl. Instr. Meth. A*, 580, 2007.

[109] F. Schüssler et al. The Auger Observer. http://augerobserver.fzk.de.

[110] R. Ulrich, J. Blümer, R. Engel, F. Schüssler, and M. Unger. Implementation of the differential atmosphere in a curved geometry in $\overline{\text{Off}\underline{\text{line}}}$. *Auger Technical Note*, GAP-2007-007, 2007.

[111] I.C. Mariş, M. Roth, F. Schüssler, R. Ulrich and M. Unger. Data Summary Trees and Shower Visualization for Reconstructed Auger Events. *Auger Technical Note*, GAP-2006-081, 2006.

[112] M. Prouza et al. Star tracking using background data of FD telescopes. *Auger Technical Note*, GAP-2005-041, 2005.

[113] P. Sokolsky. *Introduction to ultrahigh energy cosmic ray physics*. Addison-Wesley, 1989.

[114] B. Fick for the Pierre Auger Collaboration. Hybrid performance of the Pierre Auger Observatory and reconstruction of hybrid events. *Proc. of 28th Int. Cosmic Ray Conf., Tsukuba, Japan*, 2003. see also: astro-ph/0308512.

[115] B. Dawson, M. Debes, and P. Sommers. Shower Profile Reconstruction with Engineering Array FD Data. *Auger Technical Note*, GAP-2001-016, 2001.

[116] M. Unger. Shower Profile Reconstruction from Fluorescence and Cherenkov light. *Auger Technical Note*, GAP-2006-010, 2006.

[117] F. Kakimoto et al. A measurement of the air fluorescence yield. *Nucl. Instr. Meth.*, A372:527–533, 1996.

[118] M. Ave et al. (Airfly Collaboration). Temperature and Humidity Dependence of Air Fluorescence Yield measured by AIRFLY. *to be published in Proc. 5th Fluorescence Workshop, El Escorial - Madrid, Sept. 2007*, 2007.

[119] B. Keilhauer, J. Blümer, R. Engel, and H. O. Klages. Altitude dependence of fluorescence light emission by extensive air showers. *to be published in Proc. 5th Fluorescence Workshop, El Escorial - Madrid, Sept. 2007*, 2008.

[120] M. Giller et al. Energy spectra of electrons in the extensive air showers of ultra-high energy. *J. Phys. G: Nucl. Part. Phys.*, 30:97–105, 2004.

[121] A. Bucholtz. Rayleigh-scattering calculations for the terrestrial atmosphere. *Applied Optics*, 34:2765, 1995.

[122] S. Y. BenZvi et al. for the Pierre Auger Collaboration. Measurement of Aerosols at the Pierre Auger Observatory. *Proc. 30th Int. Cosmic Ray Conf. (Merida, Mexico)*, 2007. see also arXiv: 0706.3236 [astro-ph].

[123] M. Unger, R. Engel, F. Schüssler, and R. Ulrich. Longitudinal Shower Profile Reconstruction from Fluorescence and Cherenkov Light. *Proc. 30th Int. Cosmic Ray Conf. (Merida, Mexico)*, 2007. see also arXiv:0706.1501v1 [astro-ph].

[124] A. M. Hillas. Angular and energy distributions of charged particles in electron-photon cascades in air. *Journal of Physics G (Nuclear Physics)*, 8:1461–1473, 1982.

[125] F. Nerling, J. Blümer, R. Engel, and M. Risse. Universality of electron distributions in high-energy air showers Description of Cherenkov light production. *Astroparticle Physics*, 24:421–437, 2006.

[126] S. Y. BenZvi, B. M. Connolly, J. A. J. Matthews, M. Prouza, E. F. Visbal, and S. Westerhoff. Measurement of the aerosol phase function at the Pierre Auger Observatory. *Astroparticle Physics*, 28:312–320, 2007.

[127] A. M. Hillas. The sensitivity of Cerenkov radiation pulses to the longitudinal development of cosmic-ray showers. *Journal of Physics G (Nuclear Physics)*, 8:1475–1492, 1982.

[128] T.K. Gaisser and A.M. Hillas. *Proc. 15th Int. Cosmic Rays Conference (Plodviv, Bulgaria)*, 8:353, 1977.

[129] D. Heck et al. CORSIKA: A Monte Carlo Code to Simulate Extensive Air Showers. *Forschungszentrum Karlsruhe Report FZKA 6019*, 1998.

[130] T. Bergmann et al. One-dimensional hybrid approach to extensive air shower simulation. *Astroparticle Physics*, 26:420–432, 2007.

[131] T. Pierog et al. Latest Results from the Air Shower Simulation Programs CORSIKA and CONEX. *Proc. 30th Int. Cosmic Ray Conf. (Merida, Mexico)*, 2007. see also arXiv: 0802.1262 [astro-ph].

[132] M. Nagano et al. Photon yields from nitrogen gas and dry air excited by electrons. *Astroparticle Physics*, 20:293–309, 2003.

[133] R. Knapik for the Pierre Auger Collaboration. The Absolute, Relative and Multi-Wavelength Calibration of the Pierre Auger Observatory Fluorescence Detectors. *Proc. 30th Int. Cosmic Ray Conf. (Merida, Mexico)*, 2007. see also arXiv: 0708.1924v1 [astro-ph].

[134] M. Unger, R. Engel, F. Schüssler, and R. Ulrich. Lateral shower light distributions in the Cherenkov-Fluorescence-Matrix Profile Reconstruction. *Auger Technical Note*, GAP-2008-052, 2008.

[135] B. Dawson for the Pierre Auger Collaboration. Hybrid performance of the Pierre
      Auger Observatory. *Proc. 30th Int. Cosmic Ray Conf. (Merida, Mexico)*, 2007. see also
      arXiv: 0706.1105v1 [astro-ph].

[136] J. Abraham et al. (Pierre Auger Collaboration). Pierre Auger Project Design Report.
      http://www.auger.org/admin/DesignReport, 1997.

[137] European Commission and Pierre Auger Collaboration. Auger Access.
      http://www.augeraccess.net.

[138] M. Unger. private communication, 2008.

[139] R. Smida. private communication, 2008.

[140] J. Rautenberg for the Pierre Auger Collaboration. Online Monitoring of the Pierre
      Auger Observatory. *Proc. 30th Int. Cosmic Ray Conf. (Merida, Mexico)*, 2007.

[141] M. Unger, R. Engel, F. Schüssler, R. Ulrich. Measurement of $\langle X_{\max} \rangle$ as function of
      Energy. *Auger Technical Note*, GAP-2007-005, 2007.

[142] R. Engel et al. Air shower calculations with the new version of Sibyll. *Proc. 26th Int.
      Cosmic Ray Conf. (Salt Lake City, USA)*, page 415, 1999.

[143] S. Ostapchenko. QGSJET-II: Results for extensive air showers. *Nucl. Phys. B (Proc.
      Suppl.)*, 151:143, 2006.

[144] S. Sciutto et al. AIRES, a system for air shower simulation.
      http://www.fisica.unlp.edu.ar/auger/aires.

[145] H. Drescher and G. Farrar. Air shower simulations in a hybrid approach using cascade
      equations. *Phys. Rev. D*, 67:116001, 2003.

[146] S. Y. BenZvi. private communication, 2008.

[147] T. Abu-Zayyad and others (HiRes Collaboration). A measurement of the average lon-
      gitudinal development profile of cosmic ray air showers between 10^{17} and 10^{18} eV.
      Astroparticle Physics, 16:1–11, 2001.

[148] F. Schüssler et al. Untersuchung von longitudinalen Luftschauerprofilen. Frühjahrsta-
      gung der Deutschen Physikalischen Gesellschaft (Heidelberg, Germany), 2007.

[149] L. Prado Jr. et al. Simulation of the fluorescence detector of the Pierre Auger Observa-
      tory. *Nucl. Instr. Meth.*, 545:632–642, 2005.

[150] P. Assis, D. D'Urso, R. Engel, P. Goncalves, F. Guarino, S. Müller, L. Nozka, S. Petrera,
      M. Pimenta, F. Salamida, F. Schüssler, B. Tome, R. Ulrich, M. Unger, and L. Valore.
      Manual of fluorescence detector simulation in Offline. *Auger Technical Note*, GAP-2005-
      014, 2008.

[151] B. Keilhauer et al. for the Pierre Auger Collaboration. Atmospheric profiles at the southern pierre auger observatory and their relevance to air shower measurement. 2005. see also: astro-ph/0507275.

[152] Geant4 Collaboration. Geant4-a simulation toolkit. *Nucl. Instr. Meth. A*, 506:250–303, 2003.

[153] R. Ulrich, J. Blümer, R. Engel, F. Schüssler, and M. Unger. Mapping of FD camera pixels to electronics readout channels and its implementation in Offline. *Auger Technical Note*, GAP-2007-003, 2007.

[154] A. Menshikov, M. Kleifges, and H. Gemmeke. Fast gain calibration of photomultiplier and electronics. *IEEE Transactions on Nuclear Science*, 50:1208–1213, 2003.

[155] R. Caruso and S. Petrera. Measurement of the sky photon background flux at Los Leones. *Auger Technical Note*, GAP-2004-072, 2004.

[156] S. Petrera and F. Salamida. Status of the sky photon background flux measurement. *Auger Technical Note*, GAP-2006-014, 2006.

[157] A. Schmidt, T. Asch, Gemmeke H., H.-J. Mathes, A. Menchikov, F. Schüssler, and D. Tcherniakhovski. Third Level Trigger for the Fluorescence Telescopes of the Pierre Auger Observatory. *to appear in Nucl. Instr. Meth. A*, 2008. see also: arXiv:0807.4421v2 [astro-ph].

[158] M. Settimo, L. Perrone, G. Cataldi, I. De Mitri, and D. Martello. Parameterisation of the "Lateral Trigger Probability" functions at low energies. *Auger Technical Note*, GAP-2007-069, 2007.

[159] L. Cazón, R. A. Vázquez, A. A. Watson, and E. Zas. Time structure of muonic showers. *Astroparticle Physics*, 21:71–86, 2004.

[160] R. Ulrich, L. Cazonr, R. Engel, M. Roth, F. Schüssler, and M. Unger. Ultra-fast hybrid simulations with SDSIMPLESIM. *Auger Technical Note*, GAP-2008-061, 2008.

[161] K. Kamata and J. Nishimura. *Prog. Theo. Phys. Suppl.*, 6:93, 1958.

[162] K. Greisen. *Prog. Cosmic Rays Phys.*, III:26, 1965.

[163] J. Barbosa et al. Indirect determination of the missing energy content in extensive air showers. *Astroparticle Physics*, 22:159–166, 2004.

[164] C. Bonifazi et. al. for the Pierre Auger Collaboration. Angular resolution of the Pierre Auger Observatory. *29th Int. Cosmic Ray Conf. (Pune, India)*, 2005.

[165] S. Yoshida. Energy determination of trans-EeV cosmic rays. *Comptes Rendues Physique*, 5:483–493, 2004.

[166] K. Werner et al. Parton Ladder Splitting and the Rapidity Dependence of Transverse Momentum Spectra in Deuteron-Gold Collisions at RHIC. *Phys.Rev. C*, 74, 2006.

[167] T. Pierog. private communication, 2008.

[168] V. Scherini. *Study of the performance of the Pierre Auger Observatory and search for primary cosmic ray photons.* PhD thesis, University of Wuppertal, 2007.

[169] L. Perrone, S. Petrera, and F. Salamid. Gaisser-Hillas Profiles and FD Simulation. *Auger Technical Note*, GAP-2005-087, 2007.

[170] M. Unger et al. Systematic uncertainties on $\langle X_{max} \rangle$ and its fluctuations. http://www-ik.fzk.de/~munger/Xmax.

[171] F. Schüssler et al. Cloud coverage from Lidar and CLF measurements and the influence on air shower observations. *Auger Technical Note*, GAP-2008-13, 2008.

[172] A. Tonachini et al. Detecting Clouds with Elastic Lidar Telescopes. *Auger Technical Note*, GAP-2007-038, 2008.

[173] L. Perrone for the Pierre Auger Collaboration. Measurement of the UHECR energy spectrum from hybrid data of the Pierre Auger Observatory. *Proc. 30th Int. Cosmic Ray Conf. (Merida, Mexico)*, 2007. see also arXiv:0706.2643v1 [astro-ph].

[174] G. J. Feldman and R. D. Cousins. Unified approach to the classical statistical analysis of small signals. *Phys. Rev. D*, 57:3873–3889, 1998.

[175] R.U. Abbasi and others (HiRes Collaboration). Studies of systematic uncertainties in the estimation of the monocular aperture of the HiRes experiment. *Astroparticle Physics*, 27:370–381, 2007.

[176] C. O. Escobar, L. G. dos Santos, and R. A. Vazquez. The Effect of Non Gaussian Errors on the Determination of Steeply Falling Spectra. *ArXiv e-prints astro-ph/0202172*, 2002.

[177] R. Engel for the Pierre Auger Collaboration. Test of hadronic interaction models with data from the Pierre Auger Observatory. *Proc. 30th Int. Cosmic Ray Conf. (Merida, Mexico)*, 2007. see also arXiv: 0706.1921v1 [astro-ph].

[178] S. Müller. A Novel Method of Determining the Energy Scale of the Pierre Auger Observatory. *Diplomarbeit Universität Karlsruhe (GAP-2008-056)*, 2008.

[179] R. Barlow. Systematic Errors: facts and fictions. *ArXiv e-prints hep-ex/0207026*, 2002.

[180] M. Roth for the Pierre Auger Collaboration. Measurement of the UHECR energy spectrum using data from the Surface Detector of the Pierre Auger Observatory. *Proc. 30th Int. Cosmic Ray Conf. (Merida, Mexico)*, 2007. see also arXiv: 0706.2096v1 [astro-ph].

[181] C. Bleve for the Pierre Auger Collaboration. Weather induced effects on extensive air showers observed with the surface detector of the Pierre Auger Observatory. *Proc. 30th Int. Cosmic Ray Conf. (Merida, Mexico)*, 2007. see also arXiv: 0706.1491v1 [astro-ph].

[182] D. J. Bird and others (Fly's Eye Collaboration). The cosmic-ray energy spectrum observed by the Fly's Eye. *Astrophysical Journal*, 424:491–502, 1994.

[183] M. Ave, J. Knapp, J. Lloyd-Evans, M. Marchesini, and A. A. Watson. The energy spectrum of cosmic rays in the range $3\times10^{17} - 4\times10^{18}$ eV as measured with the Haverah Park array. *Astroparticle Physics*, 19:47–60, 2003.

[184] M.I. Pravdin et al. Energy Spectrum of Primary Cosmic Rays in the Energy Region of 10^{17} - 10^{20} eV by Yakutsk Array Data. In *Proc. 28th Int. Cosmic Ray Conf.*, page 389, 2003.

[185] T. Wibig and A.W. Wolfendale. Ultra high energy cosmic rays. *Journal of Physics G: Nuclear and Particle Physics*, 34(9):1891–1900, 2007.

[186] J.N. Bahcall and E. Waxman. Has the GZK cutoff been discovered? *Phys. Lett.*, B556:1–6, 2003.

[187] Douglas R Bergman and John W. Belz. Cosmic rays: The second knee and beyond. *Journal of Physics G (Nuclear Physics)*, 34:R359, 2007.

[188] E. Armengaud, G. Sigl, T. Beau, and F. Miniati. CRPropa: A numerical tool for the propagation of UHE cosmic rays, γ-rays and neutrinos. *Astroparticle Physics*, 28:463–471, 2007.

[189] V. Berezinsky. Transition from galactic to extragalactic cosmic rays. *Proc. 30th Int. Cosmic Ray Conf. (Merida, Mexico)*, 2007. see also arXiv:0710.2750 [astro-ph].

[190] D. Allard, N. G Busca, G. Decerprit, A. V. Olinto, and E. Parizot. private communication, adapted from arXiv:0805.4779 (to appear in JCAP), 2008.

[191] N.N. Kalmykov, S.S. Ostapchenko, and A.I. Pavlov. Quark Gluon String Jet Model. *Nucl. Phys. B (Proc. Suppl.)*, 52B:17, 1997.

[192] B. Fick et al. The first Central Laser Facility. *Auger Technical Note*, GAP-2004-003, 2003.

[193] R. Mussa, G. Sequeiros, A. Tonachini. Detecting Clouds with Elastic Lidar Telescopes. *Auger Technical Note*, GAP-2007-038, 2007.

[194] B. Dawson et al. Cloud Camera. Pierre Auger Collaboration Meeting, Malargüe, April 2007.

[195] M. Winnick et al. Status of the Cloud Camera. Pierre Auger Collaboration Meeting, Malargüe, November 2007.

Glossary

ADC	Analog to Digital Converter
ADST	Advanced Data Summary Tree
AGN	Active Galactic Nuclei
APF	Aerosol Phase Function monitor
BGLoop	BackGround Loop fluorescence detector monitoring data
CDAS	Central Data Aquisition System
CLF	Central Laser Facility
CMB	Cosmic Microwave Background
COMM	COMMunication
CONEX	air shower simulation program
CORSIKA	COsmic Ray SImulations for KAscade
CR	Cosmic Ray
DAQ	Data AQuisition
EAS	Extensive Air Shower
FD	Fluorescence Detector
FDAS	Fluorescence detector Data Aquisition System
FLT	First Level Trigger (fluorescence detector)
FOV	Field Of View
FRAM	robotic telescope system
GPS	Global Positioning System
GZK	Greisen-Zatsepin-Kuzmin
HAM	Horiziontal Attenuation Monitor
IoAuger	hybrid data file format
KASCADE	KArlsruhe Shower Core and Array DEtector
LIDAR	LIght Detection And Ranging
LTP	Lateral Trigger Probability
NIST	National Institute of Standards and Technology
NKG	Nishimura Kamata Greisen lateral distribution function

MC	Monte Carlo
MinBias	fluorescence minimal bias datastream
PMT	PhotoMultiplier Tube
QGSJet	Quark Gluon String Jet model of hadronic interactions
SC	Slow Control
SD	Surface Detector
SDP	Shower Detector Plane
Sibyll	hadronic interaction model
SLT	Second Level Trigger (fluorescence detector)
SQL	Structured Query Language
TLT	Third Level Trigger (fluorescence detector)
ToT	Time over Threshold
T3	final fluorescence detector trigger
T5	surface detector quality trigger
UHECR	Ultra High Energy Cosmic Ray
UV	Ultra Violet
VAOD	Vertical Aerosol Optical Depth
XLF	eXtra Laser Facility
XML	eXtensible Markup Language
3ToT	surface detector trigger (3 stations with ToT trigger)

Appendix B

Data reconstruction

The energy spectrum has been derived from hybrid data of the Pierre Auger Observatory collected during the period 11/2005 - 05/2008. Data has been reconstructed for the full period of available physics data, which is defined by the validity of the fluorescence detector calibration constants (12/2004 - 05/2008, for details see Sec. 6.2.1).

The reconstruction was performed with the $\overline{\text{Off}}\underline{\text{line}}$ version `v2r5p1-Godot`. The results, stored in the ADST-format version `v5r1p0_Pozzo`, are available from the (Auger password protected) website:

```
http://www-ik.fzk.de/~fabian/HybridSpectrum/Data/data.htm
```

The reconstruction can be reproduced based on the settings stored within the ADST-format. For details see the ADST-Manual [111]. The reconstruction settings correspond to the official Auger event reconstruction (Observer release `v5r1` [109]). The energy reconstruction is consistent with the surface detector energy calibration used for the spectrum published in [67]. The modification of the energy reconstruction related to the treatment of the lateral extent of Cherenkov light and the light halo correction [134] has been not been used.

During the reconstruction, the default versions of the calibration, Lidar analysis and aerosol databases have been used.

Appendix C

Atmospheric effects

C.1 Cloud detection

One of the major issues related to air shower detection with fluorescence detectors is the accurate description of the atmospheric conditions. In addition to the rather well understood effects of light scattering on aerosols, dust and molecules, changes of the temperature and pressure profiles of the atmosphere have to be monitored and/or modeled very accurately. Another main contribution to misreconstructed longitudinal shower profiles is the presence of clouds. Fluorescence light emitted from cosmic showers is absorbed and/or scattered by clouds, so accurate measurements of cloud details are essential in order to minimize errors in shower reconstruction. Especially the composition analysis relying on parameters of the longitudinal shower development like X_{max} and its fluctuations could be affected by clouds. The cloud coverage also directly influences the hybrid exposure calculations. Clouds and their influence on the measurements can currently not be simulated. It is therefore necessary to be able to detect clouds during data taking and discard these periods for a reliable measurement of the cosmic ray flux. Without that possibility, cloud related uncertainties were the largest source of systematic uncertainty for the hybrid spectrum ($\sigma_{\mathrm{flux}} \approx 16\%$, [173]).

C.1.1 Available cloud information

There are currently two methods of obtaining cloud information - the Central Laser Facility [95, 192] and Lidar Telescope [193] stations located at each eye.*

The Central Laser Facility provides an abundance of atmospheric monitoring data that can easily be compared to shower information from hybrid reconstructions. Unfortunately the only variable directly related to clouds is the measurement of the height of the lowest cloud layer above the CLF. The Lidar systems provide more detailed information like the cloud height at each of the Lidar stations, the overall cloud coverage, etc. The analyzed information is available in an $\overline{\mathrm{Off}}\underline{\mathrm{line}}$ cloud database [172].

---

*First results of a semi-automatic analysis of infrared cloud camera pictures have already shown great potential [194, 195], but the corresponding data is not yet available for large scale analysis.

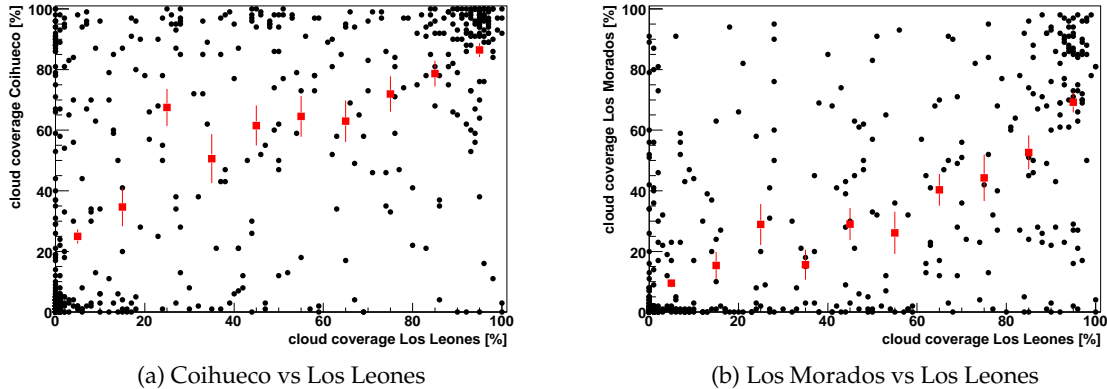(a) Coihueco vs Los Leones   (b) Los Morados vs Los Leones

Figure C.1.1: Comparison between Lidar measurements of different stations.

C.1.2   Comparison between different cloud measurements

In the following section we are discussing the reliability of the cloud measurements. Especially the Lidar stations, located near each fluorescence detector, are detecting clouds rather far away from the actual air showers as they perform vertical and horizontal scans only outside the field-of-view (FOV) of the FD in order not to disturb data taking. In addition, as the available amount of information about clouds is limited, i.e. not all FD data taking periods are covered with cloud measurements from all stations, it is important to check if for time periods with no Lidar measurement for a given eye, the use of measurements from different eyes is a valid method. This is directly connected to the assumption that the cloud coverage is uniform over the whole array at a given time.

C.1.3   Lidar measurements from different stations

One important cross-check is therefore the direct comparison of Lidar measurements taken at the same time with different stations. As can be seen in figure C.1.1, the measured cloud coverages seem to agree only for time periods with almost complete cloud coverage. The agreement is reduced for periods with no clouds detected in one station. For intermediate cloud coverages the horizontal uniformity assumption is not valid as can be seen in the large spread of the measured values.

A very natural explanation is that only if the sky is completely covered with clouds (corresponding roughly to a measured cloud coverage $\geq 80\%$) the horizontal uniformity over the whole array is given. It seems obvious that partial sky coverage is a very local (and probably very time dependent) phenomenon. One might therefore conclude that a reliable cloud measurement based on the Lidar systems, which is valid for the whole observatory, is only possible for high cloud coverages and to some extend for cloudless periods.

C.1.4   Lidar vs. CLF

With the CLF being within the FOV of the FD, its cloud measurements could be more reliable for the event selection and analysis.

(a) all data
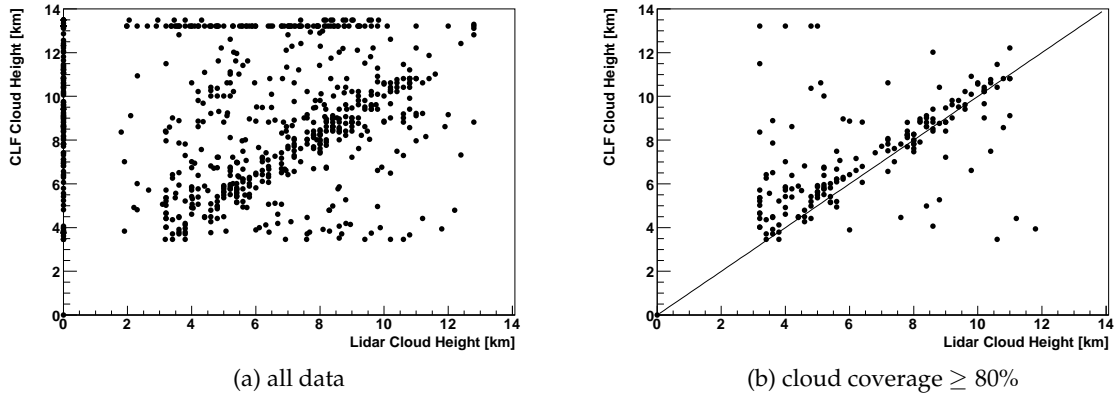
(b) cloud coverage $\geq 80\%$

Figure C.1.2: Comparison between CLF and Lidar cloud height measurements.

A direct comparison between the cloud height measured with the CLF and corresponding Lidar measurements is shown in figure C.1.2a. This plot clearly demonstrates the limiting factor of the CLF cloud information. The points along the y-axis show that there are several time periods that have a Lidar cloud height of zero (indicating clear skies in the current implementation of the Lidar database), while the CLF data range from 3 to 13 km. The inverse case is also observed: As there is no entry in the $\overline{\text{Off}}\underline{\text{line}}$- CLF database with a cloud height above 13 km, we assume this to be the maximum range of the CLF measurements and cloud heights of about this value are probably indicating a clear sky above the CLF. Corresponding Lidar measurements show a large spread over all possible height values.

Restricting the data to measurements that have clouds detected with the Lidar systems and for which we can assume reasonably good horizontal uniformity, i.e. a cloud coverage $\geq 80\%$ (cf. Sec. C.1.3), a clear correlation is found between the cloud heights of the two systems. The two systems therefore give similar results only for time periods with a lot of clouds, i.e. an almost complete cloud coverage over the full array. The difficulty here is, that for periods with no Lidar measurement available, the cloud coverage is not known which means that currently the analysis has to rely on Lidar measurements alone. Combinations of cloud information from all systems is forseen in the future to increase the accuracy.

C.2 Comparison between reconstructed hybrid events and cloud measurements

The full reconstructed hybrid dataset has been used to correlate cloud information from the CLF and the Lidar databases on an event-by-event basis with air shower and reconstruction parameters. In order to retain as much statistics as possible for this first overview we only used very basic event selection criteria:

- The event has a 'hybrid' geometry reconstruction.

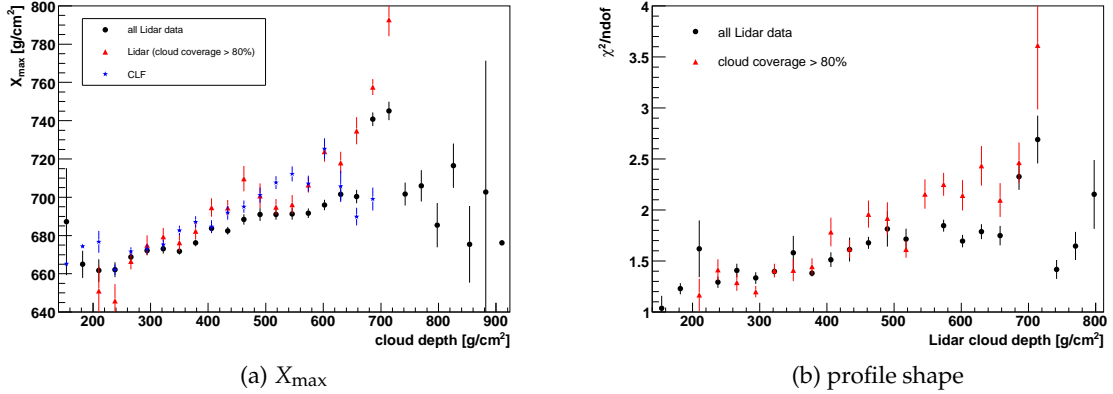- The X_{max} is in the field-of-view of the FD.

(a) X_{max} (b) profile shape

Figure C.2.3: Influence of clouds on the shape of the longitudinal shower profile.

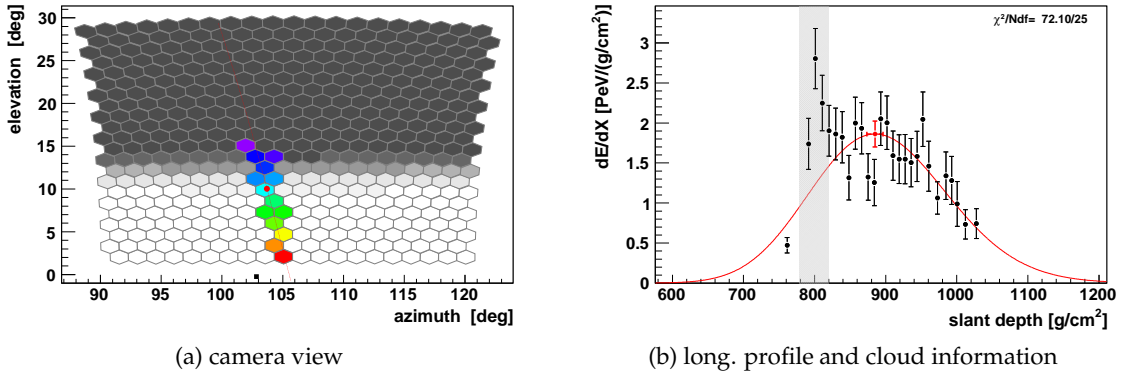(a) camera view   (b) long. profile and cloud information

Figure C.2.4: Example of an air shower being strongly affected by clouds. Projected onto the surface of the camera of the fluorescence detector, a clear obscuration is seen (left panel). Scattered light inside the cloud and the obscuration of large parts of the longitudinal profile are biasing the reconstruction (right panel). Cloud parameters reconstructed by the Lidar data analysis (shaded area in right panel) are in good agreement with the air shower observations.

C.2.1   CLF vs. hybrid data

As mentioned above, the only cloud related variable available in the $\overline{\text{Off}}\underline{\text{line}}$ "quality data-base" is the height of the lowest cloud layer. Based on the atmospheric profile used during the event reconstruction, this cloud height can be transferred into vertical depth and then, based on the reconstructed shower geometry, into slant depth.

A weak correlation between X_{max} and the height of clouds is found (cf. Fig. C.2.3a). The presence of clouds deep in the atmosphere seems to bias the X_{max} observation towards higher values. This effect can easily be understood as clouds are scattering and/or absorbing the fluorescence light emitted by the shower and one can therefore not expect to observe a shower maximum higher than the cloud layer.
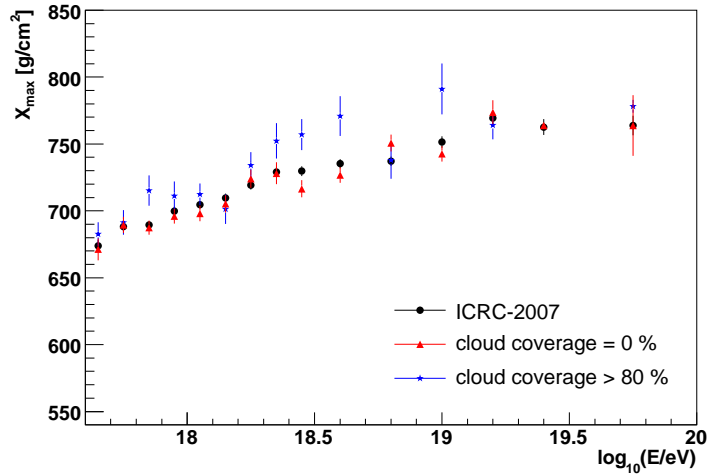
Figure C.2.5: Influence of clouds on the elongation rate.

C.2.2 Lidar vs. hybrid data

The same feature is observed between the depth of the cloud layer measured with the Lidar systems and the reconstructed X_{max} of the shower (cf. Fig. C.2.3a). Selecting only periods with high cloudiness, i.e. cloud coverages $\geq$ 80%, the effect is clearly increased. The influence of this bias on mass composition studies with hybrid events is discussed in section C.2.3.

It is even more evident that clouds disturb the longitudinal profile from figure C.2.3b. As the cloud height decreases (cloud depth increases) the χ^2/ndof of the longitudinal profile fit with the Gaisser-Hillas functional form [128] increases. Again, the effect is increased by selecting high cloud coverages (see red triangles in figure C.2.3b).

As an example the longitudinal profile of an hybrid event is shown in figure C.2.4. Scattered light from within the cloud is causing a spike in the longitudinal profile. The obscuration of large parts of the profile are strongly biasing the air shower reconstruction.

C.2.3 Influence on mass composition measurements

One of the ongoing hybrid analysis is the measurement of the elongation rate and the subsequent determination of the primary mass composition. In order to determine the influence of clouds on this analysis, all ($\approx$ 4000) events used for the ICRC-2007 elongation rate measurement [55] were analyzed and 3032 of them could be connected with cloud information from the Lidar system.

1011 events have been measured during clear weather conditions (cloud coverage = 0%) and 436 have been observed during cloudy conditions (cloud coverage > 80%). The elongation rates of these subsamples are shown together with the default one in figure C.2.5. As the analysis in the previous sections already suggested, clouds significantly influence the observable X_{max} distributions in the sense that data taken during very cloudy conditions contains deeper showers. For illustration see the disturbed longitudinal profile in figure C.2.4.

With X_{max} being larger, these events will favor a lighter primary composition. On the other hand, the cloud-free elongation rate is in good agreement with the ICRC one (due to the apparently good average weather conditions in Malargüe).

Important information on the primary mass composition can also be derived from the shower fluctuations, i.e. the RMS of the X_{max} distributions. These distributions are shown in figure C.2.6 for four energy bins.

In order to quantify the influence of clouds on the mass composition analysis, we derive the difference in $\langle X_{\mathrm{max}} \rangle$ and the RMS of the subsamples as function of energy. The results are shown in figure C.2.7. Although the difference between the clear and cloudy data sample is rather large ($\Delta\langle X_{\mathrm{max}}\rangle = 14.8 \pm 3.6\,\mathrm{g/cm^2}$ and $\Delta\mathrm{RMS} = 5.1 \pm 2.5\,\mathrm{g/cm^2}$), the agreement between the clear and the default sample are much better ($\Delta\langle X_{\mathrm{max}}\rangle = 4.2 \pm 2.1\,\mathrm{g/cm^2}$ and $\Delta\mathrm{RMS} = 2.5 \pm 1.5\,\mathrm{g/cm^2}$).

One possible way to reduce the cloud influence is the removal of all periods which are known to be affected by clouds from the analysis. This is done conservatively by removing all events which have a Lidar measurement with cloud coverages $> 20\%$. The resulting X_{max} distributions are very similar to the cloud-free subsample as can be seen in figure C.2.8. With a reduction of the usable statistics of about 20% this seems to be a very reasonable compromise between data quality and statistical uncertainty. The resulting elongation rate is shown in figure C.2.9a. The remaining systematic uncertainty can be derived by comparison of the X_{max} distribution with the subsample of absolutely clear nights, i.e. database entries of cloud coverage 0% shown in figure C.2.9b. It is not significantly different from zero ($\Delta\langle X_{\mathrm{max}}\rangle = 1.6 \pm 0.9\,\mathrm{g/cm^2}$ and $\Delta\mathrm{RMS} = 1.1 \pm 0.9\,\mathrm{g/cm^2}$.
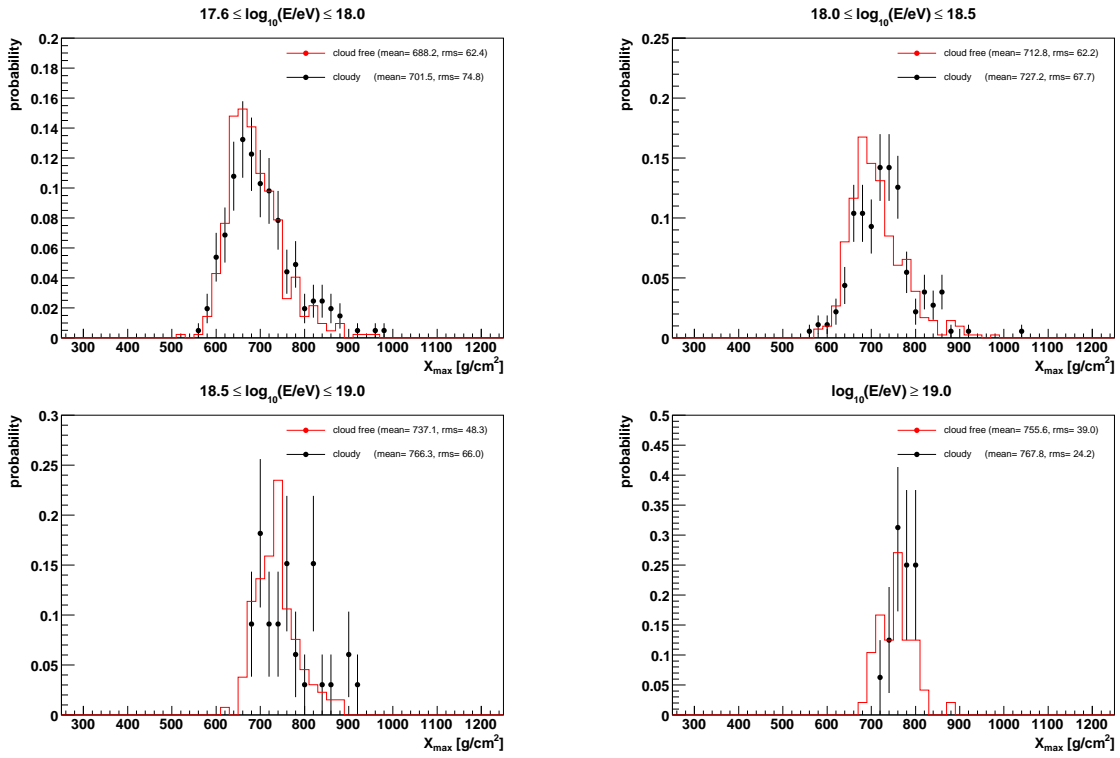
Figure C.2.6: Influence of clouds on the X_{max} distribution. Selection criteria correspond to the one used for the ICRC-2007 [55].
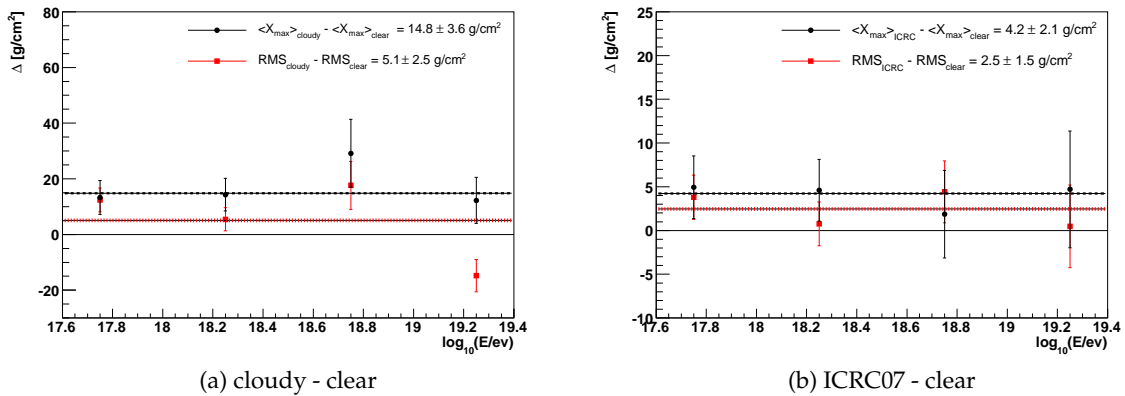

(a) cloudy - clear

(b) ICRC07 - clear

Figure C.2.7: $\langle X_{max} \rangle$ and RMS differences between data samples of different cloudiness. The underlying distributions are shown in figure C.2.6.
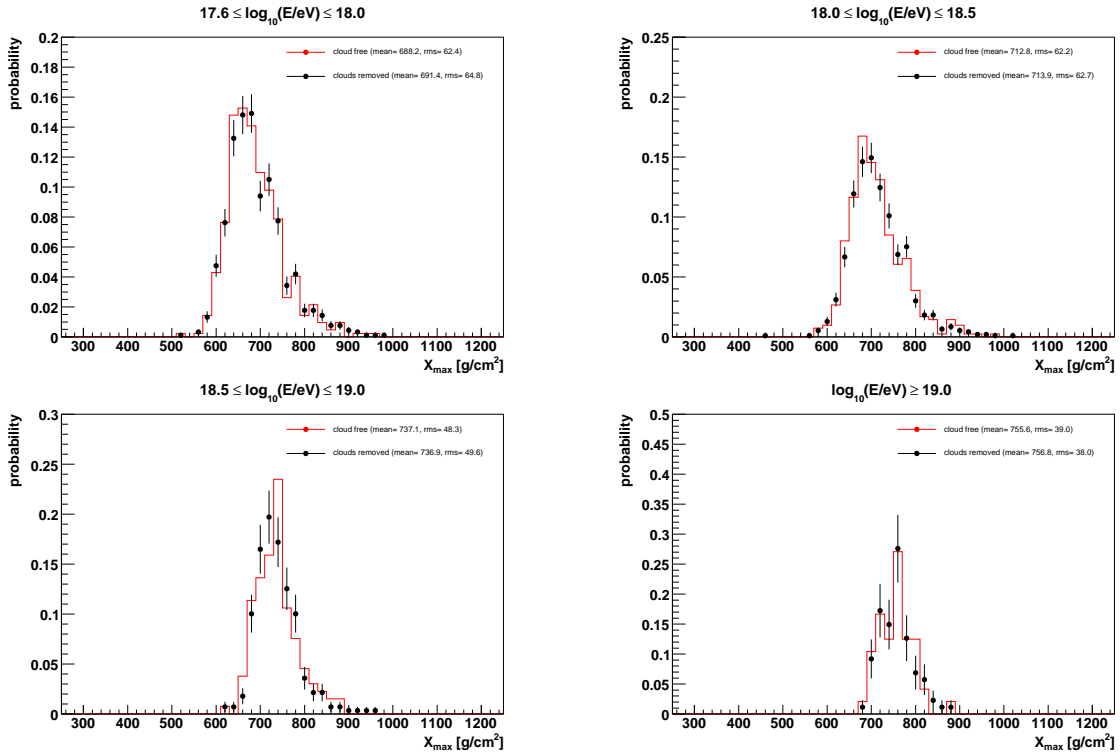
Figure C.2.8: Influence of clouds on the X_{max} distribution. Selection criteria correspond to the one used for the ICRC-2007 [55]. In addition all events with cloud coverages $< 20\%$ have been removed.
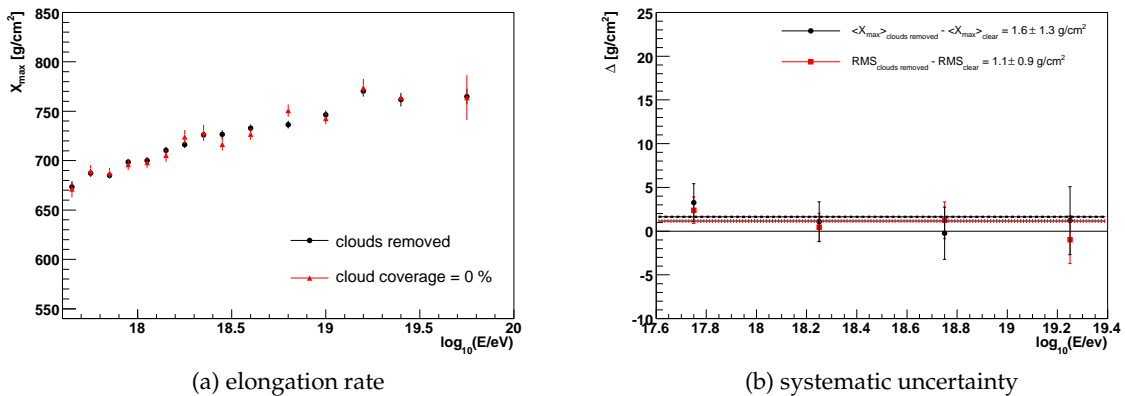

(a) elongation rate

(b) systematic uncertainty

Figure C.2.9: Elongation rate following the ICRC-2007 with clouds removed and the remaining cloud related systematic uncertainty.

Appendix D

MC validation and systematic uncertainties

D.1   Comparison between data and MC

(a) X_{max} from FOV boundary

(b) zenith angle

(c) profile fit
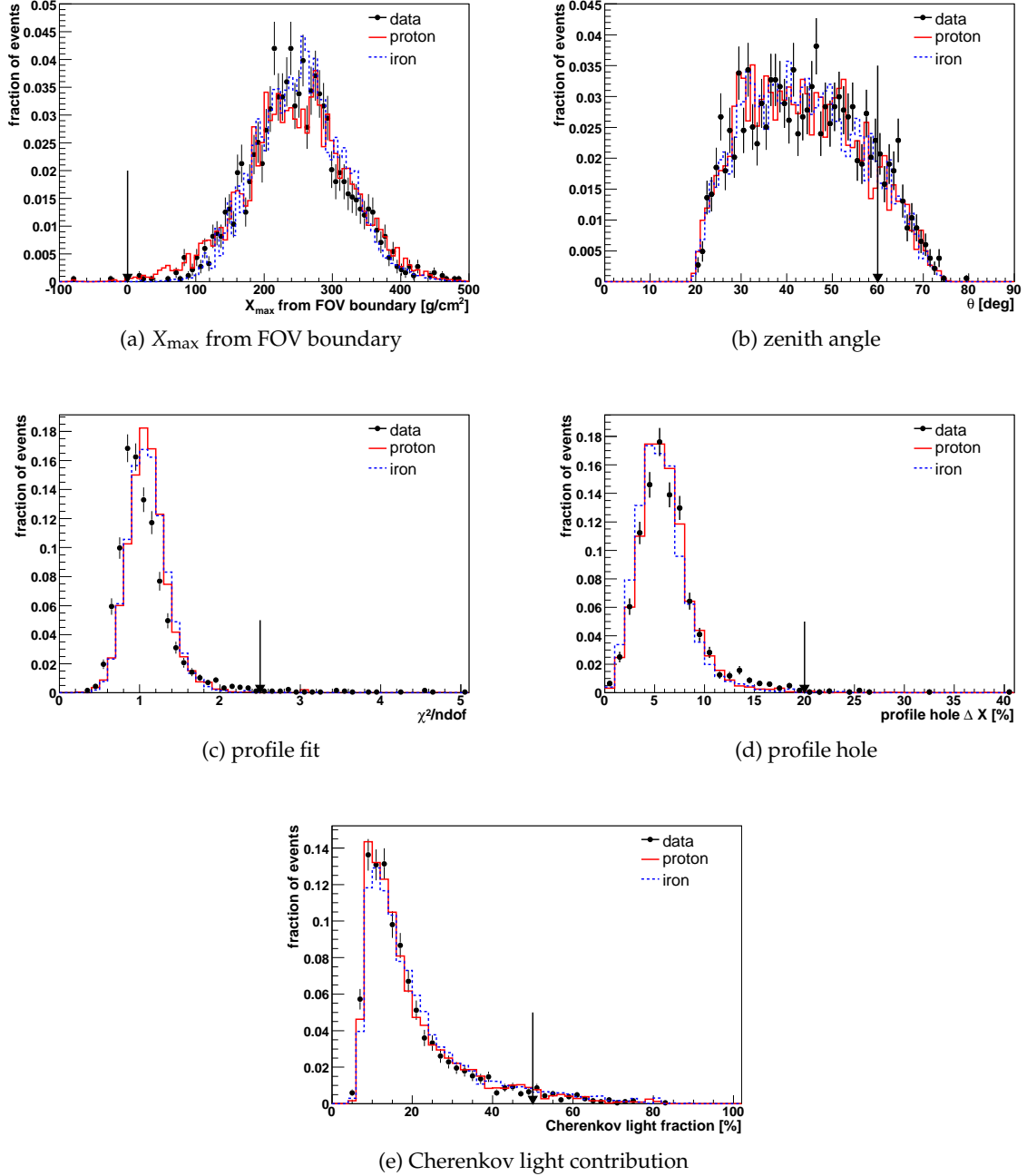
(d) profile hole

(e) Cherenkov light contribution

Figure D.1.1: Comparison between data and MC of the parameters used for the event selection. All event selection criteria, expect the depicted one, are applied and the simulated shower are weighted to following Eq. 6.2.8. The arrow denotes the event selection criteria.

D.2 Energy scale uncertainty

The systematic uncertainty of the overall energy scale of the Pierre Auger Observatory and the unknown mass composition of the primary cosmic rays lead to uncertainties in the determination of the available fiducial volume. Theses uncertainties are removed by restricting the fiducial volume used for the hybrid spectrum determination to the region in which the data and MC distribution agree with each other. As illustrated in Fig. D.2.2, the selection criteria are chosen in a way that no systematic uncertainty is remaining even for extreme assumptions of primary masses and energy shifts.
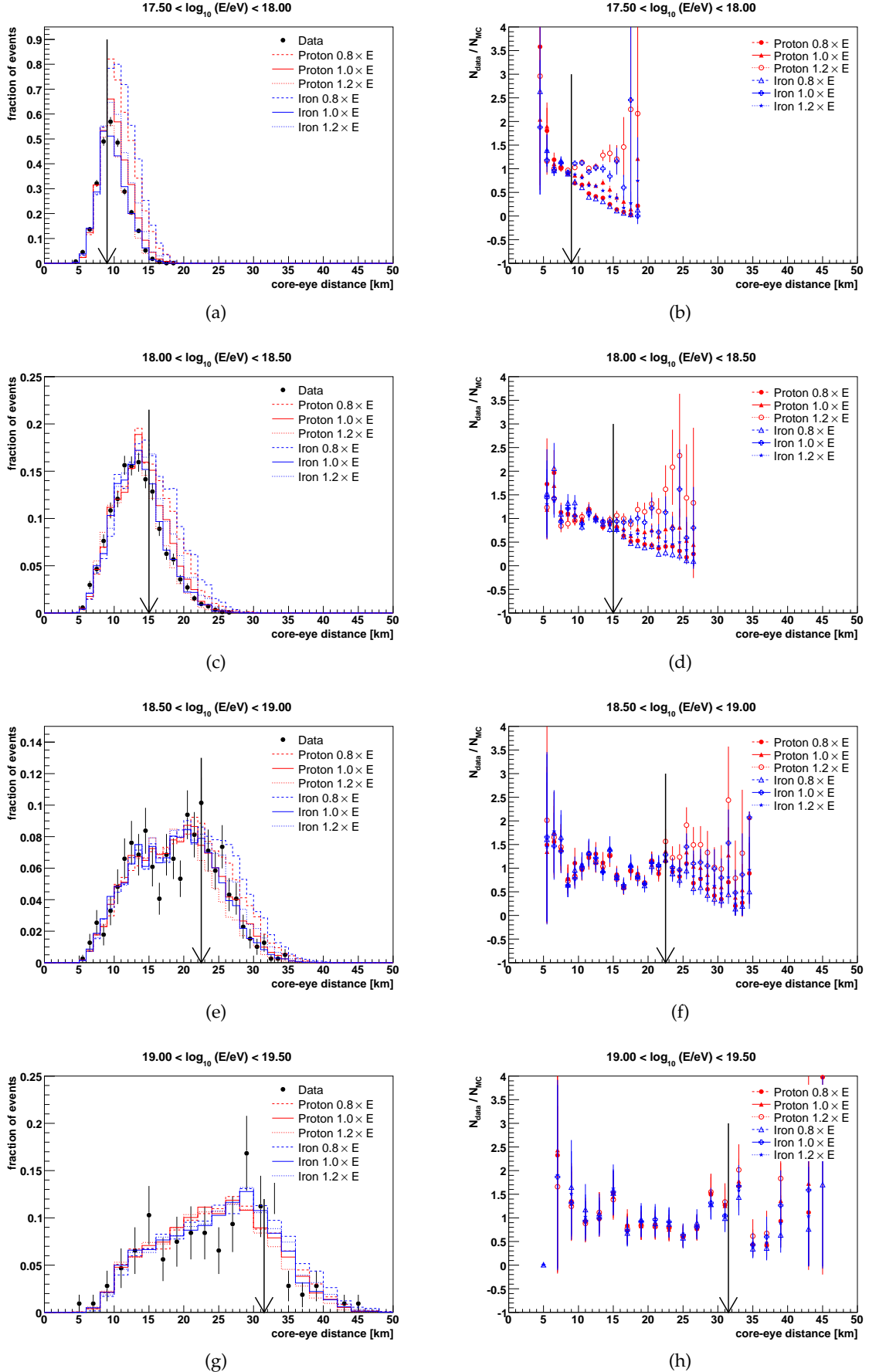
Figure D.2.2: The systematic uncertainty of the energy scale and primary mass composition is not converting into a systematic uncertainty of the hybrid spectrum.
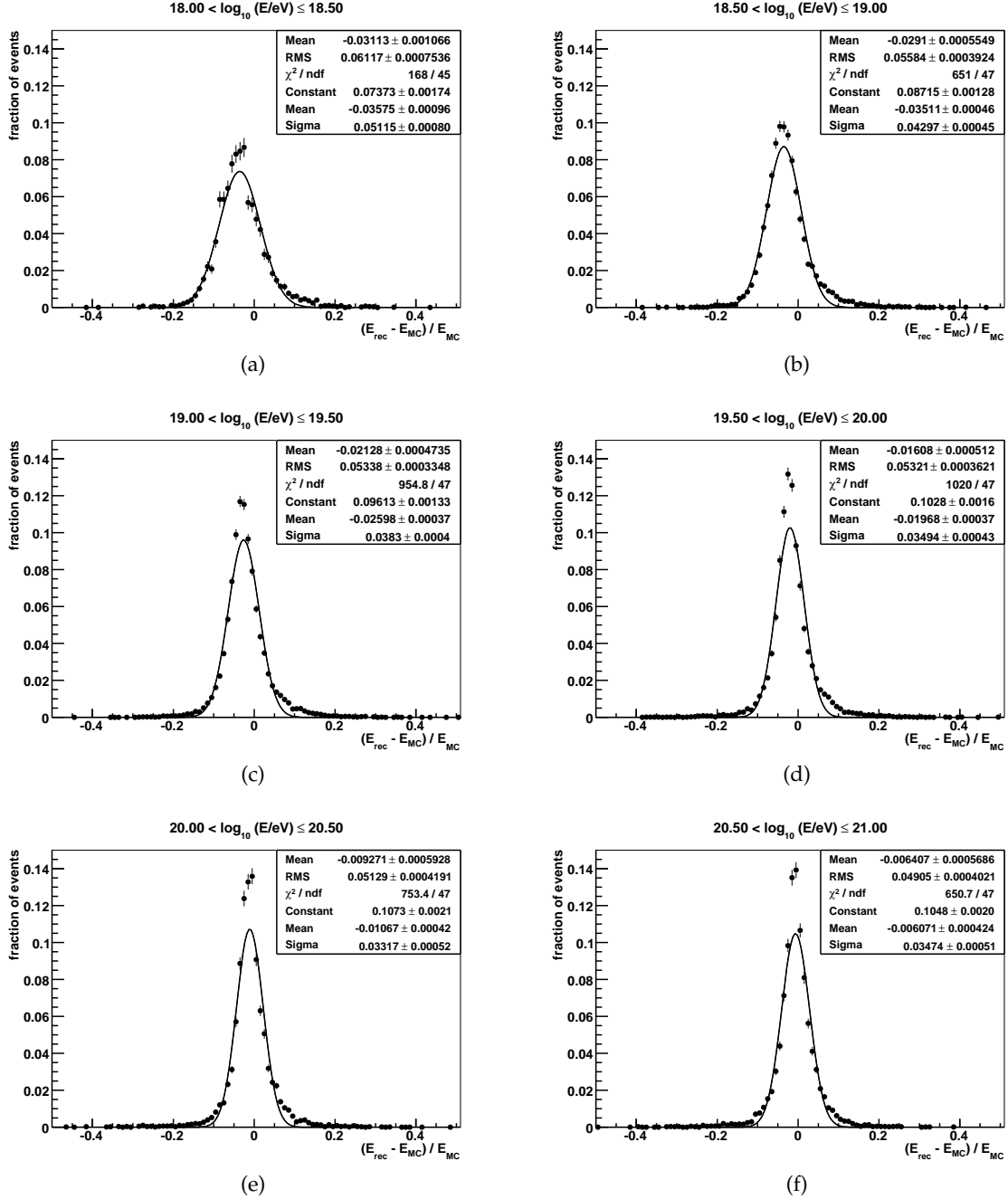
D.3 Energy resolution

Figure D.3.3: The energy resolution of events passing all quality and fiducial volume cuts determined by REALMC simulation.

Appendix E

Comparison with phenomenological models

E.1 Dip model

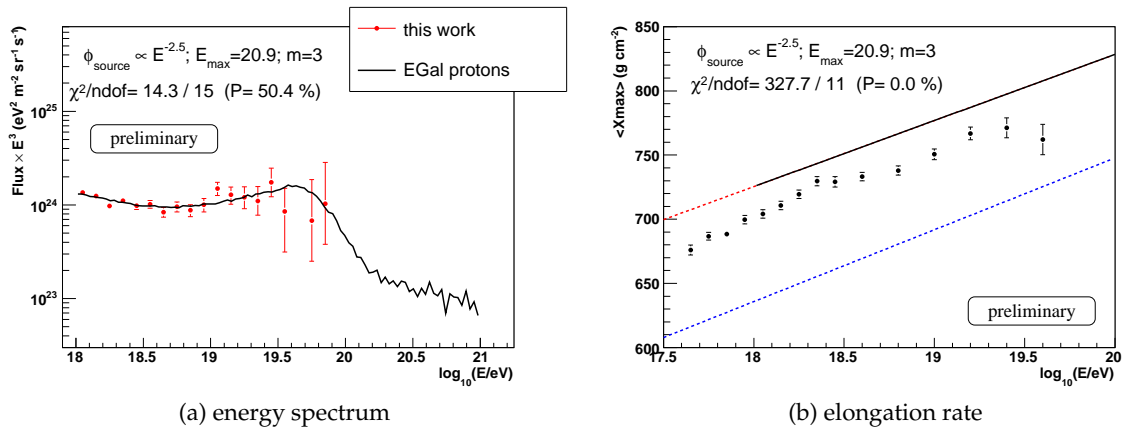(a) energy spectrum

(b) elongation rate

Figure E.1.1: Comparison between the energy spectrum derived in this work and a measurement of the elongation rate [55] with predictions of the 'dip model' [84] (model data from [190]). Although this model is able to describe the spectral shape (left panel), the extra-galactic sources are assumed to accelerate only protons which is not supported by the X_{max} measurements (right panel). The QGSJET01 hadronic interaction model has been used to interpret the X_{max} data.

E.2   Mixed composition model

(a) energy spectrum

(b) elongation rate

(c) energy spectrum

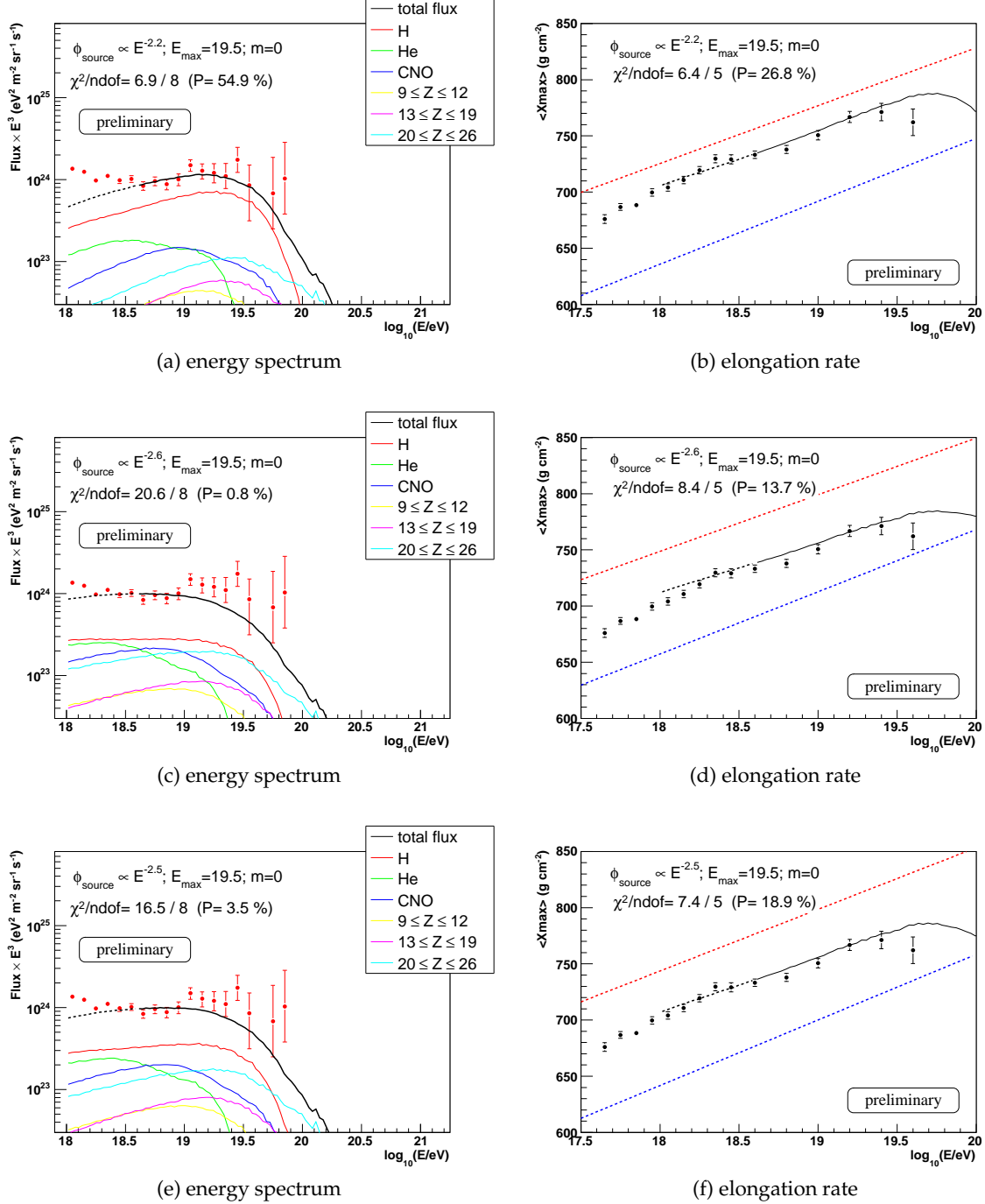(d) elongation rate

(e) energy spectrum

(f) elongation rate

Figure E.2.2: Comparison between the energy spectrum derived in this work and a measurement of the elongation rate [55] with predictions of the 'mixed composition model' [85, 190]. The extragalactic sources are assumed to accelerate nuclei with a mass composition similar to the galactic abundances. The QGSJET01 (upper panel), QGSJETII-03 (middle panel) and SIBYLL (lower panel) hadronic interaction models have been used to interpret the X_{max} data.